TECHNISCHE UNIVERSITÄT MÜNCHEN
Fakultät für Chemie
Bayerisches NMR Zentrum

NMR structural and biochemical studies on the β-barrel membrane proteins OEP21 and hVDAC1

Elisabeth Häusler

Vollständiger Abdruck der von der Fakultät für Chemie der Technischen Universität München zur Erlangung des akademischen Grades eines

Doktors der Naturwissenschaften (Dr. rer. nat)

genehmigten Dissertation

Vorsitzende/-r: Priv.-Doz. Dr. Gerd Gemmecker

Prüfende/-r der Dissertation:

1. Prof. Dr. Franz Hagn
2. Prof. Dr. Michael Sattler

Die Dissertation wurde am 06.07.2020 bei der Technischen Universität München eingereicht und durch die Fakultät für Chemie am 04.08.2020 angenommen.

Table of Content

List of figures

List of tables

Abbreviations

ADAM17	A disintegrin and metalloprotease 17
ADP	Adenosine diphosphate
Amp	Ampicillin
AMP	Adenosine monophosphate
ApoA-I	ApolipoproteinA-I
APS	Ammonium persulfate
ATP	Adenosine triphosphate
BB	Bio-Beads™ SM-2
BME	β-mercaptoethanol
bP	Bacteriorhodopsin
BS^3	Bis[sulfosuccinimidyl]suberate
CD	Circular dichroism
CHAPS	3-[(3-cholamidopropyl)dimethylammonio]-1-propanesulfonate
CHAPSO	3-[(3-cholamidopropyl)-dimethylammonio]-2-hydroxy-1-propanesulfonate
cmc	Critical micelle concentration
CSP	Chemical shift perturbation
DDM	n-dodecyl-β-D-maltopyranoside
DHPC	1,2-dihexanoyl-sn-glycero-3-phosphocholine
DLS	Dynamic light scattering
DM	n-decyl-β-D-maltopyranoside
DMPC	1,2-dimyristoyl-sn-glycero-3-phosphocholine
DPC	Fos-choline-12
16-DSA	16-DOXYL stearic acid
E	Elution
E. coli	Escherichia coli
FID	Free induction decay
FT	Flow through
fwd	Forward
GAP	Glyceraldehyde-3-phosphate
GAPDH	Glyceraldehyde-3-phosphate dehydrogenase
GB1	Immunoglobulin-type B1 domain of protein G
GdmCl	Guanidinium chloride
GpA	Glycophorin A
HEPES	4-(2-hydroxyethyl)-1-piperazineethanesulfonic acid
HMQC	Heteronuclear multiple quantum correlation
HSQC	Heteronuclear single quantum correlation
hVDAC1	Human voltage dependent anion channel 1
IE	Inner envelope
INEPT	Insensitive nuclei enhancement polarization transfer
IPTG	Isopropyl-β-D-1-thiogalactopyranoside
ITC	Isothermal calorimetry
Kan	Kanamycin
K_D	Dissociation constant
LB	Lysogeny broth
LDAO	Lauryldimehylamine-N-Oxide (= n-dodecyl-N,N-dimethylamine-N-oxide)
MD	Molecular dynamic
MP	Membrane protein
MSP	Membrane scaffold protein
MV	Mean value
ND	Nanodisc

NMR	Nuclear magnetic resonance
NOESY	Nuclear Overhauser enhancement spectroscopy
OEP21	Outer envelope protein 21
OE	Outer envelope
OG	n-octyl-β-D-glycopyranoside
OMM	Outer mitochondrial membrane
PCR	Polymerase chain reaction
PDB	Protein data bank
PGK	Phosphoglycerate kinase
PRE	Paramagnetic relaxation enhancement
rev	Reverse
rf	Radiofrequency
rmsd	Root mean square deviation
S75a	Superdex 75 10/300
S75p	Superdex 75 pg
S200a	Superdex 200 10/300
S200p	Superdex 200 pg
SD	Standard deviation
SDS	Sodium dodecyl sulfate
SEC	Size exclusion chromatography
SLS	Static light scattering
SMALP	Styrene-maleic acid polymer
SP FF	SP sepharose fast flow
TCA	Trichloroacetic acid
TEMED	Tetramethylethylenediamine
TIM	Translocase of the inner membrane
T_m	Melting temperature
TM	Transmembrane
TOC	Translocase of the outer membrane
TP	Triosephosphates
Tris	Tris(hydroxymethyl)aminomethane
TROSY	Transverse relaxation-optimized spectroscopy
W	Wash
wt	Wildtype

Abstract

The β-barrel membrane proteins are versatile integral membrane proteins, which occur primarily in the outer membrane of plastids or bacteria and mediate mainly the transport of a large variety of metabolites. Facilitating this transport, they have a pore-like structure of variable size, where additional protein domains are often required to regulate the transport capability. In order to investigate these membrane proteins in a near-native and suitable environment, appropriate membrane mimetics need to be identified.

This thesis focuses on structural and functional analysis of two β-barrel membrane proteins: the outer envelope protein of 21 kDa (OEP21) in chloroplasts and the mitochondrial outer membrane protein human voltage-dependent anion channel (hVDAC1).

Chloroplast are the main producer of phosphorylated carbohydrates, which have to be transported through the double membrane system into the cytosol for an optimal cell function. Channel proteins, such as the chloroplastic outer envelope protein OEP21, facilitate the translocation of these negatively charged solutes and metabolites in an either outward or inward rectifying manner. In this research, the high-resolution structure of OEP21 in LDAO micelles was determined by using NMR spectroscopy, revealing a 12 anti-parallel β-stranded barrel with a large tendency to oligomerize. The monomer itself has a funnel-like shape with mainly positive charges on its inner surface, causing a strong affinity to negatively charged solutes. ATP and glyceraldehyde 3-phosphate (GAP), as main metabolites in chloroplasts, are able to bind and stabilize OEP21, while GAP is transported through the channel and ATP has the ability to block OEP21. The efficiency of this GAP transport is modulated by the ATP to GAP ratio as well as by the positive charges within the pore, revealed by mutagenesis of amino acid involved in the GAP translocation.

The human voltage-dependent anion channel hVDAC1 is an essential key player located in outer membrane of mitochondria. It directs the transport of small hydrophilic molecules and is therefore indispensable for a functioning metabolic cross-talk. With changing its oligomeric state, the β-barrel further functions as gateway for the pro-apoptotic cytochrome c. However, oligomerization of hVDAC1 and the related functional changes is not fully characterized so far. Therefore, hVDAC1 is used as a model system to establish a novel assay for quantifying membrane proteins insertion into phospholipid nanodiscs, based on a cleavable GB1-fusion construct. After the nanodisc assembly and proteolytical cleavage of GB1, the number of inserted membrane proteins can be calculated using the absorption at 280 nm for GB1 and the

nanodiscs. Applying this method, the number of hVDAC1 in MSP1D1 and MSP1D1ΔH5 nanodiscs can be determined at different assembly conditions, revealing mainly monomers with a tendency of cooperative co-assembly.

Structurally and functionally characterization of two β-barrel membrane proteins were performed. Regarding OEP21, a high-resolution structure in LDAO micelles, as well as functional insights of the transport and interaction of GAP and ATP could be obtained using NMR spectroscopy, biochemical assays and MD simulations. Additionally, a novel method was established for quantifying the oligomeric state of a membrane protein in phospholipid nanodisc using a GB1-fusion construct. Applying this approach, the quantity of hVDAC1 in MSP nanodiscs could be determined and manipulated by changes in assembly conditions.

Zusammenfassung

Die β-Fass (engl. *β-barrel*) Membranproteine sind vielseitige integrale Membranproteine, welche vorwiegend in der äußeren Membran von Plastiden und Bakterien lokalisiert sind. Sie fungieren dabei meist als Transportproteine für eine große Anzahl verschiedener Metabolite und weisen eine porenähnliche Struktur unterschiedlicher Größe auf. Zusätzliche Proteindomänen können dabei deren Transporteigenschaften regulieren. Um solche Membranproteine zu charakterisieren, sind geeignete Membranmimetika nötig, welche die Proteine solubilisieren und dabei ein natives Umfeld imitieren.

Diese Arbeit basiert auf zwei dieser β-Fass Membranproteine und deren strukturelle und funktionale Analyse: das jeweils in der äußeren Membran lokalisierte Chloroplasten-Protein OEP21 (*outer envelope protein of 21 kDa*) und das mitochondriale Proteine hVDAC1 (*human voltage-dependent anion channel 1*).

Chloroplasten sind die Hauptlieferanten von phosphorylierten Kohlenhydraten, welche durch die Doppelmembran in das Cytosol transportiert werden müssen, um für eine optimale Zellfunktion zu sorgen. Bestimmte β-Fass Membranproteine, wie das *outer envelope protein* OEP21, ermöglichen den Transport dieser negativ geladenen Metabolite und fungieren dabei als Anionen-selektiver Kanal mit nach innen oder nach außen gerichteten Transport. In dieser Arbeit wurde die hochauflösende Struktur von OEP21 in LDAO Mizellen mittels NMR-Spektroskopie bestimmt. Diese besteht aus 12 antiparallel verlaufende β-Faltblättern und besitzt eine hohe Tendenz zur Oligomerisierung. Das Monomer selbst besitzt eine trichterartige Form mit einer hohen positiven Ladungsdichte im Inneren der Pore, welche eine hohe Affinität zu negativ geladenen Metabolite begünstigt. ATP und Glycerinaldehyd 3-phosphate (GAP), die primären Metabolite in Chloroplasten, weisen einen stabilisierenden Effekt auf OEP21 auf, wobei GAP durch die Pore transportiert wird und ATP dagegen den Kanal blockiert. Die Effizienz des GAP Transports ist dabei abhängig vom Verhältnis GAP zu ATP, sowie der positiven Ladungsdichte im Inneren der Pore, welche mit Hilfe von Mutagenese der im GAP Transport involvierten Aminosäuren, gezeigt wurde.

Das hVDAC1 (*human voltage-dependent anion channel 1*) ist ein relevantes Membranprotein in der menschlichen Zellen. Es steuert den Transport kleiner hydrophiler Moleküle und ist unverzichtbar in einer funktionierenden Metabolit-basierten inter- und intrazellulären Kommunikation. Mit Änderung seines Oligomerisierungsgrades erlangt hVDAC1 unter anderem die Fähigkeit pro-apoptotisches Cytochrom c zu transportieren.

Jedoch sind bisher sowohl die Oligomerisierung als auch die damit verbundenen Änderungen in dessen Funktion noch nicht vollständig begründet. Daher dient hVDAC1 als Modelsystem für die Etablierung eines Assays zur Quantifizierung von Membranproteinen in MSP Nanodiscs. Diese Methode basiert auf dem Fusionskonstrukt von GB1 mit entweder hVDAC1 oder MSP. Nach Insertion des Membranproteins in Phospholipid-Nanodiscs und proteolytischer Spaltung von GB1, kann mit Hilfe von UV-Absorption die Konzentration von GB1 und den Nanodiscs bestimmt werden. Auf Basis dessen, lässt sich anschließend das Verhältnis von Membranprotein zu MSP berechnen. Unter Verwendung dieser Methode konnte die Anzahl von hVDAC1 in MSP1D1- und MSP1D1ΔH5-Nanodiscs mit verschiedenen Assemblierungsbedingungen bestimmt werden, wobei sich hVDAC1 vorwiegend als Monomer in den zwei Nanodisc Varianten insertieren lässt. Durch Anpassung der Assemblierungsbedingungen kann jedoch eine Tendenz der kooperativen Co-Assemblierung von hVDAC1 in MSP1D1 Nanodiscs gezeigt werden.

Hier wurden zwei β-Fass Membranproteine strukturell und funktionell charakterisiert. Für OEP21 konnte nicht nur eine hochauflösende NMR Struktur in LDAO Mizellen bestimmt werden, sondern auch funktionelle Erkenntnisse hinsichtlich des Transports und der Interaktion von GAP und ATP gewonnen werden. Zudem wurde eine verlässliche Methode entwickelt, welche die Quantität von Membranproteinen in Phospholipid-Nanodiscs bestimmen kann. Unter Anwendung dieser Methode, konnte gezeigt werden, dass die Anzahl der insertierten Membranproteine mit Hilfe verschiedener Assemblierungsbedingungen manipuliert werden kann.

1. Introduction

1.1. Functional relevance of membrane proteins

Membrane proteins are crucial key players in diverse cell functions, such as cell signaling, regulation of apoptosis and cell survival or transport of metabolites, proteins and small molecules. Despite this essential role of membrane proteins, a lack of information about their structure, function and interaction with other proteins and substances exists. This is traced back to the challenging expression, purification and refolding into their native state, due to the hydrophobic environment they are located in. But in the past few years membrane proteins became extensively studied as more and more various membrane mimicking systems have been established. This increasing interest in membrane proteins is also reflected in the increase of structures reported. But compared to the overall number of protein structures, which are known and published so far, membrane proteins count only 0.6 % (**Figure 1**). Therefore, structural and functional elucidation of this group of protein increases in the field of protein characterization.

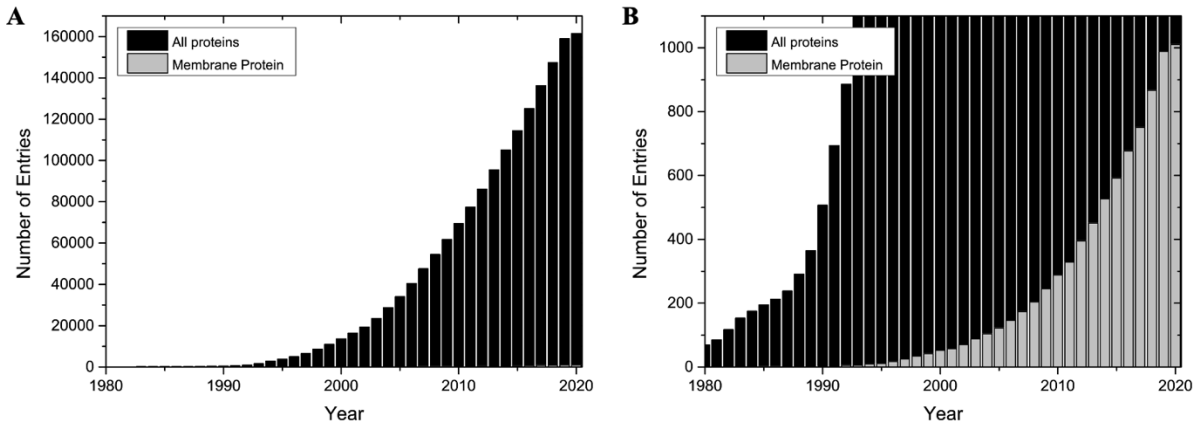

Figure 1: Illustration of the number of protein structures published accumulated per year. *Black is representing the number of all proteins, grey represents the number of solved structures for membrane proteins. Figure **A** shows the whole bar diagram. Figure **B** displays a detail of A with a closer look on the increase of the number of solved membrane protein structures until March 2020 [1, 2].*

Depending on their location, membrane proteins can be classified in two groups: integral and peripheral membrane proteins. Integral membrane proteins are mainly or fully located in in the membrane lipid bilayer, whereas peripheral membrane proteins are located at the membrane surface, with an attached lipid anchor or transmembrane helix, or specific lipid-binding surface properties. [3-6] **Figure 2** depicts the class of membrane proteins illustrated

with different examples. Focusing on the integral membrane protein, the location affects the composition of the amino acids located in the hydrophobic environment, since hydrophobic amino acids stabilize these protein structure. Integral membrane proteins show also a broad range of secondary structure. They can occur as a single transmembrane helix (e. g. Bcl-xL, ADAM17) [7, 8], as multiple helices (e. g. bR, NTS1, iRhom2) [8-10] or even as a β-barrel pore formed by β-strands through the lipid bilayer (e. g. hVDAC1, OmpX, OEP21) [11-13]. The structure gives information about the relative function of these proteins. Single helices are often anchoring the protein to the membrane, while the soluble part bears the reactive center (e. g. Bcl-xL, TNFα, ADAM17) [7, 8, 14, 15]. Multiple helices can interact with other integral membrane proteins and are responsible for signal transmission, whereas the function of β-barrel porins are mainly for shuttling metabolites. But not only the secondary and resulting tertiary structure are determining the function of the integral membrane proteins but also the oligomerization of those. Few are known for forming dimers or higher oligomers and by that changing its function.

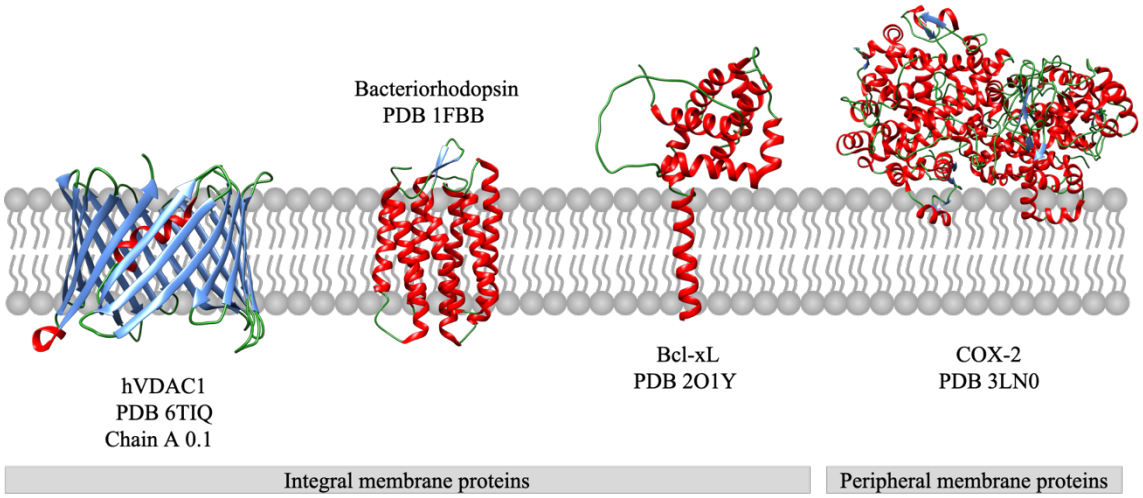

Figure 2: Different membrane protein classes represented by selected membrane proteins. *Integral membrane proteins represented by hVDAC1 (PDB 6TIQ)[16] as β-barrel membrane protein, Bacteriorhodospin (PDB 1FBB)[17] as seven transmembrane spanning α-helical protein and Bcl-cL (PDB 2O1Y)[18] as membrane anchored α-helical transmembrane protein. Peripheral membrane proteins represented by Cyclooxygenase 2 (COX-2, PDB 3LN0) [19].*

1.1.1. α-helical membrane proteins

α-helical proteins or parts of a protein have to comprise a hydrophobic surface pointing towards the lipidic interior of the membrane. A single helix consists of about 20 to 30 amino acids, mainly with aliphatic residues and phenylalanine. [20] The structure of many α-helical

membrane proteins have been solved. For example, the single transmembrane helix of glycophorin A (GpA) forms a stable homodimer [21], whereas the integral membrane protein bacteriorhodopsin (bR) has seven helixes [9]. In contrast, Bcl-xL consists of a α-helical transmembrane anchor and a catalytical active soluble part. [7, 22]. In general, the structural characteristics can be informative to some extent. Single transmembrane helices functions as anchor to the membrane (Bcl-xL), they can constitute the dimerization site (GpA) [23] or facilitates signal transduction like the proton pump bR [9]. These structures and functions are exemplary for the versatility in function of α-helical membrane proteins.

1.1.2. β-barrel membrane proteins

β-barrel membrane proteins have been detected especially in the outer membrane of bacteria, chloroplasts and mitochondria and show a variety of function, such as non-specific porins, energy-dependent transporter influx and efflux, protein secretion pore etc. [24]. Up to now, 1010 3D-structures of membrane proteins have been solved [1] while thousands more are identified but still not functionally and/or structurally characterized. Membrane proteins featuring β-strands show the following common characteristics. The β-strands are directed in an antiparallel manner and are connected via hydrogen bonds, which form a circular pattern and result therefore in its β-barrel shape. These hydrogen bonds are essential for the stability of the barrel itself and also its stability within the hydrophobic lipid interface. Nevertheless, the β-barrel membrane proteins show also significant sequence in its amino acid composition. To that fact, amino acids located and directed towards the lipid bilayer of the membrane have to be non-polar and uncharged. [24, 25] The β-hairpins are linked via short turns of long loops directed to the periplasmic side, to the cytosol or to the intermembrane space of mitochondria or chloroplasts. β-barrel membrane proteins consist at least of eight β-strands and almost always of an even number of β-strands. An exception is the human voltage-dependent anion channel 1 (hVDAC1), which consists of 19 β-strands. [11]

β-barrel membrane proteins can not only be present as monomer (e.g. OmpA, OmpX), but also form dimers (OmpLA), trimers (LamB) and even higher oligomers. They can be divided in various functional categories, such as nonspecific porin (OmpF, OmpG, PhoE), specific porins (LamB, ScrY, Tsx), protease (OmpT), lipase (OmpLA), protein pore-forming toxin (α-Hemolysin) or export channels (TolC) etc. [24, 25]

In this work, two β-barrel membrane proteins are studied: OEP21 (outer envelope protein of 21 kDa) and hVDAC1 (human voltage-dependent anion channel 1), which are located in the outer envelope of chloroplasts or the mitochondrial outer membrane, respectively.

1.2. The β-barrel membrane proteins OEP21 and hVDAC1

OEP21 is a chloroplastic outer envelope protein, that facilitates the translocation of negatively charged metabolites such as ATP, GAP and other triosephosphates. VDAC1 is a voltage dependent ADP/ATP transporter in the outer mitochondrial membrane, that is relevant for the regulation of apoptosis and is supposed to interact with a large variety of partner proteins.

1.2.1. The chloroplast β-barrel membrane protein OEP21

OEP21 was first described in 1999 by Bölter *et al.* as a 21 kDa β-barrel membrane protein located in the outer membrane of chloroplasts, facilitating the translocation of negatively charged solutes and metabolites, such as 3-phosphoglycerate, triosephosphates and phosphates. But until now OEP21 was not structurally characterized and therefore the insight of the transport on a molecular basis could be studied.

Chloroplasts are the central location of the photosynthesis which in combination with the dark reaction (Calvin cycle) provide oxygen, sugar and other vital metabolites, such as triosephosphates (TPs), 3-phosphoglycerate, amino acids and amines. To some extend these products have to be transported through the double membrane system (inner and outer envelope) of the chloroplasts to the cytosol, where further metabolism is taking place [26, 27]. Permeability through the inner envelope (IE) of the chloroplast is directed by a large variety of proteins (*i. a.* TIC, TGD-1, PPT, NNT) [28-31]. In contrast, the outer membrane (OE) of the chloroplast was firstly thought to act as a permeable sieve to small molecules by forming pores. [32] Recently, a variety of proteins were detected in the outer membrane of chloroplasts, which are involved in several processes, such as transport, lipid metabolism and proteolysis and redox defense [33]. Two main classes of proteins in the outer envelope are known so far, the Toc (translocase of the outer chloroplastic membrane) and OEP (outer envelope protein). The Toc proteins are interacting with the Tic (translocase of the inner chloroplastic membrane) proteins to facilitate the translocation of proteins and precursor proteins [29]. In contrast, the OEPs serve as transporters for diverse small metabolites, as listed above. For example, TPs, ATP, P_i, dicarboxylic acid as well as positively and negatively charged amino acids are translocated

through the outer envelope protein of 24 kDa (OEP24), a cation selective channel. It has been shown, that OEP24 can functionally replace the ADP/ATP selective channel voltage-dependent anion channel (VDAC) in mitochondria. In contrast OEP16 excludes the transport of TPs and uncharged sugars, but facilitates the translocation of amino acids and amines. [34]

Another protein of the OEP family is OEP21 (outer envelope protein of 21 kDa), which forms a rectifying channel in the outer membrane of chloroplasts for the translocation of negatively charged solutes. This channel is assumed to consist out of eight transmembrane β-strands and forms a pore by two monomeric units, with a diameter of around 1 nm at the so-called restriction zone and 2.4 nm at the wider vestibule. In the restriction zone a binding site for ATP and other negatively charged solutes is located, whereas at the vestibule the ATP binding motif FX_4K is placed. The channel properties are regulated by binding of ATP and are also directed by the ratio of ATP to TPs in a competitive manner. This ratio is responsible for the direction of the rectifying channel. A high ATP:TP/P_i ratio results in an inward-rectifying channel, whereas a low ratio leads to an outward-rectifying OEP21 channel (depicted in **Figure 3 A**). [13, 35, 36] The ratio of ATP and TPs is conducted by the ongoing prominent reaction. This means in high photosynthetic activity, the chloroplast produces high amount of ATP leading to the inward rectification, while under dark conditions the ratio reverses and the outwards rectification is pronounced. In each case the transport of triosephosphates is predominant, but translocation of ATP is not excluded completely, since the size of ATP indicates that it passes in a tight manner. [13, 35, 36].

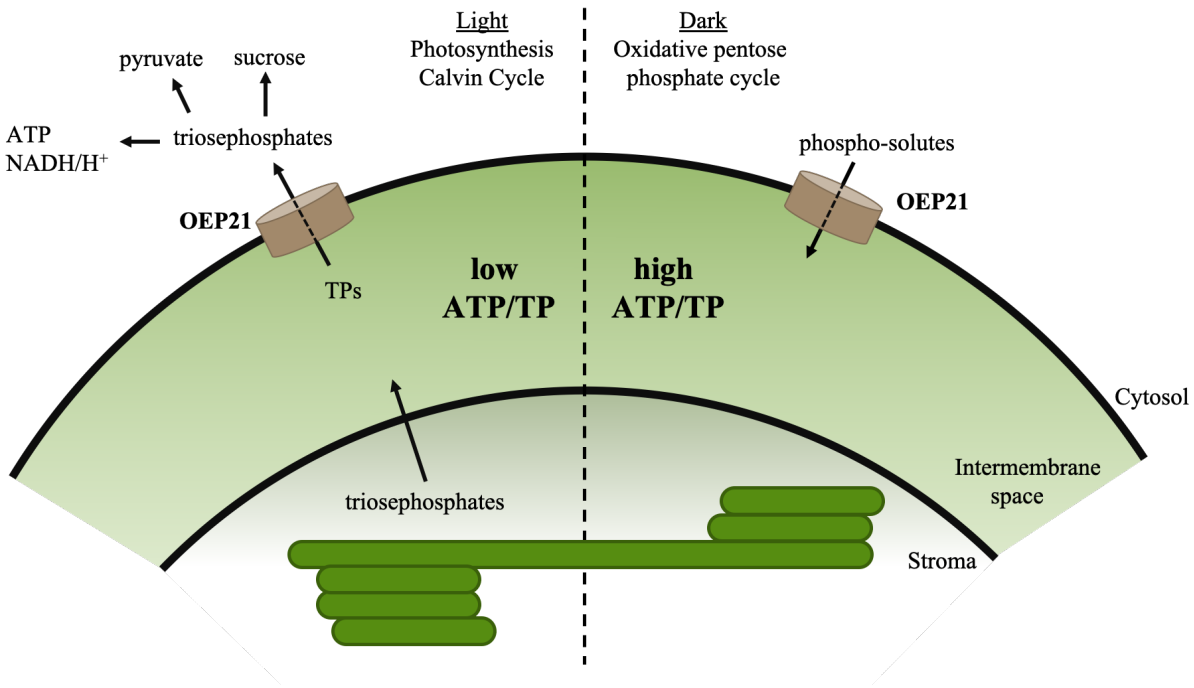

Figure 3: Schematic description of the transport of ATP and TPs from chloroplasts to cytosol. *At light, low ATP to TP ratio results in an outward rectifying OEP21 channel, whereas at dark, a high ATP to TP ratio leads to an inward rectifying OEP21 channel. [36]*

1.2.2. The mitochondrial β-barrel membrane protein hVDAC1

The human voltage dependent anion channel 1 (hVDAC1) is one of the most studied membrane proteins in the outer membrane of mitochondria [37-41], but still the detailed understanding of its mechanism remains unclear.

Mitochondria are a crucial plastid in all eukaryotic cells and similar to chloroplast. They are also enveloped by a two-membrane system, the inner mitochondrial membrane and the outer mitochondrial membrane and possess its own mitochondrial DNA (mtDNA). In mitochondria essential mechanisms and reactions of cell survival and death are taking place, amongst others the citric acid cycle and releasing of the resulting metabolites to the cytosol, oxidative phosphorylation, storage of Ca^{2+} ions and programmed cell death by releasing cytochrome c [42-44]. To preserve the communication of the mitochondria and the remaining cells, the transport of vital metabolites has been allocated through the double membrane. This task is handled by membrane proteins located in both, the inner and the outer mitochondrial membrane. For example, protein translocation is conducted by a complex of the translocase in the inner membrane and the translocase in the outer membrane, the so-called TIM/TOM-complex [45, 46]. In the inner membrane also the hole machinery for the mitochondrial respiratory chain is incorporated, which includes complex I–V (NADH dehydrogenase, cytochrome c reductase, succinate dehydrogenase, cytochrome c oxidase and ATP synthase)

[45]. In addition to the translocation of proteins the transport of metabolites and small solutes has to be ensured through the membranes. In case of the outer mitochondrial membrane (OMM), these solutes pass through the so-called porins. The main porin in the OMM is the voltage dependent anion channel (VDAC), which exists in three or more isoforms [47]. As mentioned earlier the human voltage dependent anion channel 1 (hVDAC1) is the most studied representative of the all known isoforms, while structural prediction of VDAC1, VDAC2 and VDAC3 suggest a high similarity in their secondary structure [47]. hVDAC1 consists of 19 amphipathic β-strands, connected via short turns and longer loops directed either to the cytosol or to the intermembrane space of the mitochondria. The N-terminus forms an α-helix located in the center of the pore (**Figure 4***)*. The characterization of the N-terminal helix is quite controversial, since already the location and the associated function of this segment has been highly discussed. [40, 48-50]

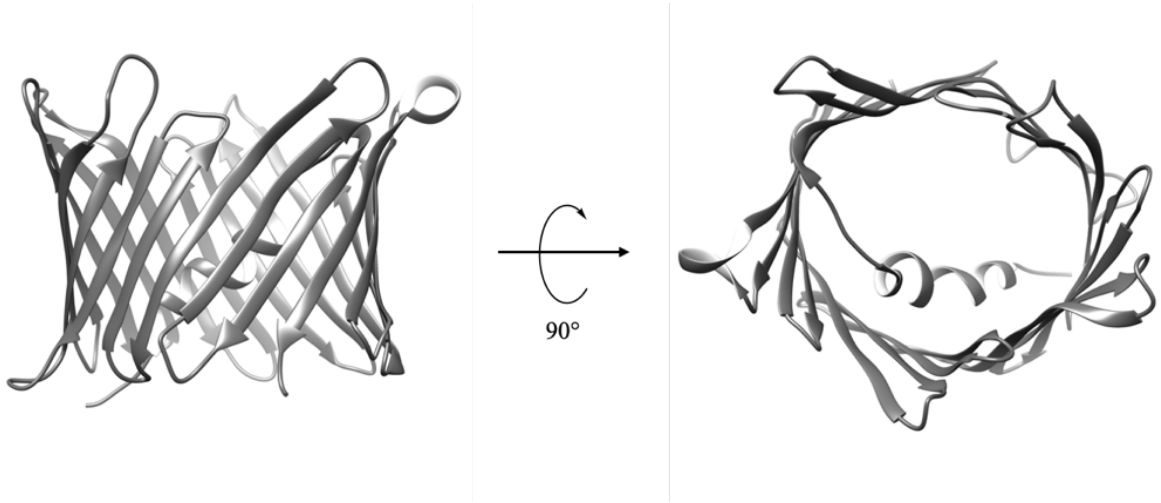

Figure 4: Structure of the voltage-dependent anion channel hVDAC1. *(PDB 6TIQ, Chain A 0.1). Side view of the barrel (left), top view of the barrel revealing the α-helix in the inner part. (right) [51]*

Nevertheless, early studies found out that hVDAC1 shuttles metabolites, such as ATP and glutamate and small cations and anions, predominantly Ca^{2+} ions by containing two binding sites for calcium [37]. Additionally, the interaction to a large number of proteins, which are located in the mitochondrial membrane or are associated with the mitochondria is focused in the research on hVDAC1. It is already known that hVDAC1 forms complexes with a large number of proteins (e.g. hexokinase, cytochrome c, MAP2) and therefore regulates and is involved in a series of functionalities in cell survival and death, such as metabolism, signal transduction, apoptosis and antioxidation [37, 52]. One prominent interaction, which is already intensively studied and still is in focus, is the interaction of Bcl-xL, a protein of the Bcl2 family,

with hVDAC1 (**Figure 5**) and its contribution to apoptosis. [53-58] This interaction occurs at the OMM between the N-terminal α-helix of hVDAC1 and the soluble part of Bcl-xL, promotes therefore the dimeric structure of hVDAC1 and releases cytochrome c from mitochondria, which results in apoptosis [52, 54].

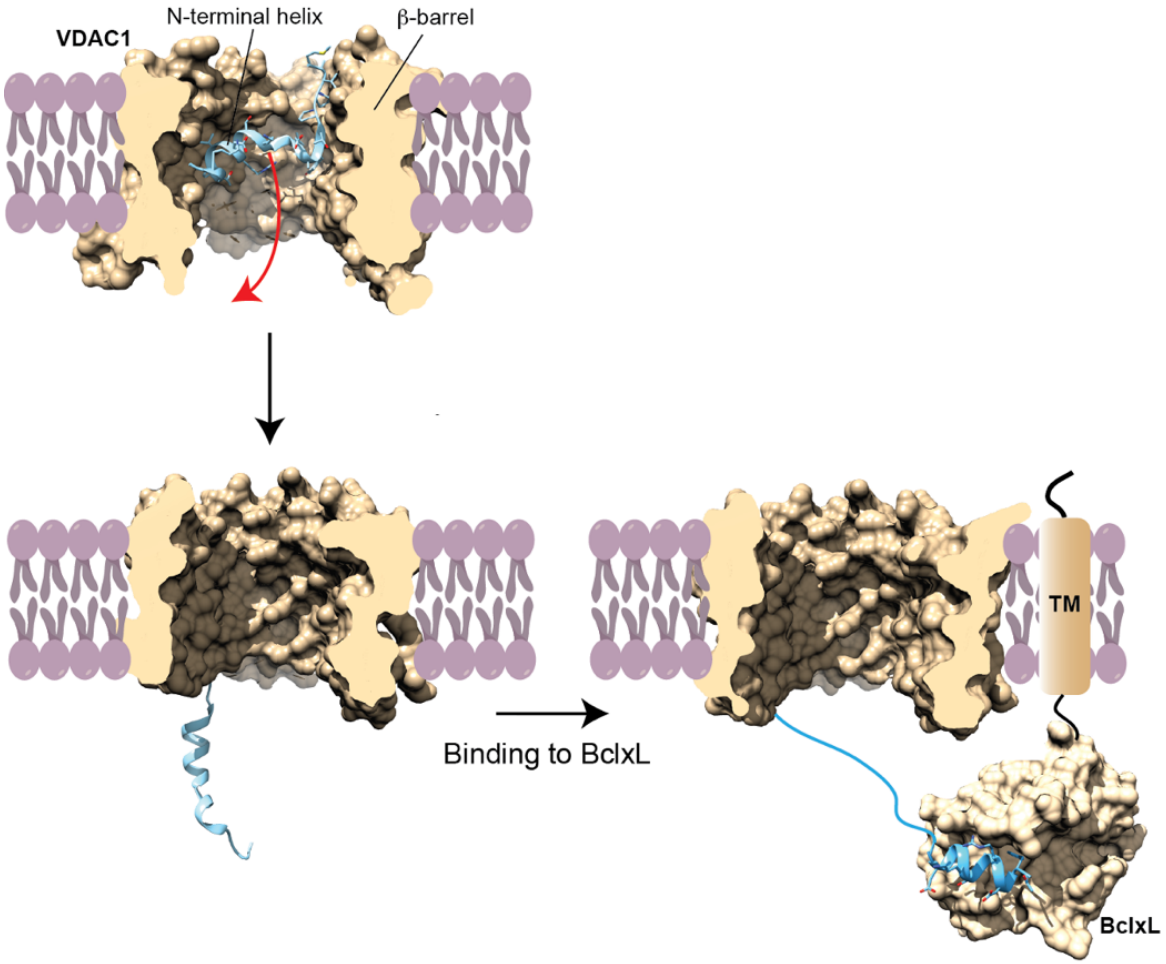

Figure 5: Suggested interaction of hVDAC1 with Bcl-xL. *Translocation of the α-helix from the inside of the β-barrel for interaction with the BH3-binding site of the soluble part of Bcl-xL.*

hVDAC1 has been reported to be involved in many biological processes. However, despite many studies on its structure, function and physical interactions, the overall function, and in particular the role of its oligomeric state in the cell as well as its complexes with partner proteins still needs to be characterized.

1.3. Membrane mimetics

The purification and especially the solubilization of membrane or membrane anchored proteins are challenging, but a necessity to study their structure, functionality and interaction. As described in chapter 1.1 a main feature of membrane proteins are their hydrophobic parts located fully or partially in the membrane. Due to this hydrophobicity, membrane proteins are not soluble in aqueous solutions and therefore an adequate environment is needed. This mimetic has to copy the characteristics of native membranes and has to be soluble in aqueous solutions.

Nowadays a variety of methods are known and applied to mimic biological membranes and in the past years selected systems resemble more and more the native environment of membrane proteins. Beginning with micelles and amphipols, the best choice for native like environments is using lipids to form bilayers. These bilayers can be produced as liposomes or can be stabilized by auxiliary proteins or polymers, such as styrene-maleic acid polymers (SMALP), peptides or membrane scaffold proteins (MSP). An overview of possibilities to mimic the hydrophobic environment with an increasing native character, is given in **Figure 6**.

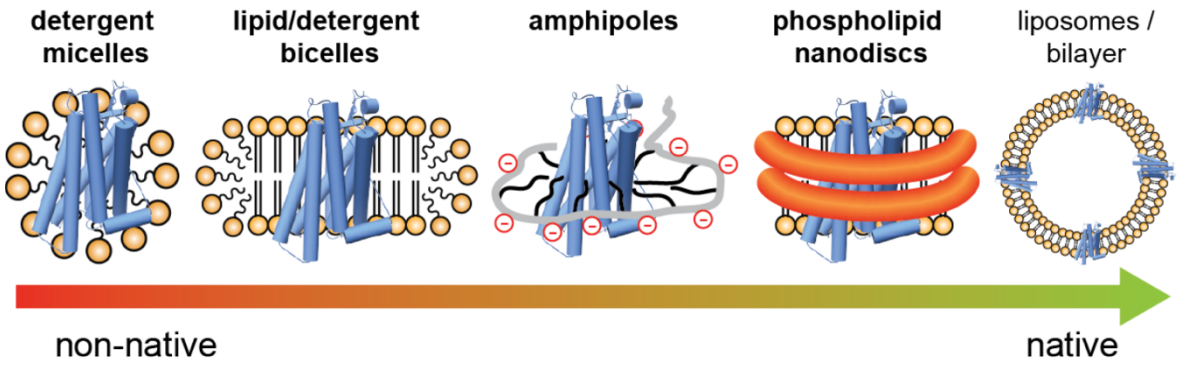

Figure 6: Overview of membrane mimetic systems. *Systems are sorted by their native-like environment, with detergent micelles as non-native and liposomes as native membrane mimetic system. Picture used with permission from Klöpfer & Hagn. [59]*

In the following three subsections, membrane mimetics are outlined in more detail.

1.3.1. Detergent micelles

Detergent micelles are one of the most used membrane mimetics to refold or extract membrane proteins and conduct structural and functional analyses.

First of all, it is necessary to have a closer look on the detergent properties. For studies on membrane protein, the detergent has to be above its critical micelle concentration (cmc), which is dependent of the used detergent and its amphipathic properties. Otherwise the

formation of a micelle would not occur. If the detergent concentration is above the cmc, single molecules bind to each other and form the globular shaped micelle with a hydrophobic core and a hydrophilic surface, which results in its solubility in aqueous solutions. [60, 61]

Detergents can be classified in two categories, ionic and non-ionic detergent, depicting their denaturing feature on proteins. [62] The non-ionic detergents DM, DDM and OG pertained to the class of mild detergents, while DPC, LDAO and SDS are representatives for harsh detergent. DM and DDM are often used to extract proteins from the membrane, such as G-protein coupled receptors (GPCRs) or other helical proteins. Both form large micelles with a size of about 70 kDa. The zwitterionic detergents LDAO and DPC are solubilizing β-barrel membrane proteins or α-helical transmembrane proteins, respectively. Due to their small micelle sizes of roughly 20 kDa these detergents are preferable used to study membrane proteins via NMR spectroscopy. However, NMR studies reveal an impact of detergents on protein folding, interaction and dynamics resulting in reduced dynamics and lower stability [61, 63, 64]. Consequently, the investigation of membrane proteins in other membrane mimetics, such as bicelles, liposome and lipid nanodiscs are attractive to overcome the problems of micellar systems. Nevertheless, due to the proven refolding capacity, the diversity in their features, micelle size and its simple usage, detergent micelles are still applied to determine structural and functional behavior of membrane proteins.

1.3.2. Bicelles as membrane mimetics

In contrast to micelles, bicelles are formed by a mixture of long-chain lipids and short-chain lipids or detergents. The overall structure of every bicelle is the same, the long-chain lipids form a bilayer and surrounding the membrane protein of interest. The short chain lipids or detergents form the stabilizing rim. Various long-chain lipids can be used adjusted to the certain membrane, whereas for detergents or short-chain lipids, CHAPS, CHAPSO and DHPC are often used to form the rim around the bilayer. [59, 65-67] An advantage of this system, beside the diversity of lipids, is the variability of the bicelle size, starting at around 40 kDa and which can be regulated via the ratio of long-chain lipids to detergent q. [59, 61]

In general, bicelles are good alternatives to micelles, since they represent an more native environment, are still easy to prepare and their size can be adapted. Nevertheless they also contain detergents, which still might lead to membrane protein denaturation or destabilization [59].

1.3.3. Lipid-protein nanodiscs using MSP

The membrane scaffold protein (MSP) derives from the apolipoproteinA-I (ApoA-I), which surrounds lipid bilayers, forms thereby soluble particles and is variable in size [12, 59, 68]. Nanodiscs composed of lipids and membrane scaffold proteins (MSP) have some advantages compared to other methods, to stabilize membrane proteins. First, versatile lipids and lipid extracts can be used during the assembly of nanodiscs e.g. *E.coli* lipid extracts. Meaning the lipid environment can be easily adjusted to the native lipid character of the natural origin of the protein. Second, compared to micelles or liposomes, the stability of nanodiscs is increased, since a compact binding around the lipids is present and MSP by itself is highly stable (Tm ~95 °C), resulting in a longer life time of the protein. Another benefit in structural studies is the homogeneity of MSP nanodiscs compared to e. g. micelles and the accessibility of different nanodisc sizes eligible for different membrane protein sizes. [69-71] This variability is achieved by using different truncated versions of MSP (**Figure 7 b, c**). The nanodisc size is selected according to the membrane protein and the applied method. A prominent example is the determination of the OmpX structure, using MSP1D1ΔH5 nanodiscs. This smaller MSP discs are highly applicable for NMR structure determination since NMR spectroscopy requires small and homogenic particles. [12, 59, 69]

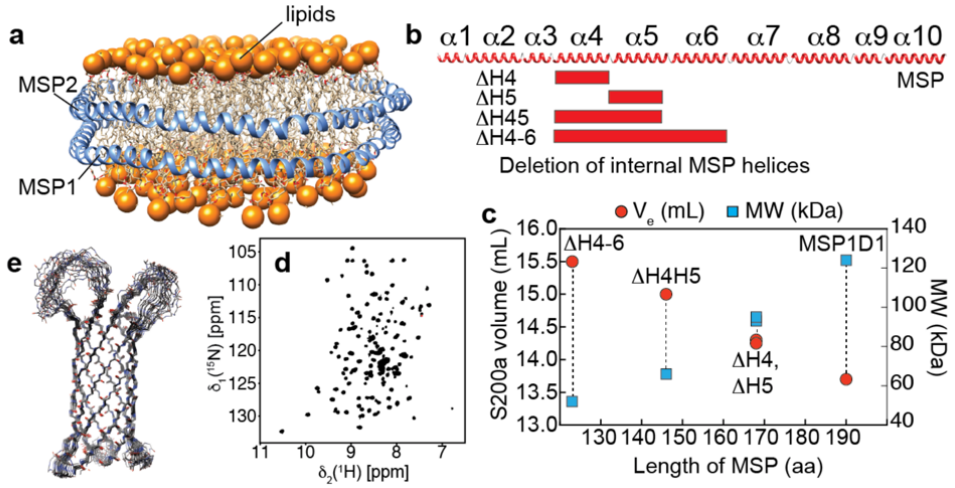

Figure 7: Phospholipid nanodiscs and its application in structural studies. ***a*** *Representation of a MSP nanodiscs composed of a lipid bilayer surrounded by two copies of MSP molecule.* ***b*** *MSP variants, where the truncated regions are highlighted in red.* ***c*** *Relation of SEC elution volume, the molecular weight and the length of the MSP construct.* ***d*** *2D-[^{1}H,^{15}N]-TROSY spectrum of OmpX in MSP1D1ΔH5 nanodiscs.* ***e*** *Solution structure of OmpX in MSP1D1ΔH5 nanodisc determined by NMR spectroscopy. Picture used with permission of Klöpfer & Hagn. [59]*

2. Objectives

The overall objectives of this research, are the structural and functional studies of membrane proteins using NMR spectroscopy and biochemical assays, as well as to further develop the nanodisc technology using MSP. Here, the focus lies on two β-barrel membrane proteins: the chloroplastic membrane protein OEP21 and the mitochondrial membrane protein hVDAC1.

The chloroplastic outer envelope protein OEP21

The first project deals with the chloroplastic outer envelope protein OEP21, which is an important key player in the transport of negatively charged metabolites and solutes, such as triosephosphates, phosphates and ATP. Until now, OEP21 has been only functionally characterized, but a high-resolution structure was not identified yet.

Therefore, the first objective was to structurally characterize the chloroplastic outer envelope protein OEP21 by using NMR spectroscopy, since previous attempts, trying to crystallize the membrane protein, were not successful. Additionally, the size of OEP21 is limiting the usage of electron microscopy for structural elucidation. In order to comply the requirements for the NMR spectroscopic analysis, issues in OEP21 production and refolding in detergent micelles had to be overcome. Therefore, the optimization of sample conditions was performed.

The second objective was to obtain functional information on the metabolite transport by using NMR spectroscopy and further reliable biochemical methods. Based on the high-resolution structure of OEP21, the impact of the main metabolites in chloroplasts (ATP and GAP) on OEP21 was investigated. Using the obtained results and additional MD simulations (in collaboration with Prof. Dr. Martin Zacharias, Physics Department, Technical University Munich) a biochemical assay, using OEP21 incorporated into liposomes, was established, focusing on the GAP transport and the influence of structural features within the pore by mutagenesis as well as of ATP.

These results give a profound overall picture of OEP21, which trigger further research in various directions.

The mitochondrial ion channel hVDAC1

The second project deals with the mitochondrial β-barrel membrane protein hVDAC1 and its ability to form oligomers. The alteration of the oligomeric state in turn is defining its

function, since it is assumed to primarily shuttle metabolites in a monomeric state, whereas in an oligomeric state it functions as a channel for mainly pro-apoptotic cytochrome c release.

The first objective in this project was to apply hVDAC1 as a model system to establish a novel nanodisc-based assay in order to probe membrane protein oligomerization. The foundational concept relies on the cleavable GB1-fusion to hVDAC1 and the subsequent determination of the separated GB1 concentration. Reversely, GB1 attached to the MSP verifies this concept and enables to quantify membrane proteins, for which a GB1-tag is not applicable.

The second objective was to apply this established method on hVDAC1 inserted into MSP1D1 and MSP1D1ΔH5 nanodiscs, to screen the impact of different assembly conditions on the quantity of protein insertion.

By using the GB1-fusion construct to either the membrane protein or to the MSP, a reliable and efficient method was established to quantify membrane proteins in phospholipid nanodiscs. This gives the possibility to study membrane proteins in a defined oligomeric state.

3. Material and methods

3.1. Materials

3.1.1. Standard chemicals

If not stated otherwise the used chemicals are obtained by the following companies:
Agilent Technologies (USA), BioRad Laboratories (USA), Biozyme Scientific GmbH (Germany), Carl Roth, Cytiva (former GE Healthcare Life Sciences, USA), Life Technologies (USA), Merck KGaA (Germany), New England Biolabs (USA), PanReac AppliChem GmbH (Germany), Promega (USA), Roche (Germany), Santa Cruz Biotechnology (USA), Serva Electrophoresis GmbH (Germany), Sigma Aldrich (Germany), Thermo Fischer Scientific (USA), Th. Geyer GmbH & Co. KG (Germany), VWR (Germany).

3.1.2. Software

The following Software was used: Topspin and Sparky for NMR spectra analysis, Chimera for structural representation of the proteins, Image J for densiometrical quantification of proteins via SDS-PAGE analysis, OriginPro 9G for curve fitting and determination of the inflection point, Photoshop and Illustrator for graphical editing.

3.1.3. Media

3.1.3.1. LB and SOC medium

LB Medium was prepared by adding 25 g to 1L H_2O and subsequent autoclaving. It consists out of 10 g/L Tryptone, 5 g/L yeast extract and 10 g/L NaCl. SOB medium consists of 2 % (w/v) tryptone, 0.5 % (w/v) yeast extract, 8.56 mM NaCl, 2.5 mM KCl, 10 mM $MgCl_2$, 10 mM $MgSO_4$ and 20 mM glucose.

3.1.3.2. M9 minimal medium

Components of 1000x trace elements are given in **Table 1** and the M9 minimal medium is prepared using the components listed in
Table 2.

Table 1: Detailed composition of 1000x trace elements.

Component	Amount per 100 mL
EDTA	5 g
$FeCl_3$ x 6 H_2O	0.83 g
$ZnCl_2$	84 mg
$CuCl_2$ x 2 H_2O	13 mg
$CoCl_2$ x 6 H_2O	10 mg
H_3BO_3	10 mg
$MnCl_2$ x 6 H_2O	1.6 mg

Table 2: Detailed composition of M9 minimal medium.

Component	Amount per Liter
Na_2HPO_4	6 g/L
KH_2PO_4	3 g/L
NaCl	0.5 g/L
NH_4CL (^{15}N)	1 g/L
Antibiotics	According construct
Biotin	1 mg/L
Thiamine	1 mg/L
$MgSO_4$	2 mL of 1M stock solution in D2O
D-glucose	10 mL of 20 % (w/v) in D2O
$CaCl_2$	0.2 mL of 0.5 M stock solution in D2O
Trace elements	1 mL stock solution (1000x) in D2O

3.1.4. Primers

The list of primers, which were used are shown in **Table 3**. All primers, beside sequencing primers, were self-designed and produced by Sigma Aldrich (Germany).

Table 3: List of used primers.

Name	Sequence	Description
OEP21_K19A_fwd	TCCAAAGCACTAAAAATCCACGCC**GCG**GAAAAACTTCGAATCGACACCAAC	Single point mutation of Lys19 to Ala
OEP21_K19A_rev	GTTGGTGTCGATTCGAAGTTTTTC**CGC**GGCGTGGATTTTTAGTGCTTTGGA	
OEP21_R51A_fwd	CCGAGTTCTGGAAGTGCGCTCATT**GCG**CATTTTTATCCCAATTTTTCAGCAACGCTTGGG	Single point mutation of Arg51 to Ala
OEP21_R51A_rev	CCCAAGCGTTGCTGAAAAATTGGGATAAAAATG**CGC**AATGAGCGCACTTCCAGAACTCGG	
OEP21_R66A_fwd	GCAACGCTTGGGGTTGGTGTG**GCG**TATGATAAACAAGATTCTGTAGGAGTG	Single point mutation of Arg66 to Ala
OEP21_R66A_rev	CACTCCTACAGAATCTTGTTTATCATA**CGC**CACACCAACCCCAAGCGTTGC	
OEP21_R84A_fwd	GGAGTGAGATATGCTAAGAATGATAAGTTA**GCG**TATACTGTACTTGCTAAGAAGACGTTTCCT	Single point mutation of Arg84 to Ala
OEP21_R84A_rev	AGGAAACGTCTTCTTAGCAAGTACAGTATA**CGC**TAACTTATCATTCTTAGCATATCTCACTCC	
T7 Promotor	TAATACGACTCACTATAGGG	Sequencing Primer
T7 Terminator	GCTAGTTATTGCTCAGCGG	Sequencing Primer

3.1.5. Physical properties

Physical properties of all proteins were calculated using the online tool ProteinCalculator v3.4 http://protcalc.sourceforge.net and are listed in **Table 4**.

Table 4: Physical properties of all initial proteins.

Protein	MW [Da]	ε_{A280} [$cm^{-1}M^{-1}$]	pI	ΣAA
wtOEP21	20443.9434	34280	9.51	177
OEP21-His_6	22057.623	34280	9.41	189
hVDAC1-His_6	30772.5117	36840	8.59	291
GB1-Thr-hVDAC1-His_6	39222.6914	46370	7.03	360
MSP1D1	22043.8672	17780	5.92	190
His_6-TEV-MSP1D1	23661.5703	19060	6.46	202
MSP1D1ΔH5	19487.9551	17780	5.69	168
His_6-TEV-MSP1D1ΔH5	21105.6582	19060	6.38	180
GB1-Thr-MSP1D1ΔH5	26974.1934	27310	5.26	238
His_6-TEV-GB1-Thr-MSP1D1ΔH5	28591.8965	28590	5.80	150

3.2. Biochemical methods

3.2.1. Single point mutation

Single point mutations were performed using primers listed in **Table 3** in chapter 3.1.4 and the QuikChange Lightning Site-Directed Mutagenesis Kit (Agilent Technologies). The following table (**Table 5**) lists the components and the corresponding amount.

Table 5: Composition and pipetting scheme for site-directed mutagenesis.

Component	Amount [µL]
QCL Buffer	2.5
QuikSolution	0.75
dNTPs	0.5
Primer fwd	0.65
Primer rev	0.65
Plasmid	1
Polymerase	0.5
H_2O	18.45

Sequence with certain temperature was applied, starting with 2 min at 95 °C, followed by 30 times the cycle of 30 sec at 95°, 30 sec X °C and 7 min 68 °C and final 10 min at 68 °C. The annealing temperature X was set according the specific primer in a range of 56–62 °C. Afterwards, Dpn I digestion was performed for 1 h at 37 °C by adding 1 µL of Dpn I (10 U/µL). The resulting plasmid was transformed in *E.coli* XL10 competent cell and plate on an agar plate with 100 µg/mL ampicillin. Colonies were grown overnight at 37 °C, picked and transferred

into 5–10 mL LB medium, 2 % Glucose, 100 µg/mL ampicillin and incubated at 37 °C overnight. Plasmid extraction was performed using Wizard® Plus SV Minipreps DNA Purification System (Promega) according its protocol. The extracted plasmids were sent to Eurofins Genomics or Genewiz®, respectively using a T7 promoter or terminator (**Table 3**) as sequencing plasmid. Resulting DNA sequence was analyzed using the software SnapGene viewer and the online tool MultAlin http://multalin.toulouse.inra.fr/multalin/. [72]

3.2.2. Protein production and purification

3.2.2.1. OEP21-His_{10}

In the following OEP21-His_{10} is abbreviated as OEP21, whereas the OEP21 construct without His-tag is named as wtOEP21.

Protein expression of OEP21 was carried out using a pET21a vector transformed into *E.coli* BL21(DE3) cells. Transformation was carried out using a heat shock of 30 sec at 42 °C after 30 min incubation on ice followed by adding SOC medium and an incubation at 37 °C for 1 hour. Afterwards, *E.coli* cells were inoculated in 25 mL LB medium with 2 % glucose, 100 µg/mL ampicillin and incubated overnight at 37 °C while shaking. The preculture were then inoculated in 1 L LB medium containing 100 µg ampicillin. The culture grew at 37 °C while shaking till an OD_{600} of 0.6–0.8 was reached. Expression of OEP21 was induced by adding 1 mM IPTG. After 4–5 hours shaking the cells were harvested by centrifugation at 4 °C with 6000 rpm for 20 min. The cell pellet was stored by -80 °C.

For purification the cells were resuspended in 50 mM Tris pH 8.0, 100 mM NaCl, 1 mM EDTA, 2 mM DTT. After adding a protease inhibitor tablet and a tip of spatula of lysozyme the cells were incubated for 30 min on ice. Cell lysis was performed by using sonication (30% amplitude, 1 sec pulse, 2 sec break) and afterwards 1 U/mL DNase I and 5 mM $MgCl_2$ were added and 1 hour incubated while shaking at 4 °C. Lysate was spun down for 20 min at 18000 rpm. The obtained pellet was resuspended and washed with 20 mM Tris pH 8.0, 100 mM NaCl, 1 mM EDTA, 1 % Triton X-100 and afterwards pelletized again. The washing step was repeated twice without Triton X-100. The final pellet was dissolved in 6 M GdmCl, 50 mM Tris pH 8.0, 100 mM NaCl and 5 mM BME by shaking for couple of hours or overnight. Afterwards the dissolved inclusion bodies were centrifuged for 20 min at 18000 rpm and the supernatant was applied on 4 mL NiNTA resin (Ni Sepharose excel, GE Healthcare) to perform a gravity flow affinity chromatography. After incubation of 1–2 h it was washed with 10 mM Imidazole, without BME and followed by elution with 500 mM Imidazole, without BME. The elution fraction was dialyzed overnight in 5 L 20 mM Tris pH 8.0, 100 mM NaCl, 1 mM ETDA. The

precipitation was then pelletized using centrifugation for 20 min at 18000 rpm. The pellet was dissolved for a couple of hours in 6 M GdmCl, 50 mM NaP_i pH 8.0, 100 mM NaCl, 5 mM EDTA and 10 mM DTT with a final concentration of 5 mg/mL. The protein solution could be stored at -80 °C after being flash freezed in liquid nitrogen or directly used for further refolding step.

For refolding 5 mL of OEP21 in GdmCl-buffer 1 drop per 20 sec was added using a peristaltic pump (P-1, single channel, GE Healthcare) while stirring to 50 mL of 20 mM NaP_i pH 6.0, 50 mM NaCl, 1 mM EDTA, 3 mM DTT, 10 % (v/v) Glycerol, 2mM ATP and 1 % (m/v) LDAO. After overnight stirring, the solution was centrifuged for 20 min at 18000rpm to remove precipitation. Afterwards the refolded protein was concentrated up to a final volume of 5 mL to perform a size exclusion chromatography (ÄKTA pure system, column: HiLoad™ 16/600 Superdex™ 200 pg, GE) by using 20 mM NaP_i pH 6.0, 50 mM NaCl, 0.5 mM EDTA, 5 mM DTT, 5 mM ATP and 0.1 % (m/v) LDAO. The main peak was collected and concentrated for further analysis.

If necessary a detergent exchange was performed. Therefore OEP21 in LDAO micelles was applied on 3–4 mL NiNTA resin, incubated for 1–2 h and subsequently washed with 30–50 mL in 3 mL steps using the buffer with the specific detergent, e. g. deuterated LDAO. OEP21 was eluted using the specific buffer with additional 500 mM Imidazole. The elution fraction was concentrated and a buffer exchange was conducted with an illustra™ NAP™-5 column (GE Healthcare).

3.2.2.2. wtOEP21

Expression of wtOEP21 in inclusion bodies using a pET21b vector and subsequent cell lysis was performed as described in chapter 3.2.2.1. After washing of the inclusion bodies, the pellet was dissolved in freshly prepared 8 M Urea and 40 mM HEPES pH 7.9 and subsequently was applied on SP Sepharose Fast Flow (GE) resin and was incubated for 1–2 h. The protein was washed with 10 CV 8 M Urea and 40 mM HEPES pH 7.9 and afterwards eluted with 100 mM NaCl. The elution fraction was dialyzed in 20 mM Tris pH 8.0, 100 mM NaCl and 1 mM EDTA. Precipitated protein was centrifuged at 4 °C for 20 min at 18000 rpm and subsequent dissolving in 6 M GdmCl, 50 mM Tris pH 8.0, 100 mM NaCl, 5 mM EDTA and 10 mM DTT. The final concentration was adjusted to 5 mg/mL. The protein solution was stored at -80 °C, after flash freezing in liquid nitrogen or directly used for further refolding step according chapter 3.2.2.1.

3.2.2.3. hVDAC1 / GB1-hVDAC1

In the following the purification steps are valid for both constructs hVDAC1 and GB1-hVDAC1.

Protein expression of hVDAC1 was performed using a pET21a vector (Novagen) transformed into *E.coli* BL21(DE3) cells. Transformation and expression were carried out as described in chapter 3.2.2.1.

For purification the cells were resuspended in 50 mM Tris pH 7.0, 250 mM NaCl, 20 mM BME. After adding protease inhibitor tablet and a tip of spatula of lysozyme, the cells were incubated for 30 min on ice. Cell lysis was performed by using sonication (30 % amplitude, 1 sec pulse, 2 sec break). Afterwards 1 U/mL DNase I and 5 mM $MgCl_2$ were added, followed by an 1 hour incubation at 4 °C while shaking. Lysate was spun down for 20 min at 18000 rpm. The obtained pellet was resuspended in 50 mM Tris pH 7.0, 250 mM NaCl, 20 mM BME and 1 % Triton X-100 and afterwards pelletized again. The washing step was repeated twice without Triton X-100. The final pellet was dissolved in 6 M GdmCl, 50 mM Tris pH 8.0 and 100 mM NaCl by shaking for couple of hours or overnight. Afterwards the dissolved inclusion bodies were centrifuged again for 20 min at 18000 rpm and the supernatant was applied on 4 mL NiNTA resin (Ni Sepharose excel, GE Healthcare) to perform a gravity flow affinity chromatography. After incubation of the protein solution, it was washed with 10 mM Imidazole and followed by elution with 500 mM Imidazole. The elution fraction was dialyzed overnight in 5 L 20 mM Tris pH 7.5, 50 mM NaCl, 1 mM ETDA and 10 mM BME. The precipitation was then pelletized using centrifugation for 20 min at 18000 rpm. The pellet was dissolved for couple of hours in 6 M GdmCl, 100 mM NaP_i pH 7.0, 100 mM NaCl, 1 mM EDTA and 5 mM DTT with a final concentration of 5 mg/mL. The protein solution could be stored at -80 °C after flash freezing in liquid nitrogen or directly used for further refolding step.

For refolding 10 mL of hVDAC1 in GdmCl-buffer 1 drop per 20 sec were added using a peristaltic pump (P-1, single channel, GE Healthcare) while stirring to 100 mL of 25 mM NaP_i pH 7.0, 100 mM NaCl, 1 mM EDTA, 5 mM DTT and 1 % (m/v) LDAO. The solution continued stirring for a couple of hours before it was dialyzed overnight in 5 L 10 mM NaP_i pH 6.5, 1 mM EDTA and 3 mM DTT. To remove precipitation the solution was centrifuged for 20 min at 18000rpm. Next a cation exchange chromatography was performed using a 5 mL HiTrap SP Sepharose FF. Buffer A contained 10 mM NaP_i pH 6.5, 5 mM DTT and 0.1 % (m/v) LDAO, whereas Buffer B contained additionally 1 M NaCl. (System flow 1.5 mL/min, up to 50 % buffer B within 16.5 CV). Finally the fractions containing the correctly folded hVDAC1 can be concentrated up to 300–500 µM for subsequent nanodisc assembly and further analysis.

3.2.2.4. MSP

The following protocol was applied for all used MSP constructs including His_6-GB1-Thrombin-MSP1D1ΔH5. Protein expressions of diverse MSP constructs were performed using a pET21a vector transformed into *E.coli* BL21(DE3) cells. Transformation was carried out using a heat shock of 30 sec at 42 °C after 30 min incubation on ice followed by adding SOC medium and an incubation at 37 °C for 1 hour. Afterwards *E.coli* cells were inoculated in 25 mL LB medium with 2 % Glucose and 35 µg/mL kanamycin and incubated overnight at 37 °C while shaking. The preculture was then inoculated in 1L LB medium containing 35 µg kanamycin. The culture grew at 37 °C while shaking until an OD_{600} of 0.6–0.8 was reached. Expression of MSP was induced by adding 1 mM IPTG. After 4–5 hours shaking at 37 °C the cells have been harvested by centrifugation at 4 °C, with 6000 rpm for 20 min. Afterwards, the cell pellet was stored by -80 °C.

For purification the cells were resuspended in 50 mM Tris/HCl pH 8.0, 500 mM NaCl, 1 mM EDTA and 1 % (v/v) Triton X-100. After adding a protease inhibitor tablet and a tip of spatula of lysozyme the cells were incubated for 30 min on ice. Cell lysis was performed by using sonication (30 % amplitude, 1 sec pulse, 2 sec break) and afterwards 1 U/mL DNase I and 5 mM $MgCl_2$ were added and 1 hour incubated while shaking at 4 °C. Lysate was spun down for 20 min at 18000 rpm. The obtained supernatant was applied on 4 mL NiNTA resin (Ni Sepharose excel, GE Healthcare) to perform a gravity flow affinity chromatography. After incubation of 1–2 h, four washing steps were performed. First with 50 mM Tris/HCl, 500 mM NaCl, 1 % (v/v) Triton X-100, second with 50 mM Tris/HCl, 500 mM NaCl, 50 mM sodium cholate, third with 50 mM Tris/HCl, 500 mM NaCl and fourth with 50 mM Tris/HCl, 500 mM NaCl and 20 mM Imidazole. Afterwards the MSP was eluted by applying 50 mM Tris/HCl, 500 mM NaCl and 750 mM Imidazole. The eluted fraction was dialyzed overnight against 5 L 50 mM Tris/HCl, 20 mM NaCl, followed by a TEV cleavage by adding 1 mM EDTA, 2 mM DTT and TEV protease (1 A280 TEV for 100 A280 MSP). After complete cleavage MSP was dialyzed overnight against 5 L 50 mM Tris/HCl pH 8.0, 500 mM NaCl. To remove the His-Tag and not cleaved MSP a reverse NiNTA affinity chromatography was conducted. Therefore the protein was incubated for 1–2 h on the resin. The flowthrough was collected and the column was subsequently washed with 50 mM Tris/HCl pH 8.0, 500 mM NaCl and 20 mM Imidazole. Dialyzing of the flowthrough fraction was carried out overnight against 5 L 20 mM Tris/HCl, 100 mM NaCl and 0.5 mM EDTA. Finally the protein was concentrated up to 600–800 mM, portioned in 1 mL aliquots, flash frozen and stored at -80 °C.

3.2.2.5. Isotope labeling of proteins

Isotope labeling of proteins was performed following the protocol of Goto *et al.* (1999) [73]. Therefore, a D_2O adaption had to be performed, starting with an overnight culture was prepared as described in chapter 3.2.2.1. 5 mL of grown preculture was spun down at 2500 g for 10 min and resuspend in 10 mL LB medium with 2 % glucose and corresponding antibiotics and let it grew overnight at 37 °C. Afterwards 5 mL was spun down again with subsequently resuspension of the cell pellet in 10 mL M9 D_2O with 2 % glucose and corresponding antibiotics. The cell culture was incubated at 37 °C for around 8 h and afterwards diluted to a total volume of 50 mL. After growing overnight at 37 °C, the preculture was inoculated in 1 L main culture. Expression and harvesting by induction with IPTG proceed as described in chapter 3.2.2.1. For additional ^{13}C-labeling 2 g/L deuterated ^{13}C-glucose is added to the M9 medium instead of ^{12}C-glucose.

For specifically label proteins at position Ala-$^{13}C_{\beta}$, Ile-$^{13}C_{\delta1}$, Leu-$^{13}C_{\delta2}$ and Val-$^{13}C_{\gamma2}$ and Phe-$^{15}N_H$ and Tyr-$^{15}N_H$ (termed as ILVAFY) precursors had to be added 1 h prior induction. Therefore, the LV precursor ~25 mL of M9 medium was titrated to pH 12.5 with NaOD, 300 µL precursor was added and incubated for 1 h at RT and titrated back to pH 7.0 with DCl. Alanine precursor was prepared by solubilization of 2 g/L succinic acid d6 in ~40 mL M9 medium, adjusting pH to 7.0 and adding 250 mg/L L-alanine-3-^{13}C. In addition to LV- and A-precursor 80 mg/L L-tyrosine-^{15}N, 80 mg/L L-phenylalanine-^{15}N and 75 mg/L 2-Ketobutyric4-^{13}C, 3,3-D2 were added to the main culture. Subsequent expression was performed as described above.

3.2.3. Nanodisc assembly of hVDAC1/GB1-hVDAC1 in MSP1D1ΔH5 and MSP1D1

In the following the nanodisc assembly is described by using GB1-hVDAC1, but can be directly transferred to nanodiscs assemblies using hVDAC1.

GB1-hVDAC1 nanodiscs were assembled using different GB1-hVDAC1 to MSP ratios listed in **Table 6** and **Table 7**. The final GB1-hVDAC1 concentration for each assembly was 50 µM. A lipid composition of 75 % DMPC and 25 % DMPG dissolved in 20 mM Tris pH 7.5, 100 mM NaCl, 0.5 mM EDTA and 100 mM Sodium cholate hydrate was used.

Table 6: Ratios of GB1-hVDAC1 to MSP1D1ΔH5 used during the nanodisc assembly. *Concentrations given in µM for GB1-hVDAC 1 and MSP1D1ΔH5 and in mM for lipids, respectively.*

GB1-hVDAC1: MSP1D1ΔH5	c (GB1-hVDAC1) [µM]	c (MSP1D1ΔH5) [µM]	c (DMPC/DMPG) [mM]
1:1	50	50	1.5
1:2	50	100	3
1:4	50	200	8
1:6	50	300	12
1:8	50	400	16

Table 7: Ratios of GB1-hVDAC1 to MSP1D1 used during nanodisc assembly. *Concentrations given in µM for GB1-hVDAC 1 and MSP1D1 and in mM for lipids respectively.*

GB1-hVDAC1: MSP1D1	c (GB1-hVDAC1) [µM]	c (MSP1D1) [µM]	c (DMPC/DMPG) [mM]
1:1	50	50	2
1:2	50	100	4
1:4	50	200	8
1:6	50	300	12
1:8	50	400	16

The different nanodisc assemblies were incubated for 1 h at room temperature, followed by an incubation for 90 min on Bio-Beads SM2 (0.6 g/mL) using a shaking plate. A gravity flow affinity chromatography using NiNTA resin was performed to separate empty nanodiscs from with nanodiscs occupied by GB1-hVDAC1. The elution fraction containing the desired occupied discs were finally purified by using a size exclusion chromatography (ÄKTA pure system, column: Superdex™ 200 Increase 10/300 GL, GE). The SEC-buffer consisted of 20 mM NaP_i pH 7.0, 50 mM NaCl, 0.5 mM EDTA and 2 mM DTT. In case of the GB1-fusion construct the main peak was combined and bovine thrombin (20 units/mL dissolved in 25 mM NaP_i pH 7.5, 50 mM NaCl and 10 % Glycerol) was added with subsequent incubation overnight at room temperature. After SDS-PAGE analysis to determine complete cleavage a final size exclusion chromatography (ÄKTA pure system, column: Superdex™ 200 Increase 10/300 GL, GE) was performed. With hVDAC1 without GB1-fusion the SEC peak fractions were directly pooled and used for further analysis.

For empty GB1-MSP1D1ΔH5 nanodiscs, DMPC and DMPG lipids with a ratio of 3:1 were used. The assembly were performed with 100 µM GB1-MSP1D1ΔH5 and a MSP to lipids ratio of 1:45. The assembly of empty nanodiscs were done, following the same procedure as loaded nanodiscs, but without NiNTA affinity chromatography.

3.2.4. SDS-PAGE assay

Gels and buffers for SDS-PAGE assay were prepared according to **Table 8**. Sample preparation for SDS-PAGE analysis was prepared by combining 20 µL of protein solution and 10 µL of 2x Lämmli buffer and subsequent the incubation at 95 °C for 5 min. SDS-PAGE assays were performed by using a chamber from Hoefer Inc. (Germany) at 50 mA per gel for 30 min. Gels were stained with PageBlue™ protein staining solution containing Coomassie G-250 dye for 2 h at room temperature and distained in water afterwards.

Table 8: Composition of the required buffers and gels for SDS-PAGE analysis.

15 % separation gel		**80 mL**
	ddH2O	28.3 mL
	40 % Acrylamide	30 mL
	1.5M Tris pH 8.8	20 mL
	10 % SDS	800 µL
	10 % APS	800 µL
	TEMED	80 µL
6 % Stacking gel		**50 mL**
	ddH2O	29 mL
	40 % Acrylamid	7.5 mL
	0.5 M Tris pH 6.8	12.5 mL
	10 % SDS	500 µL
	10 % APS	500 µL
	TEMED	50 µL
2x Lämmli buffer		**10 mL**
	1M Tris pH 6.8	1.25 mL
	10 % (w/v) SDS	4.0 mL
	Glycerol	2.0 mL
	0.25 M EDTA	1.0 mL
	Bromophenol blue	4 mg
	BME	0.2 mL
10x SDS buffer		**1 L**
	Tris	30.29 g
	Glycine	150 g
	SDS	10 g

3.2.5. Liposome preparation

For preparing liposomes 10 mg/mL DMPC / DMPG (75 % / 25 %) were weighted, dissolved in chloroform, subsequent evaporated via nitrogen stream and stored overnight at -20 °C. Lipid mixture was dissolved in the respective buffer, followed by incubation in an ultrasound bath for 5 min. Afterwards 3–4 times freeze and thaw cycle were conducted by alternating usage of liquid nitrogen or a heating block (Thermomixer® C, Eppendorf), which was adjusted at 50 °C. Following the liposomes were produced by using an extruder (Avanti Polar Lipids). The applied membrane pore size was 0.1 µm (GE, Whatman Nuclepore polycarbonate hydrophilic

membrane). By bidirectional movement of the extruder up to 11 times the liposomes were formed and ready for immediate usage.

3.2.6. Protein crosslinking with BS^3

Bis[sulfosuccinimidyl]suberate (BS^3) is a reactive agent to crosslink oligomers via covalently formed stable amide bonds between the N-terminus of proteins. [74-76] Reaction of BS^3 with any protein is given in the following figure (**Figure 8**).

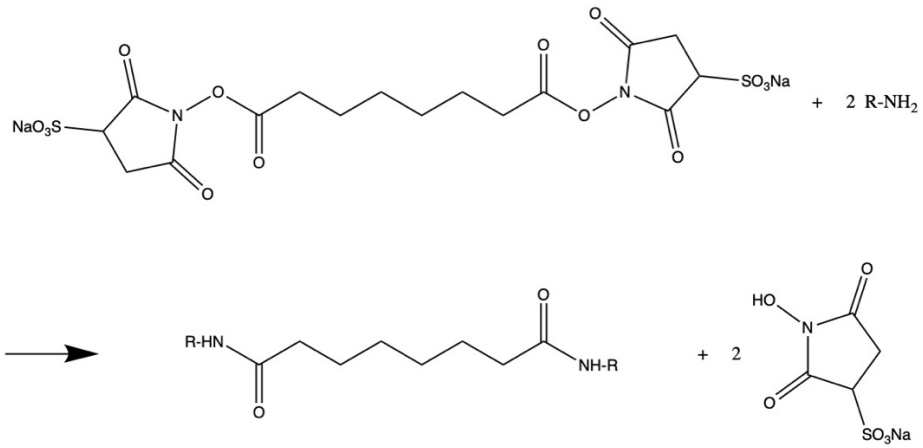

Figure 8: Reaction of BS^3 with N-terminus of any protein. *The amine reactive NHS-ester of the two ends of BS^3 reacts with the N-terminus of two proteins and links them by forming two amide bonds and N-hydroxysulfosuccinimide leaving group.*

Crosslinking is performed in 20 mM HEPES pH 6.5, 50 mM NaCl, 0.5 mM EDTA and 5 mM DTT with a final OEP21 concentration of 20–50 µM. The analyzed metabolites were added in a concentration of 1 mM or 5 mM, respectively. The total volume of each reaction was 50 µL. BS^3 was added in 50 times excess and incubated at room temperature for 30 min. Subsequently the reaction was quenched by 50 mM Tris pH 7.5 and incubated for 15 min. A SDS-PAGE analysis was performed afterwards.

In cases of high LDAO concentration, OEP21 was precipitated by trichloroacetic acid (TCA). Therefore 10 % (v/v) TCA was added to the reaction volume, incubated for 30 min on ice and subsequent centrifugation at 21000 rpm for 5 min. The protein pellet was washed three times with water and directly dissolved in SDS sample buffer for SDS-PAGE analysis.

3.2.7. ATP detection assay

ATP detection assay kit was purchased by Invitrogen™. It is applied to detect ATP by recording luminescence, which is released during the reaction of luciferin with ATP catalyzed by luciferase (reaction shown in **Figure 9**). In several steps, luciferin is transformed to a reactive and unstable species. By emission of photons the oxyluciferin reacts to its initial state [77].

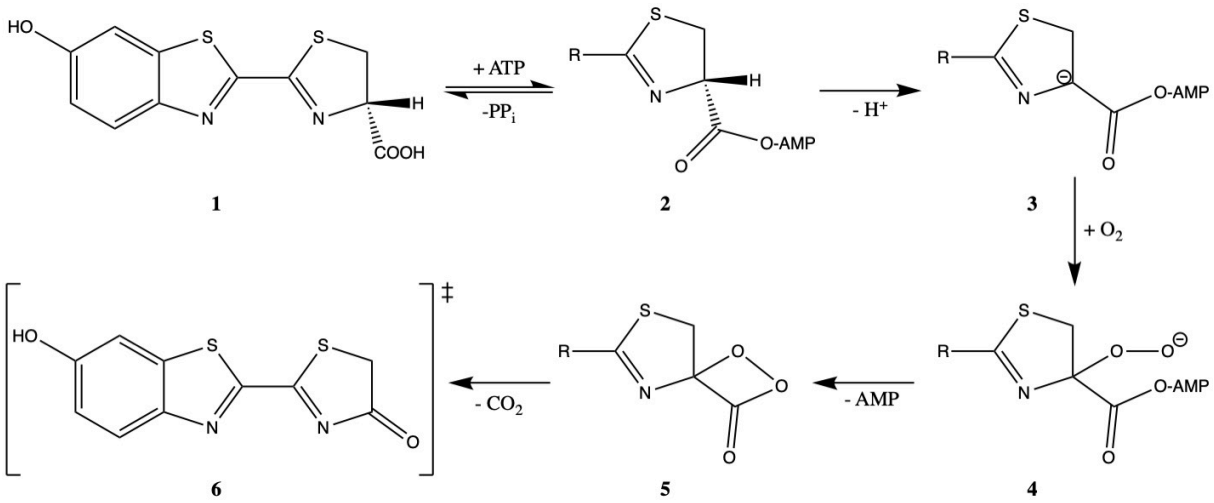

Figure 9: Reaction mechanism of luciferin with ATP catalyzed by luciferase. *First, adenylation of ATP to Luciferin (1) results after deprotonation in an carbanion (3). Further reaction with O_2 results in an hydroperoxide (4) and by leaving AMP a dioxetane (5) is formed. Decarboxylation results in an instable oxyluciferin (6), which in the last step photons are radiated during its decay.*

The ATP detection assay is conducted with ATP enclosed in liposomes to analyze the function of OEP21 as a channel protein. Therefore, liposomes were prepared as described above (chapter 3.2.5) with a buffer containing 25 mM HEPES pH 7.5, 5 mM $MgSO_4$, 5 mM BME and up to 1 M ATP. Afterwards an Illustra™ NAP™-5 column (GE Healthcare) for buffer exchange was conducted with 25 mM HEPES pH 7.5, 5 mM $MgSO_4$, 5 mM BME resulting in a 500 µg/mL liposome solution. If necessary detergent exchange of OEP21 was conducted in following steps. OEP21 was loaded on 3 mL Ni Sepharose excel histidine-tagged protein purification resin (GE Healthcare) to perform a detergent exchange of LDAO to Triton X-100 by washing with 60 mL 25 mM HEPES pH 7.5, 5 mM $MgSO_4$, 5 mM BME and 0.1 % Triton X-100 in 3 mL steps. The protein was eluted with additional 500 mM Imidazole. Buffer exchange was also conducted with an illustra™ NAP™-5 column (GE Healthcare) and 25 mM HEPES pH 7.5, 5 mM $MgSO_4$, 5 mM BME. A final concentration of 10–50 µM OEP21 was achieved. 10 mM D-luciferin and 12.5 mg/mL luciferase (firefly recombinant) were prepared using 25 mM HEPES pH 7.5, 5 mM $MgSO_4$, 5 mM BME. The following pipetting scheme was used (**Table 9**).

Table 9: Pipetting scheme of luciferin-luciferase assay using liposomes and OEP21 as channel protein. *The total reaction volume for the liposome assay is added up 100 µL.*

	Stock concentration	Final concentration	Liposomes	Liposomes + 0.1 % Triton X-100	Liposomes + 20 % Triton X-100	Liposomes + OEP21
Liposomes	500 µg/mL	150 µg/mL	30 µL	30 µL	30 µL	30 µL
OEP21	10–50 µM	0.5 µM	-	-	-	2 µL
Buffer	-	-	55 µL	53 µL	53 µL	53 µL
Luciferase	12.5 µg/mL	1.25 µg/mL	10 µL	10 µL	10 µL	10 µL
D-Luciferin	10 mM	0.5 mM	5 µL	5 µL	5 µL	5 µL
Triton X-100	0.1 % / 20 %	0.034 / 17 mM	-	2 µL	4 µL	-

A 96-well plate Lumitrec™ 200 (Greiner Bio-one) was used and sealed (EASYseal™, Greiner). The luminescence were read out by the multi-mode-microplate reader SpectraMax iD5 (Molecular Devices). Detection time was set to up to 4 h.

3.2.8. GAPDH assay

GAP is detected via GAPDH transforming NAD^+ to $NADH/H^+$ and thereby observing changes at a wavelength of 340 nm. The reaction proceeds as shown below (**Figure 10**) [44].

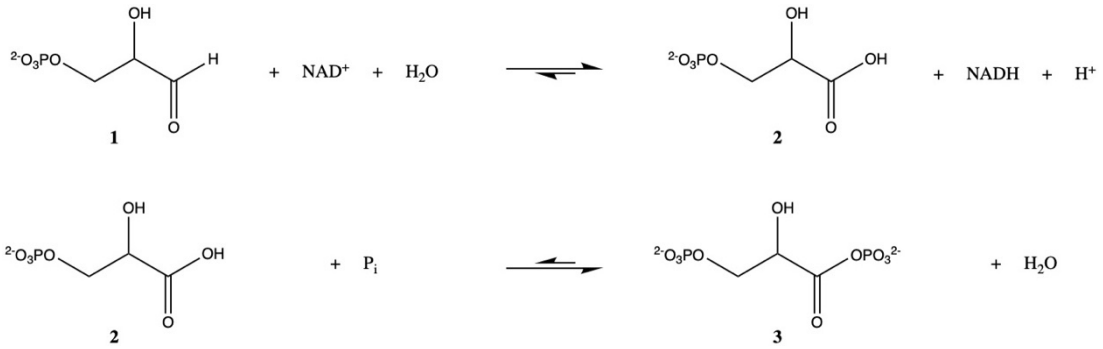

Figure 10: Reaction of GAP catalyzed by GAPDH. *Two step reaction of GAP (1) with NAD to 3-phosphoglycerate (2) and NADH/H^+ and further to 1,3-bisphosphoglycerate (3) catalyzed by GAPDH. Reaction of GAP to 1,3-bisphosphoglycerate is reversable.*

The GAPDH assay is conducted with GAP enclosed in liposomes to analyze the function of OEP21 as a channel protein. Therefore, liposomes were prepared as described above (chapter 3.2.5) with a buffer containing 50 mM KPi pH 7.5, 5 mM $MgSO_4$, 5 mM BME and 1 mM GAP. Afterwards an illustra™ NAP™-5 column (GE Healthcare) for buffer exchange was performed with 50 mM KPi pH 7.5, 5 mM $MgSO_4$, 5 mM BME resulting in a 500 µg/mL liposome solution. Detergent exchange of OEP21 was performed according chapter 3.2.7.

Following the final concentration of components was used in the reaction mixture 1mM NAD, 0.6 units and 10–50 µM OEP21 with the pipetting scheme below.

Table 10: Pipetting scheme of the GAPDH assay using liposomes and OEP21 as channel protein. *The total reaction volume for the liposome assay is added up 100 µL.*

	Stock concentration	Final concentration	Liposomes w/o OEP21	OEP21 w/o Liposomes	Liposomes + 0.1 % Triton X-100 Buffer	Liposomes + 20 % Triton X-100 Buffer	Liposomes + OEP21
Liposomes	500 µg/mL	150 µg/mL	30 µL	-	30 µL	30 µL	30 µL
OEP21	10–50 µM	0.1–01.5 µM	-	2 µL	-	-	2 µL
NAD	10 mM	0.2 mM	2 µL	2 µL	2 µL	2 µL	2 µL
GAPDH	0.22 mg/mL	67.5 µg/mL	30 µL	30 µL	30 µL	30 µL	30 µL
Triton X-100	0.1 % / 20 %	0.034 / 17 mM	-	-	2 µL	5 µL	-
Buffer	-	-	38 µL	66 µL	36 µL	33 µL	36 µL

A different approach of this assay is to prepare of liposomes with directly added OEP21, NAD and GAPDH resulting in liposomes containing OEP21 in the phospholipid bilayer with enclosed NAD and GAPDH. Thereby the effect of LDAO or Triton X-100 is decimated, in which OEP21 is solved in. For preparation 1–5 µM OEP21, 97.5 µg/mL GAPDH and 1–2 mM NAD is added to the lipid solution after 3–4 freeze and thaw cycles of the lipid solution and before production of liposomes using the extruder. Afterwards a buffer exchange was performed to remove remaining NAD and LDAO / Triton X-100 outside the liposomes. Following table (**Table 11**) is listing stock and final concentrations and the pipetting scheme for this approach.

Table 11: Pipetting scheme of the GAPDH assay using NAD and GAPDH enclosed liposomes and OEP21 added during liposome preparation. *The total reaction volume for the liposome assay is added up 100 µL.*

	Stock concentration	Final concentration	Reference Liposomes	Reference GAP + Triton X-100	Reference ATP	GAP	GAP + ATP
Liposomes	500 µg/mL	150 µg/mL	30 µL	30 µL	30 µL	30 µL	30 µL
GAP	50 mM	0.5–5 mM	-	1–10 µL	-	1–10 µL	1–10 µL
ATP	50 mM	0.5–5 mM	-		1–10 µL		1–10 µL
Triton X-100	20%	17 mM	-	5	-	-	-
Buffer	-	-	70 µL	65 - V_{GAP} µL	70 - V_{ATP} µL	70 - V_{GAP} µL	70 - V_{GAP} - V_{ATP} µL

Using multi-mode-microplate reader SpectraMax iD5 (Molecular Devices) and a 96-well plate (transparent, PS, F-bottom, Greiner Bio-one) the absorption at 260 nm and 340 nm of the reaction were detected up to 4 h. Prior the detection the 96-well plate was sealed using an EASYseal™ sealing film (Greiner).

3.2.9. Coupled GAPDH-PGK-luciferase assay

The coupled reaction of the enzymes glyceraldehyde 3-phosphate dehydrogenase (GAPDH), phosphoglycerate kinase (PGK) and luciferase was performed as another attempt to detect GAP translocation. The first reaction transforms GAP to 1,3-bisphosphoglycerate (**Figure 10**), which reacts further with ADP to 3-phosphoglycerate and ATP catalyzed by PGK (**Figure 11**) [44]. ATP generates the luminescence via luciferin-luciferase reaction (**Figure 9**) in the final step.

Figure 11: Reaction of 1,3-bisphosphoglycerate catalyzed by phosphoglycerate kinase. *Simplified dephosphorylation of 1,3-bisphosphoglycerate with ADP to 3-phosphoglycerate and ATP catalyzed by phosphoglycerate kinase.*

The coupled GAPDH-PGK-luciferase assay is used to determine the transport of GAP using GAP enclosed liposomes. Therefore liposomes were prepared as described above (chapter 3.2.5) with a buffer containing 50 mM KPi pH 7.5, 5 mM $MgSO_4$, 5 mM BME and 1 mM GAP followed by a buffer exchange using an illustra™ NAP™-5 column (GE Healthcare) to 25 mM KPi pH 7.5, 5 mM $MgSO_4$, 5 mM BME resulting in a 500 µg/mL liposome solution. The following table depicts the final concentration and the respective pipetting scheme (**Table 12**).

A 96-well plate Lumintrec™ 200 (Greiner Bio-one) and a multi-mode-microplate reader SpectraMax iD5 (Molecular Devices) was applied to read out the luminescence of the reaction. The 96-well plate was sealed using an EASYseal™ sealing film (Greiner). Detection time was set up to 4 h.

Table 12: Final concentrations and corresponding pipetting scheme of the coupled GAPDH-PGK-luciferase assay. *The total reaction volume for the liposome assay is added up 100 µL.*

	Concentrations	Liposomes w/o OEP21	OEP21 w/o Liposomes	Liposomes + 0.1 % Triton X-100 Buffer	Liposomes + 20 % Triton X-100 Buffer	Liposomes + OEP21
Liposomes	150 µg/mL	30 µL	-	30 µL	30 µL	30 µL
OEP21	1.8 µM	-	2 µL	-	-	2 µL
ADP	0.2 mM	2 µL	2 µL	2 µL	2 µL	2 µL
NAD	0.2 mM	2 µL	2 µL	2 µL	2 µL	2 µL
GAPDH	67.5 µg/mL	30 µL	30 µL	30 µL	30 µL	30 µL
PGK	70 µg/mL	2 µL	2 µL	2 µL	2 µL	2 µL
Luciferase	0.5 mM	10 µL	10 µL	10 µL	10 µL	10 µL
Luciferin	1.25 µg/mL	5 µL	5 µL	5 µL	5 µL	5 µL
Triton X-100	0.034 / 17 mM	-	-	2 µL	5 µL	-
Buffer	-	19 µL	47 µL	17 µL	14 µL	17 µL

3.3. Biophysical methods

3.3.1. CD spectroscopy

Circular dichroism spectra were recorded on a spectropolarimeter (Jasco J-715) equipped with a spectropolarimeter power supply (Jasco PS-150J), a nitrogen monitor (Jasco) and a temperature controller (Jasco PTC-348WI) connected to the circulation thermostat (Julabo F25). The resulting ellipticity Θ is used to calculate the molar ellipticity [Θ] with following equation. c is the concentration of the protein in µM, n is the number of peptide bonds of the protein. [78]

$$[\theta] = \frac{\theta \cdot 10^6}{1 \cdot c \cdot n}$$

For determining the melting temperature (T_m), the changes in ellipticity is detected at a certain wavelength, while increasing the temperature from 20–100 °C. T_m value was determined by curve fitting analysis of the inflection point of the resulting sigmoidal curve using the software OriginPro 9G.

3.3.2. NMR spectroscopy

Nuclear magnetic resonance spectroscopy (NMR spectroscopy) is a commonly applied method in protein biochemistry to study the structure and dynamics of proteins. It makes use of the magnetization of the spins within an atom or molecule and the alignment of them in an external applied magnetic field.

Solution state NMR spectroscopy has many advantages over other methods. For instance, compared to crystallography, the determination of dynamics within the protein is possible, such as enzyme turnovers, kinetics and folding. It can detect ligand and partner protein binding and can be used to solve protein structures in solution. However, protein NMR spectroscopy is just applicable for structure determination of small proteins (<50 kDa). Nevertheless, regarding proteins with a molecular weight of 900 kDa, analysis of binding and dynamics is possible using resonance assignment via mutagenesis and the detection of isolated methyl probes in a highly deuterated background [73]. Therefore, specifically ^{13}C-labeled methyl side chains (e. g. Ala-β, Ile- δ1, Leu-δ2 and Val-γ2) can be incorporated, with the advantage to gain additional side chain information and optimization of structure calculation. To gain the selective labeling of amino acids a suitable expression host is necessary. Insect and

mammalian cells are inefficient for these labeling strategies, whereas bacteria, e. g. *E.coli* cells are the better choice. [73, 79, 80] However, compared to other structural methods, NMR spectroscopy can be time-consuming. Nonetheless, with obtaining a large set of information from NMR spectroscopy, this method has a major part in structure determination of (membrane-) proteins, binding studies as well as for detecting protein dynamics multiple time scales. [81-83]

In principle there are two main spectroscopic methods: solution state and solid-state NMR spectroscopy. In the following the basics of the solution state NMR spectroscopy are described in more detail.

General principle of NMR spectroscopy

NMR spectroscopy take advantage of the spin alignment of an atom in an external applied magnetic field B_0. The energy E of the spins in the static magnetic field B_0 can be described with the magnetic moment $\vec{\mu}$ or by the gyromagnetic constant γ, the magnetic quantum number m_z and the Planck's constant h.

$$E = -\vec{\mu}\overrightarrow{B_0} = m_z \gamma h B_0$$

Nuclear spins undergo a precession motion around the direction of the magnetic field B_0 with the Lamour frequency ω_0. Spin ½ nuclei ($m_z = ½ , -½$) can be present in two possible orientations, α (low-energy state, parallel to B_0) and β (high-energy state antiparallel to B_0), which are populated according the Boltzmann distribution. The energy difference between these states can be calculated according to the equation shown below:

$$\Delta E = \frac{\gamma h B_0}{2\pi}$$

$$\omega_0 = \gamma B_0$$

The Boltzmann distribution can be calculated with the equation shown below and is resulting in a macroscopic polarization, i. e. in the net magnetization M_z.

$$\frac{n_\alpha}{n_\beta} = e^{\frac{\Delta E}{kT}} = e^{\frac{\gamma h B_0}{2\pi k T}}$$

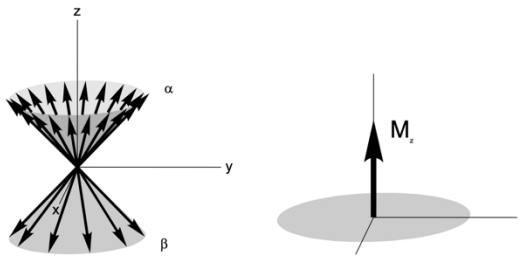

Figure 12: Spin precession around the external field B_0 and resulting z-magnetization. *[84]*

By applying a radiofrequency (rf) field B_1 the Boltzmann distribution is perturbed, if the energy of the irradiated radiofrequency is in resonance with the energy gap between the two energy states of the nuclear spin states. Depending on the direction of the radiofrequency pulse, the direction of the macroscopic magnetization can be adjusted, as required for a particular NMR experiment and turned into transverse magnetization in case of a 90° pulse from x or y direction (**Figure 13**).

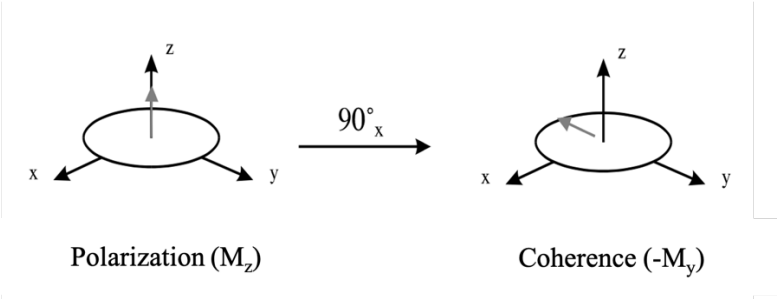

Figure 13: Simplified representation of a 90 degree rf pulse resulting in a magnetization M in the x,y-plane. *[84]*

This transverse magnetization $M_{x,y}$ (coherence) will undergo precession around the B_0 field, as well as a loss in spin coherence (T_2 relaxation, transverse relaxation) or a return to the Boltzmann equilibrium (T_1 relaxation, longitudinal relaxation). This leads to the observation of a typical free induction decay (FID) (**Figure 14**), where the decay of the NMR intensity is governed by T_2 relaxation. T_2 relaxation is occurring in the ms time scale and affect the line broadening of the signals, whereas T_1 relaxation is slower (seconds) and is responsible for the loss of signal intensity. To obtain a final NMR spectrum Fourier Transformation performed. [81, 85, 86]

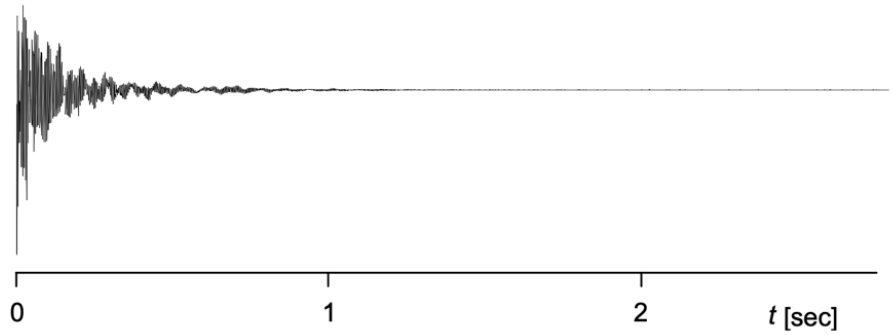

Figure 14: Representation of a free induction decay. *[84]*

The chemical shift of an atom is defined by its chemical surrounding, which in turns is equivalent with changes in Lamour frequency induced by the local electronic environment. The chemical shift is therefore within defined ranges for different atoms and molecular groups. A proton chemical shift for example is shifted into low field if a nitrogen is connected to it. As an example, a typical ^{1}H resonance for backbone NH group is 8–10 ppm and the corresponding ^{15}N chemical shift is between 110 and 140 ppm. Regarding $C_{\alpha}H$ groups, the chemical shift for protons is between 3.5 and 5 ppm, whereas for $^{13}C_{\alpha}$ the range is between 40 and 65 ppm. [87]

Since a protein does not only consist out of a single atom, the chemical shift are dependent on the chemical and electronical surrounding. Thereby the nuclei can also interact with other nuclei up to three chemical bonds via the electrons in the bonding orbitals. This interaction is called J coupling, also known as scalar coupling. It is another important factor in protein NMR spectroscopy. The contribution to the J coupling is defined by electrons of the involved bonds (typical magnitude of couplings in proteins are shown in **Figure 15**). By using the J-coupling structural information can be extracted, such as connectivities and angles. Thus, all multidimensional NMR experiments make use of the interaction through bonds, providing essential information on the connectivity between the atoms in the protein. In the following the 2D- and 3D-NMR spectra are described. [85, 88]

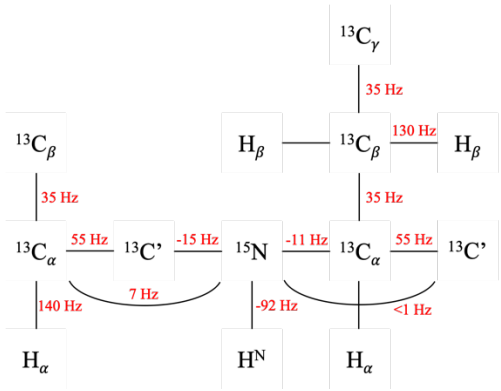

Figure 15: ^{1}J- and ^{2}J- coupling in proteins and the corresponding ranges depending on the involved atoms. *[88]*

[^{1}H,^{15}N]-HSQC/TROSY

Heteronuclear single quantum correlation (HSQC) is a simple 2D heteronuclear NMR experiment detecting an I and S spin (here ^{1}H and ^{15}N). In the following the pulse sequence (**Figure 16 A**) is given.

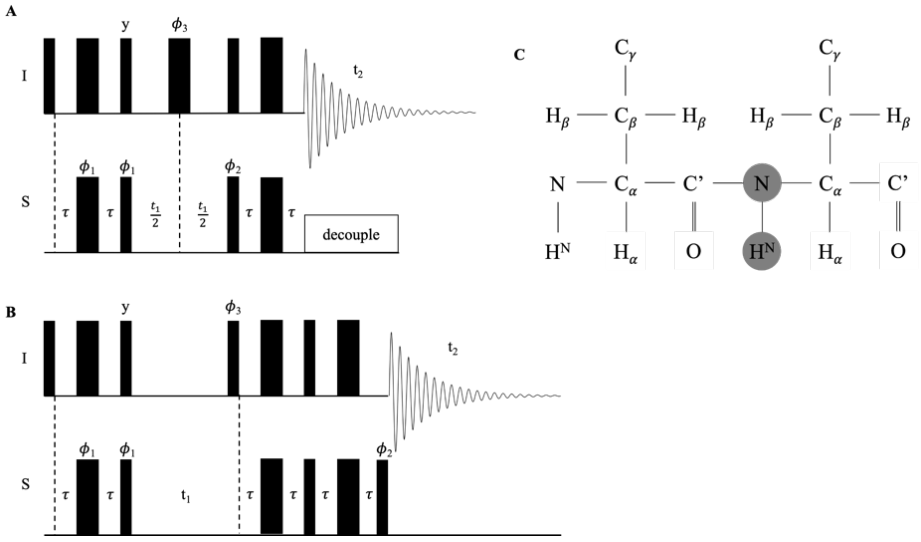

Figure 16: HSQC and TROSY experiments. *Pulse sequence of HSQC (**A**) and TROSY (**B**). [81]* ***C*** *Schematic representation of the involved nuclei (marked in grey). [85, 89]*

The experiment starts with the excitation of the proton spin, transfer of the magnetization to the ^{15}N spin, recording of the ^{15}N frequencies in an indirect manner, and back-transfer to ^{1}H for final direct detection. The HSQC takes advantage of the INEPT (Insensitive nuclei enhancement polarization transfer) method, which is part of all conventional multidimensional solution-state NMR experiments. [81, 86, 87] The INEPT sequence transfers magnetization from a sensitive nucleus with a high gyromagnetic ratio γ (such as protons, γ = 2.6752 x 10^8 Ts^{-1}) to a less sensitive nucleus with a small γ (here nitrogen, γ = -2.713 x 10^7 Ts^{-}

^{1}). [81] In case of the HSQC experiment, two INEPT sequences results in transfer from the I to the S spin and back to increase the sensitivity. In an HSQC spectrum every N-H-bond is visible, as well as side-chain amide moieties of Trp, Asn, Gln, Lys and Arg. This spectrum is typically one of the first spectra that is recorded of a particular protein and can be used as a fingerprint of its structural state. Unfolded or not correctly folded proteins are recognized by the low chemical shift dispersion of the resonances in the ^{1}H dimension. [81, 84]

Similar to a HSQC experiment, transverse relaxation-optimized spectroscopy (TROSY) is a highly applied method to reduce the signal linewidth and increase spectral quality especially for larger proteins. Large proteins are tumbling slowly in solution, which is leading to in line broadening effects, caused by fast T_2 relaxation. To reduce these line broadening effects and obtain an increase in the spectral quality, the TROSY pulse sequence is selecting the slowest-relaxing multiplet component of an NH spin pair. This principally leads to a drop in signal intensity to 25 % of the HSQC peak intensity. However, since favorable relaxation is active for the selected component, there is an overly gain in resolution and sensitivity for larger and deuterated proteins. The pulse sequence of a standard TROSY experiment is given in **Figure 16 B**. [81]

^{13}C-HMQC and 3D triple-resonance experiments (HNCA, HNCO, HNCACB)

The following experiments were applied to assign the backbone resonances of a protein. In this context, a short overview is given on the transfer of magnetization in these 3D experiments.

In a ^{13}C-HMQC experiment (heteronuclear multiple quantum coherence) the magnetization is transferred from ^{1}H to ^{13}C and back. In principle the transfer is similar to the HSQC, discussed before. In an HMQC experiment the H and X (here ^{1}H and ^{13}C) multiple quantum coherences evolve during the indirect evolution period, whereas in a HSQC experiment in-phase single quantum coherence of just the X nucleus (e. g. ^{15}N) is recorded. [81, 86, 87]

For a fully ^{13}C-labeled protein, every carbon nucleus within the protein can be directly detected. Using ^{13}C-labeled amino acids without additional ^{13}C-glucose added during protein expression, only a selected subset of carbon nuclei is labeled with ^{13}C, e.g. methyl carbons of Ile, Val, Leu and Ala, which facilitates assignment of these side-chain moieties. [89, 90]

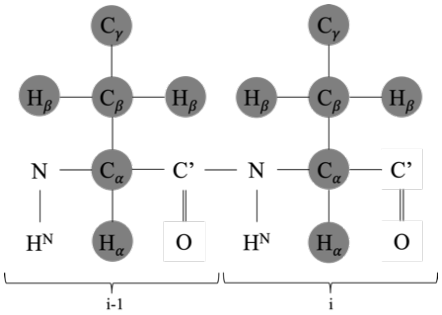

Figure 17: Schematic representation of the nuclei involved in the ^{13}C-HMQC. *[89]*

The nomenclature of the following 3D experiments is related to the nuclei involved in the magnetization transfer, e. g. meaning the HNCA is detecting proton and nitrogen of the amide group and the C_α, all located in the backbone of the protein. In this 3D experiments, the magnetization starts at the H^N and passes from ^{15}N to $^{13}C_\alpha$. Due to the fact, that transferring magnetization from ^{15}N spin to both the C_α^i and C_α^{i-1} of the previous amino acid is possible, this experiment provides sequential information required for sequence specific resonance assignment. In contrast, the HNCO experiment transfers the magnetization from the H^N to the backbone amide and further to the carbonyl C' and back. This experiment provides the chemical shifts of the carbonyl C'(i-1), which can be used for secondary structure estimation. The 3D HNCOCA experiment can be compared to the HNCA experiment, with the exception that just the C_α^{i-1} is detected and not its own C_α^i of the amino acid. Another highly useful 3D NMR experiment is the HNCACB, which contains most of the information required for backbone assignment. Beside H^N, N and C_α, the spectrum shows also the C_β of the own and preceding residue. Since for larger proteins the spectral quality decreases, the previously mentioned NMR spectra can be quite beneficial. [81, 89]

A schematic representation of HNCA (**A**), HNCO (**B**), HNCOCA (**C**) and HNCACB (**D**) is given in **Figure 18**. Here, the light grey marked nuclei are involved in the transfer of magnetization but the dark grey nuclei are given in the corresponding spectra.

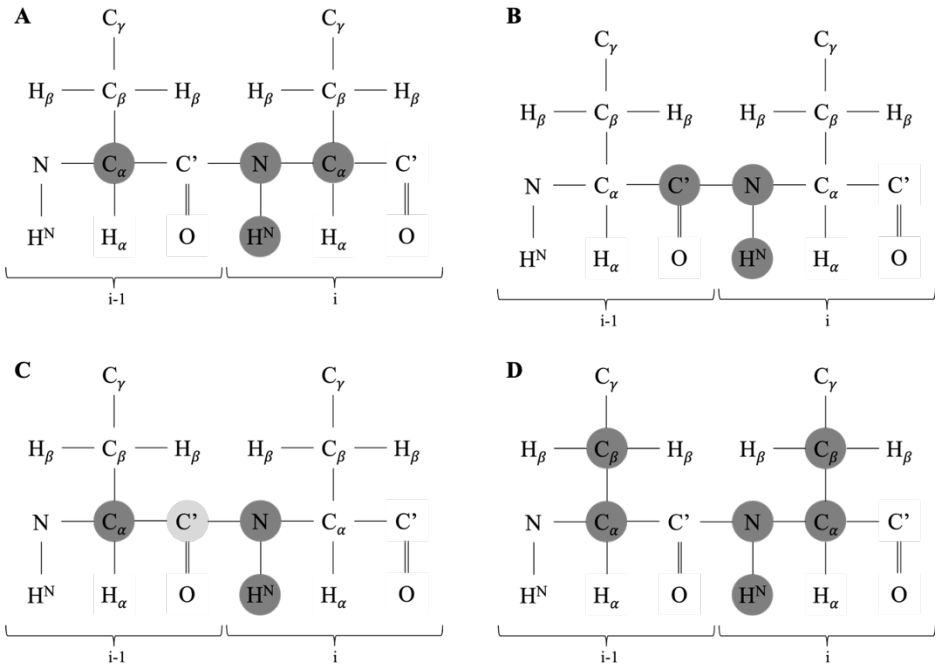

Figure 18: 3D-NMR experiments and the involved nuclei. *Schematic representation of the nuclei involved in HNCA (**A**), HNCO (**B**), HNCOCA (**C**) and HNCACB (**D**). [89]*

NOESY

In contrast to the previously mentioned NMR experiments, the NOESY crosspeaks (Nuclear Overhauser Effect spectroscopy) originate from dipole-dipole cross-relaxation effects instead of J-coupling and thereby is monitoring the through-space interactions of protons and is based on longitudinal cross-relaxation. This effect is only detectable if the protons are less than ~6 Å apart from each other. The distance between these protons is directly connected to the integral of the cross peak visible in the NOESY spectrum (r^{-6} relation). This peak intensity can then be converted into explicit pairwise distances between protons in the protein and subsequently used for structure calculation. [81, 86]

Paramagnetic relaxation enhancement (PRE)

Here, the paramagnetic probe 16-DOXYL stearic acid (16-DSA) was used, containing a free stable nitroxide radical. Compared to 5-DSA, the spin label is attached to C16 of the hydrocarbon chain in the hydrophobic core of the micelle. Therefore it leads to NMR signal reduction corresponding to amino acids in the protein that are located at the inside of the micelle, whereas amino acids located outside the micelle are not affected. [91] This effect is based on the magnetic dipolar interaction of the spin of unpaired electron of the nitroxide group and the nuclear spins in the protein, resulting in enhanced T_1 and/or T_2 relaxation, respectively.

This method is very valuable to quickly determine the location of a membrane protein in membrane or micelle. [92, 93]

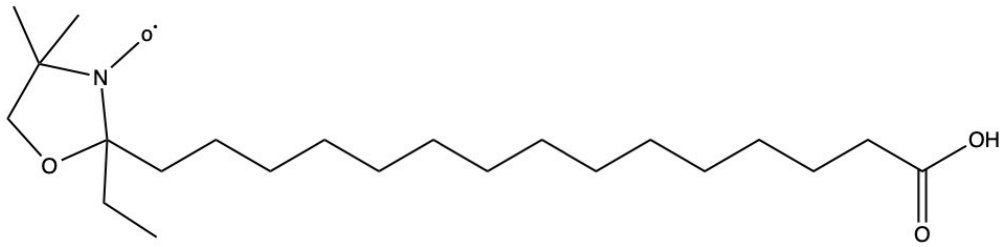

Figure 19: 16-DSA molecule with a free radical at the nitroxyl group located at C16.

In a NMR sample approximately one molecule 16-DSA per micelle were added. This was calculated after determining the exact LDAO concentration using the integrals of the H_2O and the CH_3-group signals in an 1D-^{1}H-NMR spectrum. With the exact LDAO concentration and its aggregation number of 76, meaning 76 LDAO molecules in a micelle, the concentration of 16-DSA could be determined and added to the NMR sample.

Sample preparation and NMR set-up

All NMR samples were prepared by adding 7 % D_2O of a total volume of 300 µL and for long-term measurements additional 3 µL of a solution prepared of 1 cOmplete™ EDTA-free protease inhibitor tablet (Roche) solved in 1 mL H_2O and 1 µL of 10 % (w/v) sodium azide. All following nuclear magnetic resonance experiments were conducted on Bruker systems (500 MHz, 600 MHz, 800 MHz, 900 MHz and 950 MHz) using cryogenic probes. Temperature were set according the measured protein. NMR spectra of OEP21 were recorded at 308K and 303K for hVDAC1. NMR spectra were processed using the software TopSpin (Bruker) and analyzed with NMRFAM Sparky [94].

4. Results

4.1. OEP21 and its mutants

4.1.1. OEP21 – expression and purification

Expression and purification of OEP21 was performed according chapter 3.2.2.1. **Figure 20 A** indicates an adequate amount of OEP21 after 5 h expression at 37 °C. Purification using Ni affinity chromatography reveals an insufficient binding to Ni resin, which indicates an overload of the resin by OEP21 (**Figure 20 B**). After repetition of the Ni affinity chromatography with the flowthrough fraction to increase the yield and subsequent precipitation of wash and elution fraction the protein was solubilized in GdmCl buffer to a final concentration of 5mg/mL. In total a yield of ~35 mg per 1 L culture solubilized in 6 M GdmCl could be achieved.

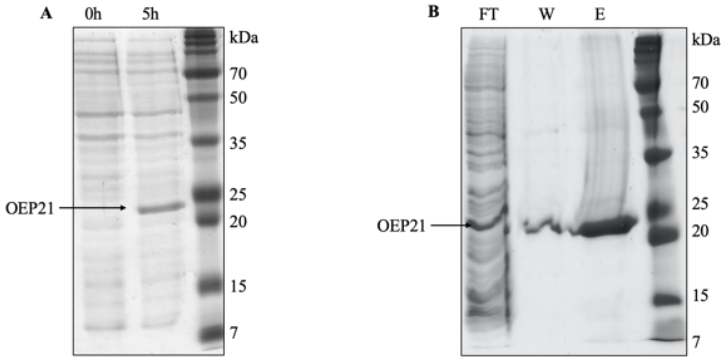

Figure 20: SDS-PAGE analysis of the expression and purification of OEP21. ***A*** *Expression of OEP21. Using E. coli BL21 (DE3) cells. Expression starts with 1mM IPTG at an OD of 0.6–0.8. Expression duration is 4–5h.* ***B*** *SDS-PAGE analysis of the purification of OEP21 using Ni affinity chromatography.*

The refolding of OEP21 had to be optimized, since the first purification attempts yielded in incorrectly folded protein, which was proven by CD and NMR spectroscopy. Using conditions as described in chapter 3.2.2.1, the following SEC profile could be attempt. As represented in Figure 21 the SEC results in several peaks, whereas all of them containing OEP21, while using NaP_i buffer with additional ATP. At a higher elution volume, LDAO concentration is increased as seen on the SDS gel. Comparing the SEC profile using NaP_i buffer, the SEC chromatogram of OEP21 in HEPES buffer without any metabolite (**Figure 21**) results in a single peak, followed by uneven absorbance that represent still some amount of OEP21 with higher LDAO concentrations. Regarding the yield of both buffer systems no

significant difference could be observed. The yield of the collected main fractions are displayed in **Table 13**.

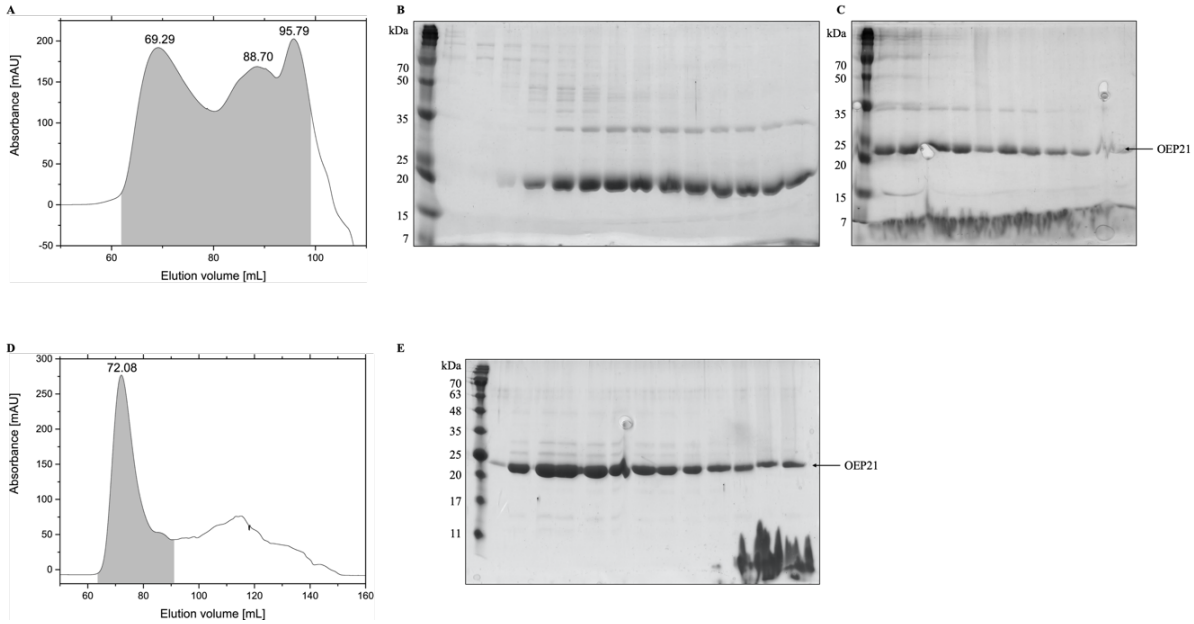

Figure 21: Size exclusion chromatography of OEP21 and its corresponding SDS-PAGE analysis of the main peak. *(grey).* ***A*** *Size exclusion chromatogram of OEP21 in NaP_i-Buffer pH 6.0 and 0.5mM ATP.* ***B, C*** *SDS-PAGE analysis of SEC fractions of OEP21 in NaP_i pH 6.0 and 0.5 mM ATP.* ***D*** *Size exclusion chromatogram of OEP21 in HEPES buffer pH 6.5 without metabolites.* ***E*** *SDS-PAGE analysis of main SEC fraction (grey) of OEP21 in HEPES pH 6.5 without metabolites.*

4.1.2. Single point mutation of OEP21 – expression and purification

Cloning of the single point mutation K19A, R51A, R66A and R84A of OEP21 was performed according protocol in chapter 3.2.1 with corresponding annealing temperatures of 58 and 62 °C, respectively. Plasmid extraction resulted in 20–50 ng/µL concentrations and were analyzed by Eurofins Genomics. After successful cloning the single point mutations were expressed and purified according the protocol for OEP21 with a final buffer consisting of HEPES pH 6.5 and without ATP. Expression and purification by gravity flow chromatography, using Ni resin resulted in the same SDS-PAGE analysis picture as OEP21 and therefore is not depicted. The SEC profiles of the mutants including corresponding SDS-PAGE analysis are similar as shown in the following figure (**Figure 22**).

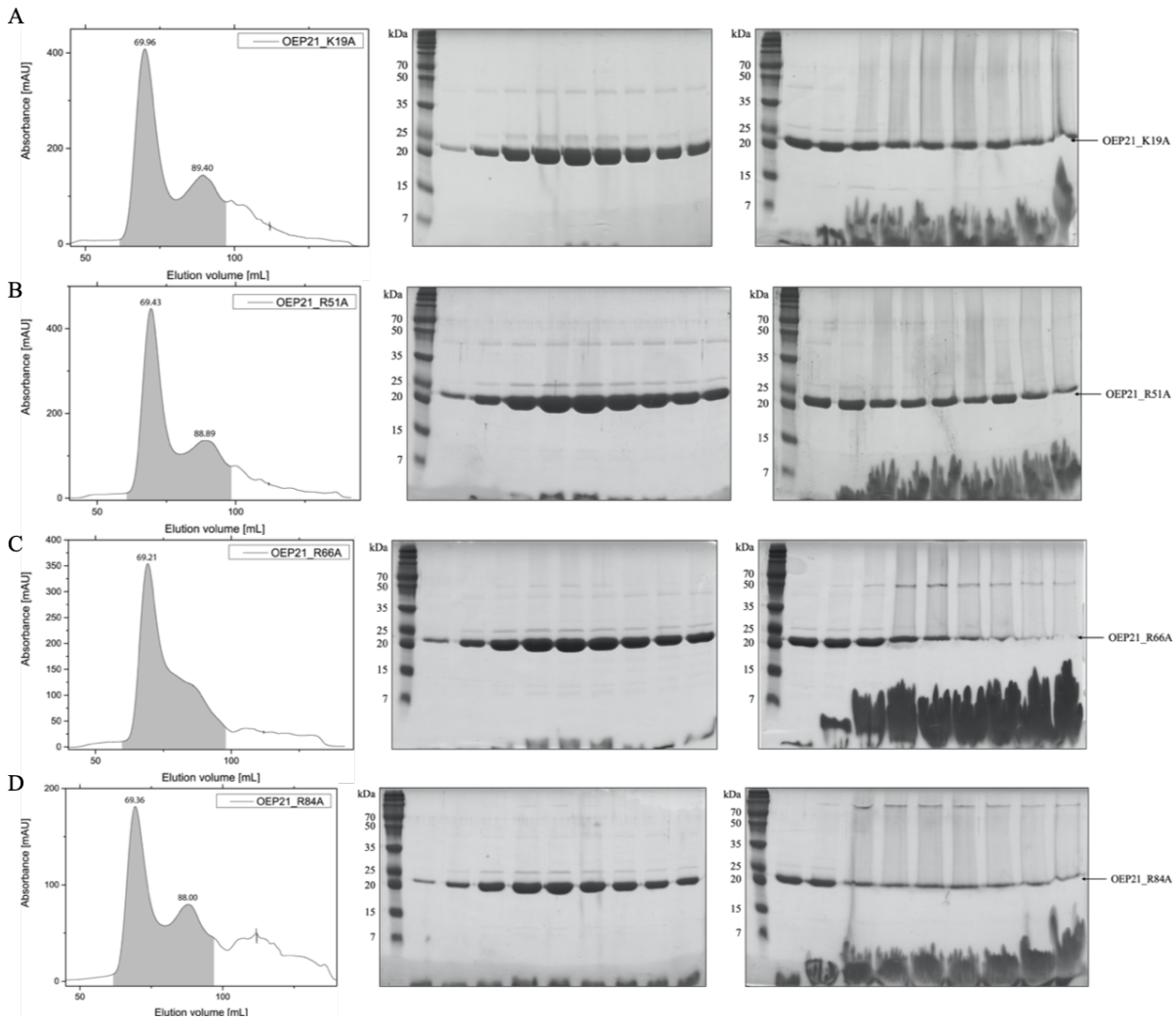

Figure 22: Size exclusion chromatography of OEP21 mutants and their related SDS-PAGE analysis. *Fractions displayed in the SDS-PAGE analysis are highlighted in grey.* ***A*** *OEP21_ K19A* ***B*** *OEP21_ R51A* ***C*** *OEP21_R66A* ***D*** *OEP21_R84A*

The main peak was collected and the associated yield were determined using a NanoPhotometer® N60 (Implen). The yield of OEP21 and the mutants K19A, R51A, R66A and R84A are listed in the following table (**Table 13**). The overall yield varied between 14 and 36 % of the particular protein. Since each purification and refolding might differ, these values are fluctuating but corresponded to this range.

Table 13: Yields of refolded OEP21 and its mutations K19A, R51A, R66A and R84A.

OEP21 mutants	Initial quantity [mg]	Refolding yield [mg]	Yield [%]
OEP21	20	5	25
OEP21_K19A	30	10.64	35
OEP21_R51A	30	10.78	36
OEP21_R66A	30	9.80	33
OEP21_R84A	35	4.76	14

4.1.3. Structural and functional analysis

4.1.3.1. Far-UV CD spectroscopy

Far-UV CD spectroscopic analysis was performed with 10–20 µM protein and additional 0.5 mM metabolite at 20 °C. The spectrum of OEP21 reveals an anti-parallel β-sheet structure in HEPES buffer (**Figure 23, A**). The addition of metabolites does not change the overall secondary structure of the protein. The minimum of each CD-spectra is determined at 214.5 nm. By adding the metabolite, the photomultiplier voltage is increasing above 500 V at wavelength under 210-200 nm, which results in an increasing signal-to-noise ratio. Nevertheless, the signal between 200 and 260 nm can be analyzed. The data imply, that the overall antiparallel β-sheet structure does not change upon ligand. Regarding the determination of the melting temperature T_m by increasing the temperature from 20 to 100 °C the thermal melt plot is displaying a sigmoidal transition indicating the thermal unfolding of OEP21. Additional metabolites do not change the stability of the protein in a significant way, except ATP, which increases the stability from 59.6 °C in the apo state to 64.2 °C in the ATP bound state with an enhanced steepness (Figure 23**, B**).

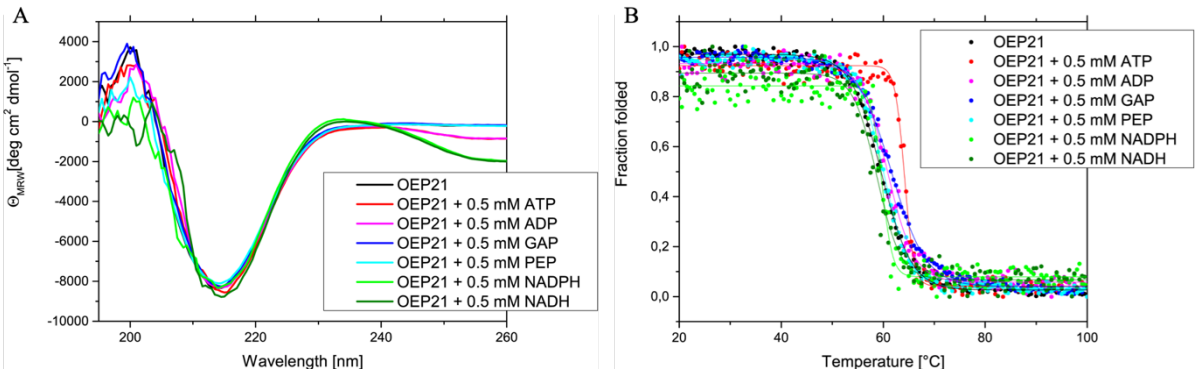

Figure 23: Circular dichroism analysis of OEP21. ***A*** *CD spectra of OEP12-His$_{10}$ (black) and additional 0.5 mM metabolites (colored) showing a typical curve for antiparallel β-sheet membrane proteins detected at 25 °C.* ***B*** *Thermal melting curve of OEP21 (black) and additional 0.5 mM of each metabolite (colored) detected at 214.5 nm.*

Plotting each melting temperature of OEP21 with the metabolites, the effect of ATP on the stability of OEP21 can be highlighted (**Figure 24, A**). Compared to the effect of other metabolites (up to + 2 °C), ATP increases the melting temperature by about 4.6 °C. The stabilizing effect is also independent on the pH of the buffer system (**Figure 24, B**). Here, it has also to be mentioned, that the used buffer system was based on NaP_i. Compared to OEP21 in HEPES pH 6.5, the melting temperature of OEP21 in phosphate buffer is increased of around 2 °C, indicating that phosphate buffers tend to stabilize OEP21 without additional metabolites.

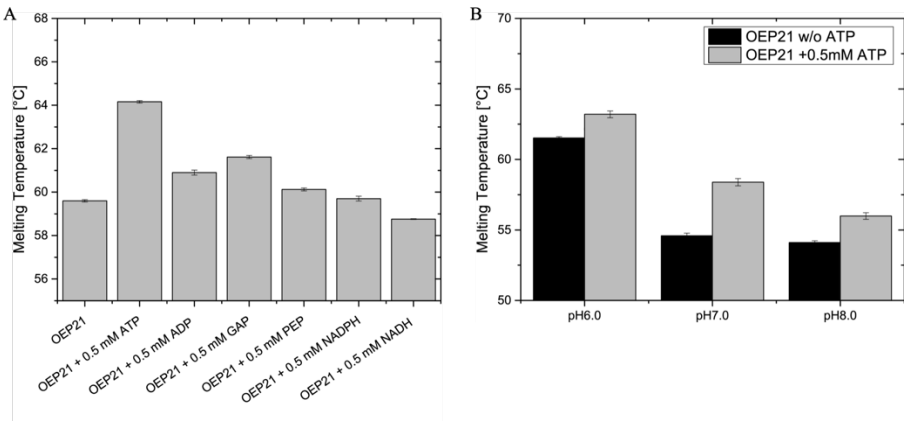

Figure 24: Graphical presentation of the melting temperatures of OEP21. *T_m values of OEP21 in the apo state and in the metabolite bound state were determined using CD spectropolarimeter.* ***A*** *Melting temperature of OEP21 and additional metabolites in a HEPES pH 6.5 buffer system.* ***B*** *Melting temperature of OEP21 dependent on pH and ATP addition determined in a NaP_i buffer system.*

The single point mutations of OEP21 do not change the overall β-sheet structure (Figure 25**, A**). The only difference is the deviation of the amplitude at 214.5 nm, which itself can explained by pipetting errors resulting in small concentration dependent changes in amplitude. Since the highest impact on the stability is caused by ATP addition, the Tm values of OEP21 in an ATP bound state were determined. Thereby an increase in stability of the OEP21 mutants are also present if 0.5 mM ATP is added. (**Figure 25, B**).

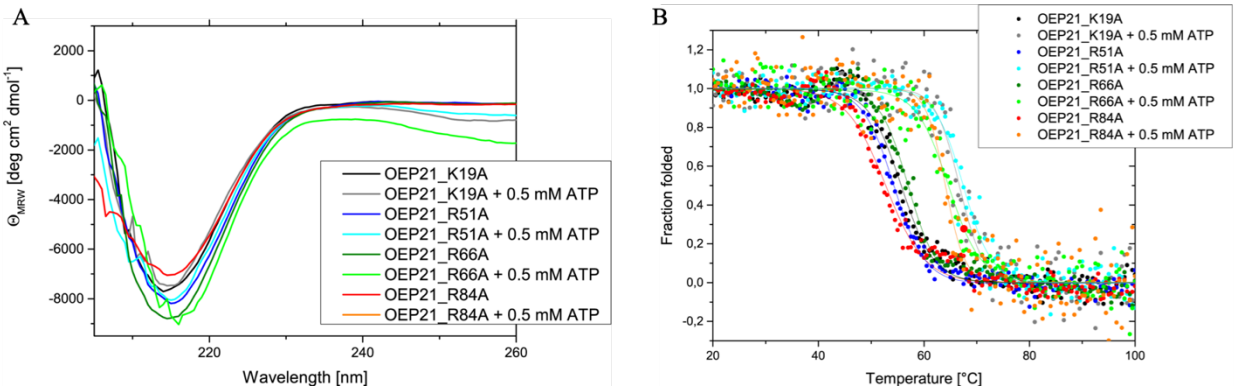

Figure 25: Circular dichroism analysis of OEP21 mutants. ***A*** *CD spectra of OEP12 (black) and its mutations (colored), each ± 0.5 mM ATP showing a typical curve for antiparallel β-sheet membrane proteins detected at 25 °C.* ***B*** *Thermal melting curve of OEP21 (black) and its mutations (colored) detected at 214.5 nm. Adding 0.5 mM ATP the inflection point of the sigmoidal curve shifts to higher temperatures.*

The following figure (**Figure 26**) is depicting the differences of the calculated melting temperatures. Compared to OEP21, the mutants are more instable, but gain stability by adding 0.5 mM ATP. The increased ranges from 4.6 to 13.1 °C and is for OEP21_R51A the highest

increase in stability and for OEP21 the lowest. Adding 0.5 mM ATP, results for all constructs in a final Tm range of 65.4 °C ± 2 °C.

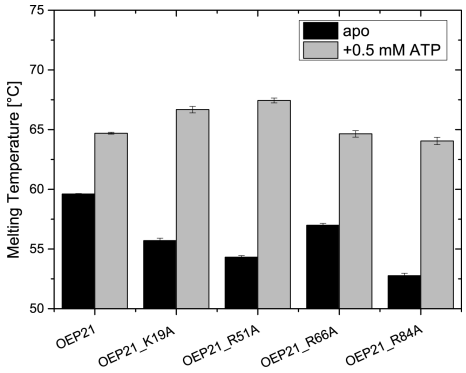

Figure 26: Graphical presentation of the melting temperatures of OEP21 and its mutants. *T_m values of OEP21 and the mutants in the apo state and in the ATP bound state determined using CD spectropolarimeter.*

4.1.3.2. NMR spectroscopic analysis

OEP21 was then structurally analyzed using NMR spectroscopy. Therefore, various OEP21 samples were produced containing various isotope labeling patterns. Deuterated and ^{15}N-labeled OEP21 were used for 2D-[^{1}H,^{15}N]-TROSY experiments, whereas for 3D backbone resonance assignment experiments, ^{2}H,^{13}C,^{15}N-labeled protein was produced. Furthermore, structure determination was performed with a ILVAFY-labeled OEP21, meaning a ^{13}C-labeling of Ala-C_β, Ile-$C_{\delta1}$, Leu-$C_{\delta2}$ and Val-$C_{\gamma2}$ and ^{15}N-labeling of Phe-^{H}N and Tyr-^{H}N. In general protein yields of isotope-labeled OEP21 was around 30 % lower than with unlabeled OEP21, but the obtained amount was still sufficient for recording multidimensional NMR experiments of excellent quality.

Initial [^{1}H,^{15}N]-TROSY spectra were recorded using ^{2}H,^{15}N-labeled OEP21-His_{10}, in order to analyze the folded state of OEP21 and to obtain protein samples of sufficient quality for further NMR analysis (see chapter 3.2.2.1). After successful optimization of refolding conditions of OEP21 in NaP_i buffer containing 5 mM ATP, NMR spectra of excellent quality could be recorded. Using 2D-[^{1}H,^{15}N]-TROSY, 3D-HNCA, HNCO, HNCACB and 3D-^{15}N-edited NOESY spectra, backbone resonances of OEP21 could be assigned to about 85 % (**Figure 27**). The missing non-proline amino acids are located in the dynamic loop regions of the protein (total number of prolines within OEP21 is 4).

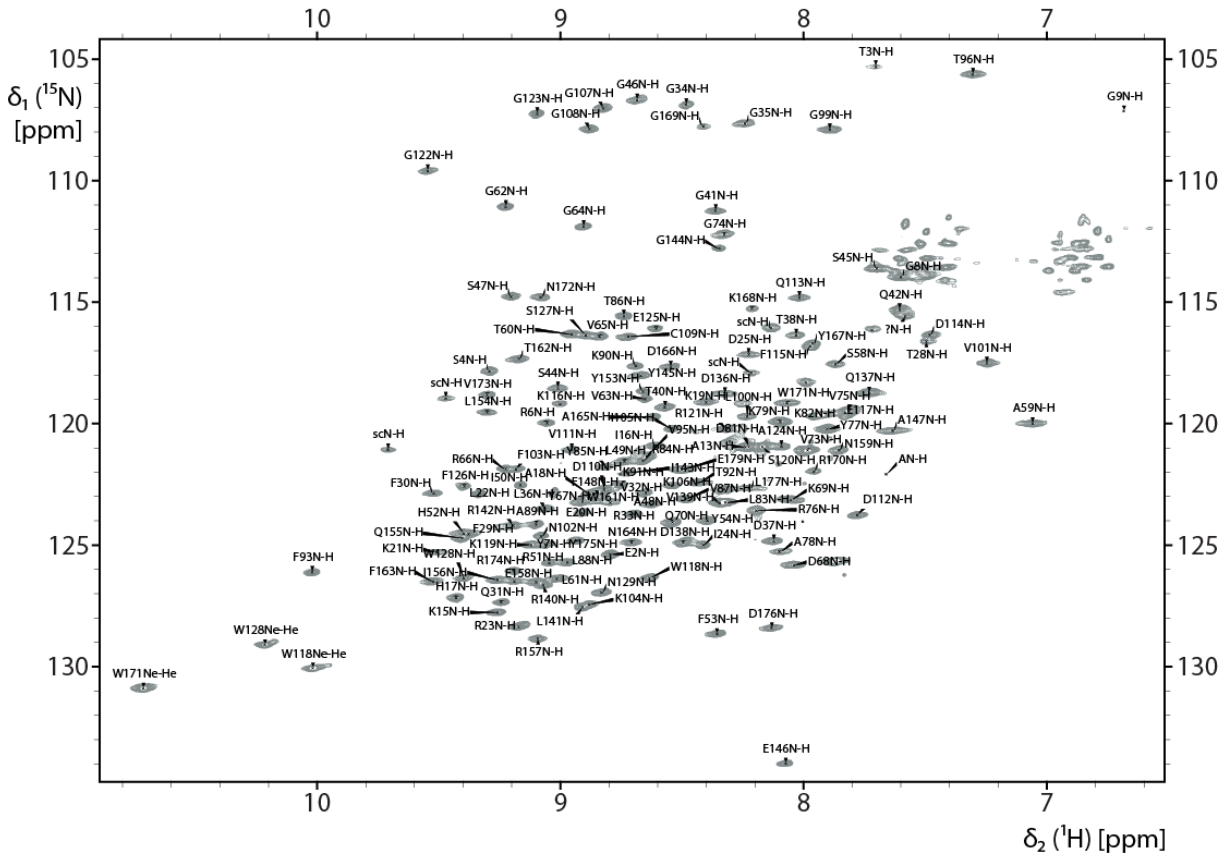

Figure 27: 2D-[1H,15N]-TROSY spectrum of OEP21. *Spektrum were obtained at a 900 MHz Bruker spectrometer with ~85 % assigned amide backbone resonances.*

The differences in the experimental Cα and Cβ carbon chemical shifts *versus* their corresponding random coil values (secondary chemical shifts) was used to obtain a first estimation of the secondary structure elements in the protein (**Figure 28 A)**. This analysis shows that the protein contains12 β-strands. With a closer look on the through-space NOE contacts, the OEP21 topology could be established (**Figure 28**, **B**). This displays an anti-parallel orientation of the β-strands in the barrel. Furthermore, the dimerization side is marked in red, which was extracted from 2D NMR experiments with OEP21 at increasing concentrations of the detergent LDAO. (see also **Figure 31**).

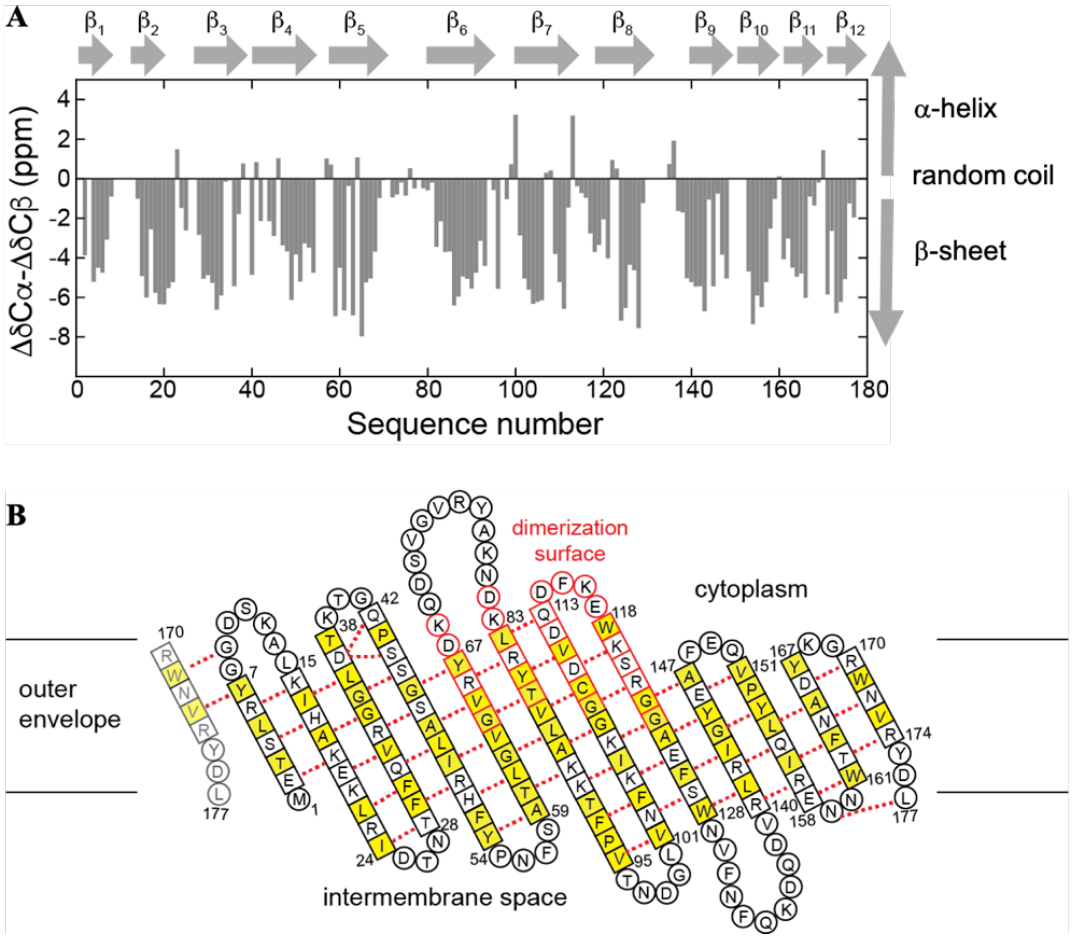

Figure 28: Secondary structure of OEP21 obtained by NMR spectroscopy. ***A*** *Differences between C_α and C_β secondary chemical shift resonances relative to their random coil shifts indicating OEP21 as a 12 β-stranded barrel.* ***B*** *Topology of OEP21 according the through-space NOE contacts, with additional information about the dimerization surface (red).*

For further structure calculation, OEP21 was specifically labeled at position Ala-$^{13}C_\beta$, Ile-$^{13}C_{\delta1}$, Leu-$^{13}C_{\delta2}$ and Val-$^{13}C_{\gamma2}$ and Phe-$^{15}N_H$ and Tyr-$^{15}N_H$ (termed as ILVAFY-OEP21). Expression of OEP21 with the specific labeling was performed according protocol (see chapter 3.2.2.5) and purified (see chapter 3.2.2.1), with a final detergent exchange to deuterated LDAO. The final yield of ILVAFY-labeled OEP21 was ~4.4 mg per liter culture resulting in enough material for two NMR samples of around 450 µM concentration in 300 mM of deuterated d_{31}-LDAO. By recording and analyzing [^{1}H,^{15}N]-TROSY, [^{13}C]-HMQC, [^{15}N]-NOESY-HSQC, [^{13}C]-NOESY-HSQC, NNH-NOESY and CCH-NOESY spectra, structure calculation could be performed with around 700 NOE distance and 300 backbone angular restrains, derived from the program TALOS+ using ^{13}C chemical shift information. Specific data are given in appendix (**Table 19**). **Figure 29 A** depicts the ^{1}H,^{13}C-HMQC with the specific methyl site chains of Ala, Ile, Leu and Val, whereas **B** represents NOE contacts of Ile105 $C_{\delta1}$ and Val173 $C_{\gamma2}$.

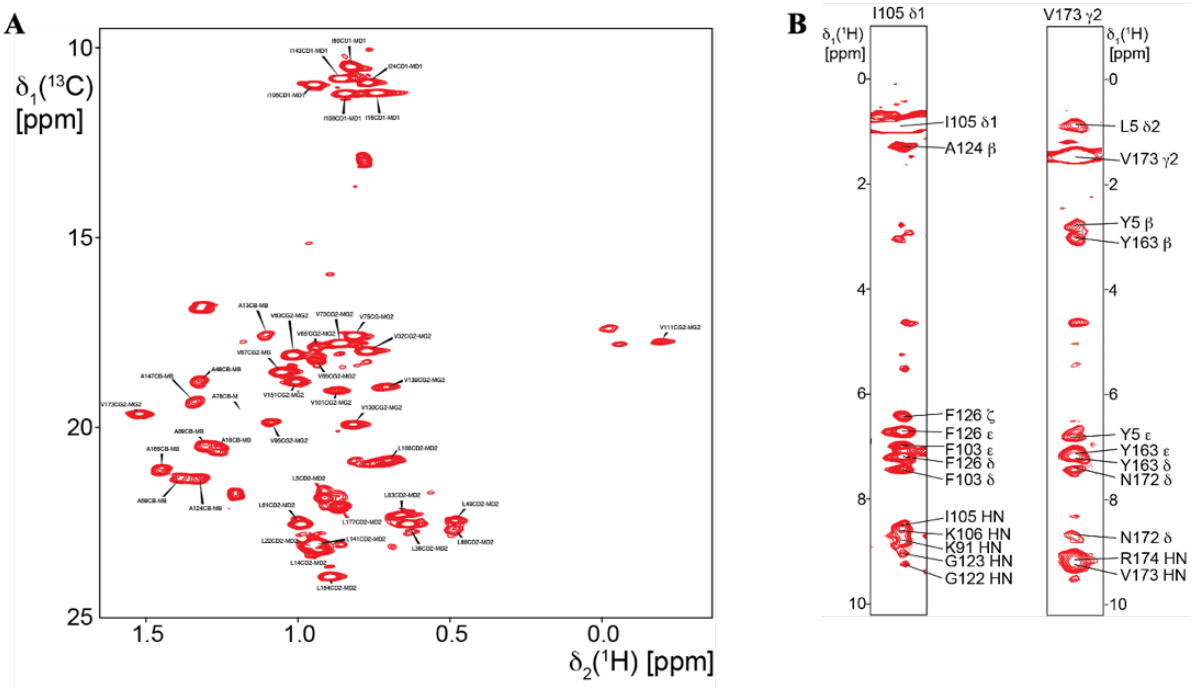

Figure 29: NMR spectroscopic experiments using ILFAFY-labeled OEP21. *A $^{1}H,^{13}C$-HMQC of ILVAFY-labeled OEP21 showing the ^{13}C-labeled methyl sites of Ala, Ile, Leu, Val side chains.* ***B*** *Representative assignment of the NOE contacts of I105 and V173 for structure calculation.*

Using the information obtained from the diverse NMR data sets, the structure of OEP21 was calculated using the obtained NOE restrains. Using Talos+ for the empirical prediction of backbone angles and Procheck for structure validation with the calculated Ramachandran plot, the final structure of OEP21 can be achieved (**Figure 30 B**). OEP21 is a 12 stranded β-barrel pore with a funnel-like shape. By comparing all calculated structures using the obtained NOE restrains, different conformers can be determined. Comparing these conformations of OEP21 the structure bundle depicted in **Figure 30 A** could be created, resulting in an excellent agreement of the obtained structures.

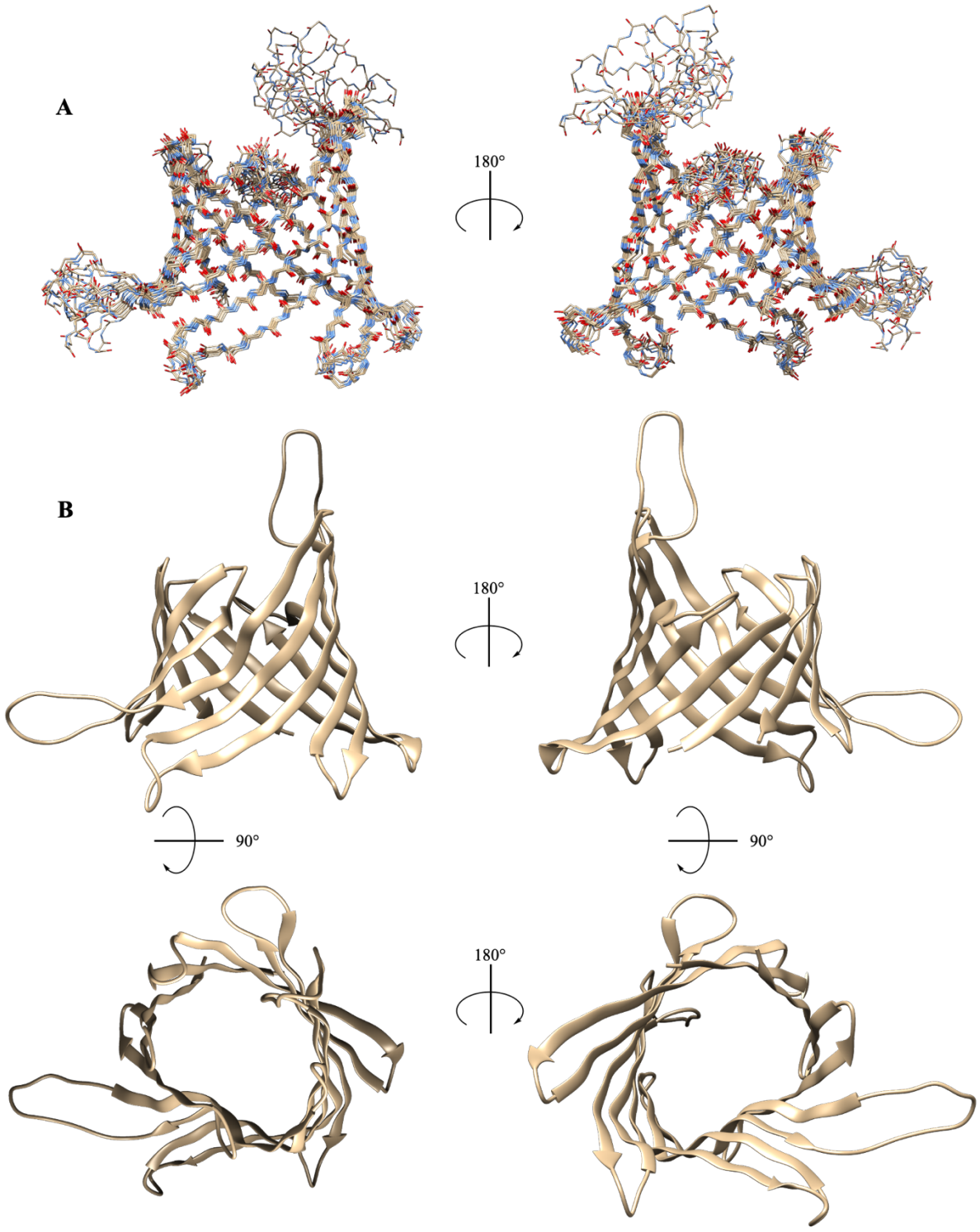

Figure 30: Determined structure of OEP21. A *Structural bundle of OEP21 conformers with a rmsd of 1.9 Å for all backbone atoms and 0.5 Å for ordered secondary structure elements.* ***B*** *OEP21 as a 12 β-stranded barrel in a funnel-like shape, with upper diameter of 18 Å and lower diameter of 34 Å.*

Since structure determination of OEP21 was performed in high LDAO concentrations (~300 mM), a 2D-[^{1}H,^{15}N]-TROSY spectrum was recorded to analyze the effect of increasing detergent concentration. In Figure 31 the spectra of OEP21 in 170 mM LDAO (red) and 500

mM LDAO (grey) are compared. Examining the line width of the signals in the two spectra, a line broadening in the red spectrum can be observed. Additionally, CSP evolves and seven new signals appear in case of the higher LDAO concentration. The corresponding $^{1}H,^{15}N$-CSP plot is shown in **Figure 31 B**. By mapping the chemical shift perturbation on the determined NMR structure, the side of the β-barrel where the long β-sheets are located is mostly affected (Figure 31 **C**), suggesting a potential dimerization site.

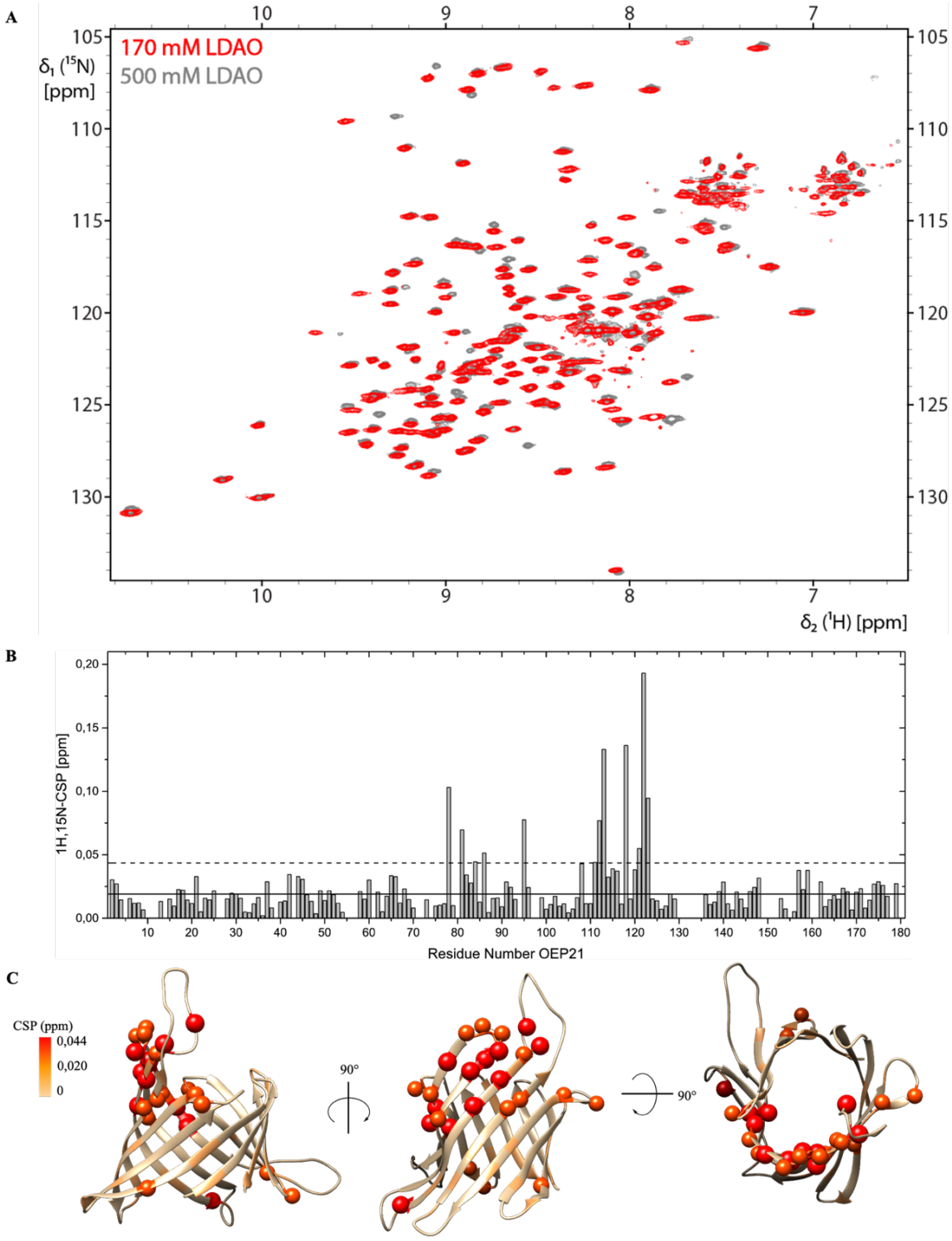

Figure 31: Impact of high and low LDAO concentrations on OEP21. ***A*** *2D-[^{1}H,^{15}N]-TROSY of OEP21 with a final LDAO concentration of 170 mM (red) and 500 mM (grey), respectively.* ***B*** *Corresponding ^{1}H,^{15}N-CSP plot. Mean value is given as a dotted line, whereas the sum of mean value and standard deviation is given in a solid line.* ***C*** *^{1}H,^{15}N-CSP mapped on the calculated OEP21 structure.*

This dimerization site was also verified by PRE studies with OEP21 using the paramagnetic probe 16-DOXYL stearic acid (16-DSA). NMR measurements were performed according chapter 3.3.2 section paramagnetic relaxation enhancement. The presence of 16-DSA

affects amino acids in OEP21, which are not located in the LDAO micelle rather at the surface or outside. The [^{1}H,^{15}N]-TROSY spectrum of OEP21 shows strong signal reduction for a wide range of signals upon the addition of 16-DSA (**Figure 32**, red spectrum), compared to the reference spectrum without 16-DSA (in grey). Adding ascorbic acid, which should lead to reappearance of all peaks, does not change the number of signals nor the intensities. This is most likely caused by inaccessibility of the free radical inside the micelles for the reducing agent. Plotting the relative intensities (**Figure 32**, **B**) and subsequent mapping those on the OEP21 structure (**Figure 32**, **C**), it can be seen that only signals originating from loop regions are still present, confirming the notion that the loops are located outside the micelle. Furthermore, amino acids involved in dimerization still give rise to NMR signals with 16-DSA, however, these are less intense than the ones in loops. This suggests that the dimerization site is shielded from the spin label in the micelle.

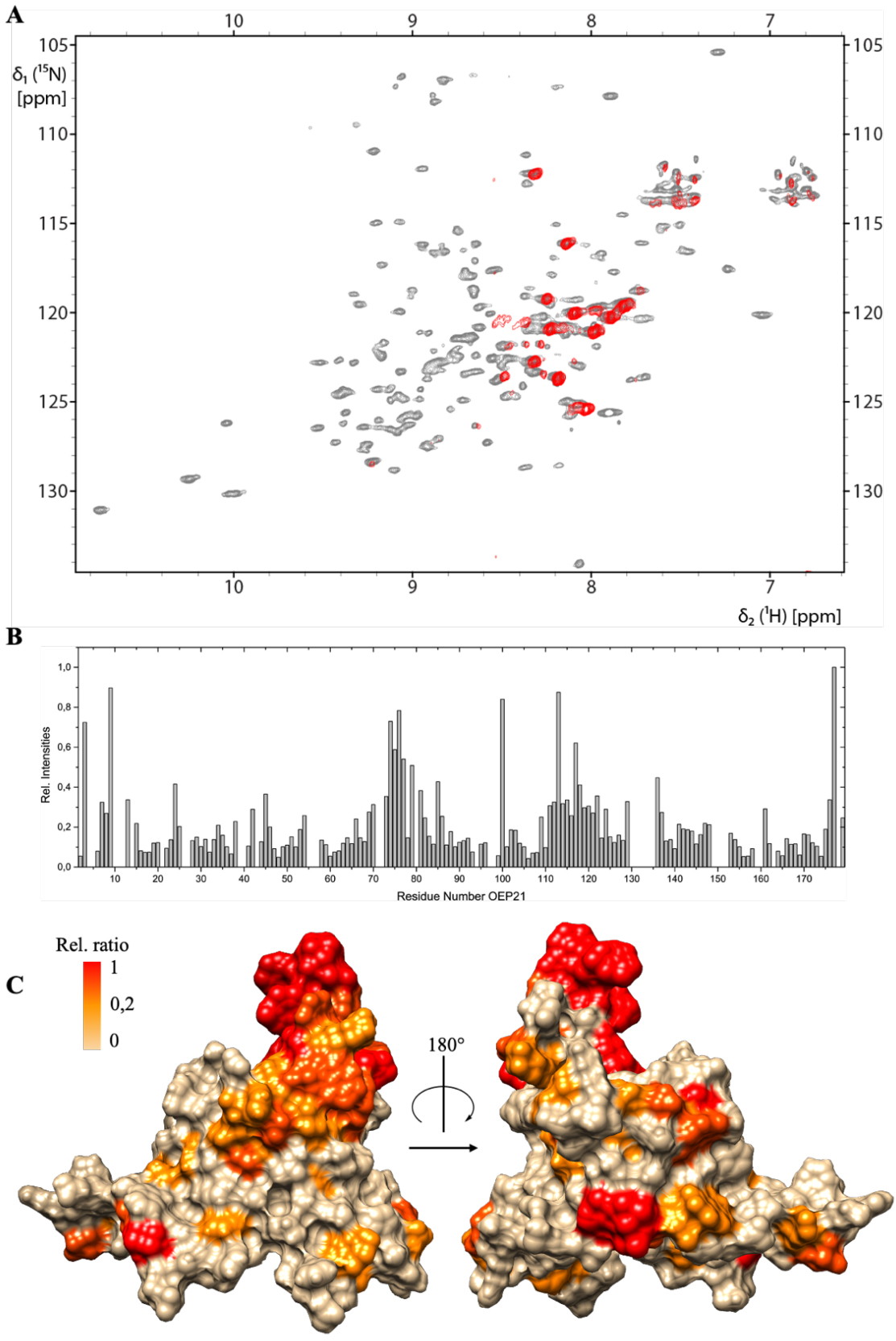

Figure 32: PRE studies with OEP21 using the spin-labeled fatty acid 16-DSA. ***A*** *2D-[^{1}H,^{15}N]-TROSY spectra of OEP21 without (grey) and with 16-DSA (red).* ***B*** *Relative intensity plot of OEP21 +/- 16-DSA.* ***C*** *Relative intensities mapped on the OEP21 structure.*

To analyze the interaction of GAP and ATP with OEP21, NMR titration experiments using 2D-[^{1}H,^{15}N]-TROSY experiments were conducted. A reference spectrum of ^{2}H,^{15}N-OEP21 in HEPES pH 6.5 without ATP was recorded and subsequently 1 mM GAP and 1 mM ATP were added, respectively. The resulting NMR spectra are depicted in **Figure 33 A**, where each spectrum with metabolite (ATP in red and GAP in blue) is overlaid on the reference spectrum (in grey). In both spectra significant changes can be observed compared to the reference spectrum. By adding 1 mM ATP the signals become sharper and marked chemical shift perturbations can be observed. In contrast, additional GAP results in a decrease in signal intensity.

These changes in the spectra result in the ^{1}H,^{15}N-CSPs and relative intensity diagrams as shown in **Figure 33 B** and **C**. ATP induces predominantly CSP and reduces just a bit the signal intensities, whereas GAP mainly affects the intensities and does not induce CSP significantly. By mapping these differences on the structure (**Figure 33 D** and **E**) the changes are predominantly located on the ‘long’ side of the β-barrel, meaning the interaction of ATP and GAP is taking place at this part.

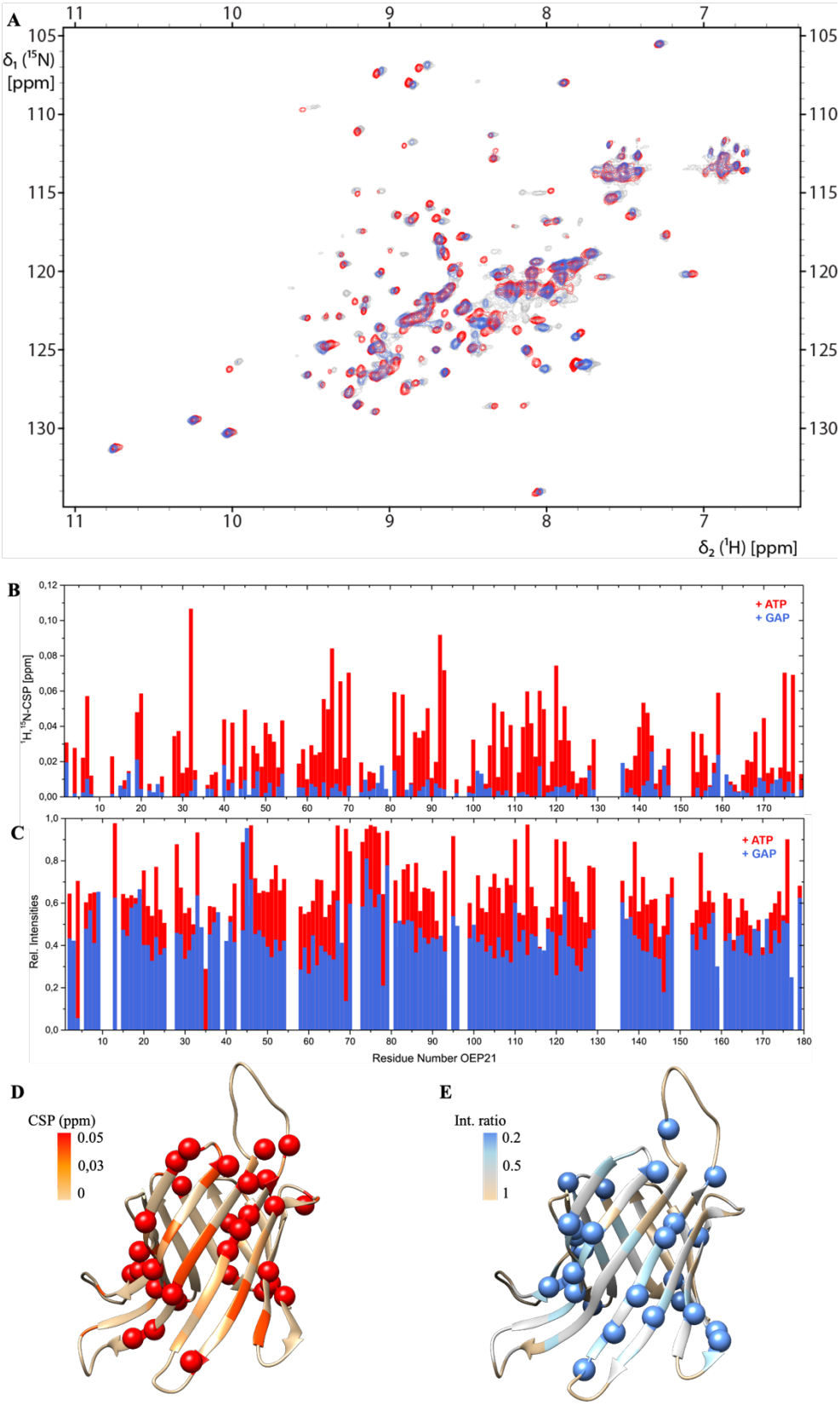

Figure 33: Impact of GAP and ATP on OEP21 analyzed using NMR spectroscopy. *A 2D-[^{1}H,^{15}N]-TROSY spectra of OEP21 in HEPES pH 6.5 (grey) with additional 1 mM ATP (red) and 1 mM GAP (blue).* ***B,C*** *^{1}H,^{15}N-CSP plot and relative intensity plot of OEP21 +/- 1 mM ATP (red) and +/- 1mM GAP (blue), respectively.* ***D,E*** *^{1}H,^{15}N-CSP of ATP addition (red) and rel. intensities of GAP addition (blue) mapped on the structure of OEP21.*

4.1.3.3. Crosslinking via BS^3

Crosslinking of OEP21 is performed according protocol in chapter 3.2.6. **Figure 34** depicts the crosslinking experiments with OEP21 to its dimeric, trimeric and higher oligomeric state with particular focus on the influence of LDAO and different metabolites on the oligomerization pattern. First, LDAO was added stepwise, starting with no additional detergent, meaning a LDAO concentration of 4,4 mM and up to a LDAO concentration of ~500 mM (**Figure 34 A**). Since LDAO disturbs the running behavior of the SDS-samples, TCA precipitation were performed after crosslinking, which results in a significantly decrease of LDAO concentration and a better resolution in SDS-PAGE. Next, 1 mM of distinct metabolites were added to OEP21 (**Figure 34 B**). These metabolites were chosen since they represent the diversity of phosphorylated carbohydrates or are key metabolites, found in plant cells and chloroplasts.

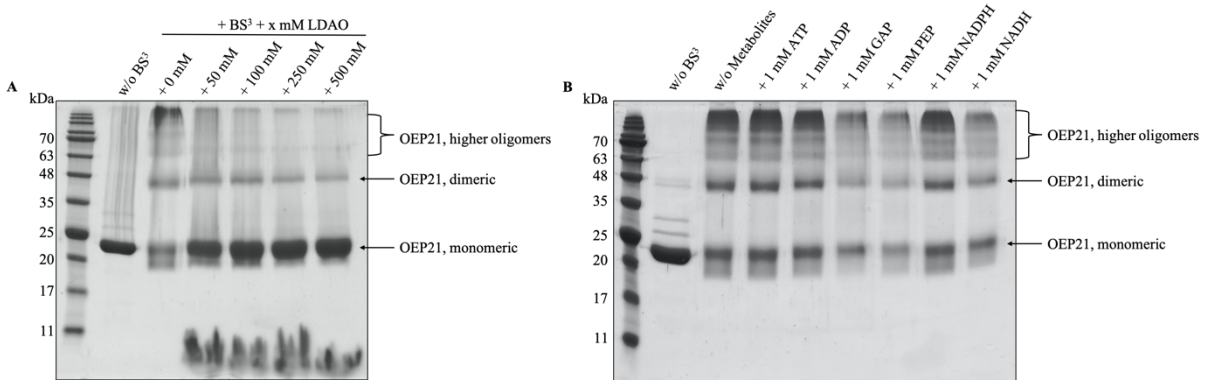

Figure 34:SDS PAGE analysis of the BS3 crosslinking experiments on OEP21. A *SDS-PAGE analysis of OEP21 crosslinking using BS^3 and increasing LDAO concentrations. B SDS-PAGE analysis of OEP21 crosslinking using BS^3 and addition of divers metabolites.*

In **Figure 34 A** the SDS-PAGE analysis of OEP21 with increasing LDAO concentration is illustrated. The reference of OEP21 without crosslinking reagent BS^3 is also given in the first line as a single band at around 23 kDa. By adding BS^3, the SDS gel can display the covalently crosslinked OEP21 oligomers, the dimeric OEP21 at around 46 kDa and higher oligomers as an accumulation starting at around 70 kDa to higher molecular weight. This is especially seen in the case of 0 mM LDAO, meaning a LDAO concentration of 4.4 mM, which corresponds to 0.1 % (w/v) in the protein solution. With increasing LDAO concentration the tendency to form higher oligomers decreases evidently, as best visualized at 500 mM LDAO. Under these conditions, mainly monomeric OEP21 is present with a negligible amount of dimeric conformation. This behavior is in line with the previously shown NMR spectra at 170 mM LDAO and 500 mM LDAO concentration. In comparison, an influence of any metabolite on the oligomeric state of OEP21 cannot be detected in this assay (**Figure 34 B**). Lower intensities

after adding GAP, PEP and NADH can be explained by pipetting errors during loading of the SDS-gel.

4.1.3.4. Liposome assay of OEP21

OEP21 is known to shuttle negatively charge metabolites from the intermembrane space of the chloroplasts to the cytosol. To detect this transport in vitro, a robust assay had to be established. The general methods of the following assays are given in chapter 3.2.7, 3.2.8 and 3.2.9. They were performed using OEP21 and its mutants OEP21_K19A, R51A, R66A and R84A. Hereinafter the different approaches are described with the respective results.

ATP detection assay

This assay should monitor the transport of ATP through OEP21. Therefore, the effect of liposomes, the used metabolites and detergent on the luciferin-luciferase reaction had to be determined. The assay is based on the protocol in chapter 3.2.7. The following figure (**Figure 35**, **A**) shows the recorded luminescence induced by the reaction of ATP and luciferin. The reactions are showing a maximum in luminescence after ~1000 sec for the samples with OEP21 and the mutants respectively. The maximum value of these curves is given in the bar diagram **B** (**Figure 35**) with the corresponding error bars. It can be seen that the mutants show rarely an effect of the mutants on the ATP transport. References of liposomes without OEP21 (given as *Reference Liposomes*) and with additional 0.002 % Triton X-100 result in a flattening curve with no effective maximum. The reference for a 100 % luminescence was determined by adding 1 % Triton X-100 and results in a curve progression with high similarity to the OEP21 results. With the assumption that OEP21, if any, shuttles ATP in a tight fit, the ATP transport should be slower. This should result in a slower increase and therefore later timer point of the maximum. Since this is not the case and the maximum occurs at the same time as the reference, it can be assumed, that OEP21 and its mutants contain too much detergent resulting in the breakup of the liposomes. With the results of the next method this assumption could be verified also after preparation of new protein stocks.

Nevertheless, the effect of GAP on this reaction was tested, to analyze if a competitive assay of ATP and GAP is feasible. Therefore, no liposomes or OEP21 were added to the luciferin-luciferase reaction mixture. **Figure 35 C** depicts the maximum in luminescence with increasing GAP concentrations resulting in a decrease of maximal values. Hence this decrease in luminescence leads to the conclusion that GAP is influencing the luciferin-luciferase reaction

and consequently a competitive assay of GAP and ATP cannot be applied with this approach. Thus, another assay setup is necessary to analyze the competitive transport of ATP and GAP.

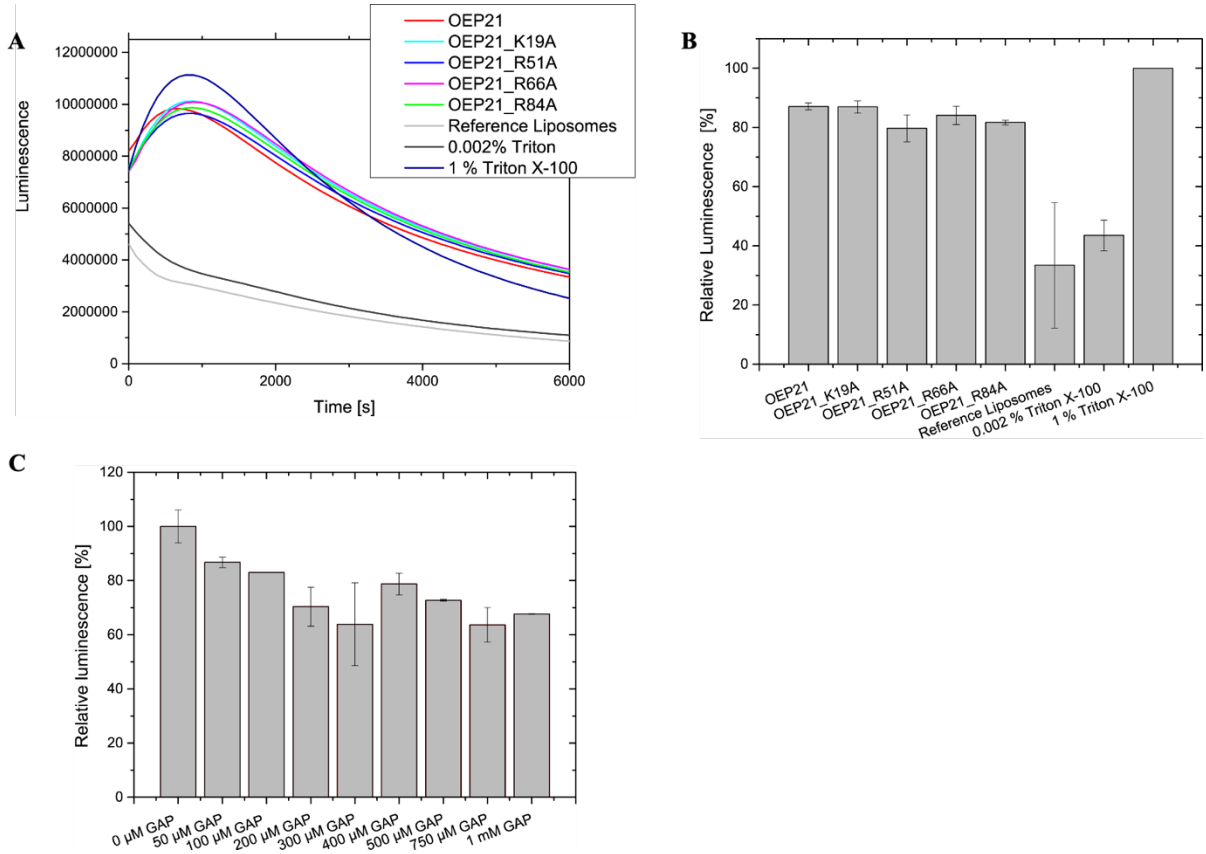

Figure 35: Luciferin-luciferase assay of OEP21. ***A*** *Luminescence curve of OEP21 and its mutants in liposomes* ***B*** *corresponding relative luminescence, whereby 100 % refers to broken liposomes.* ***C*** *depicts the influence of GAP on the luciferase-luciferin reaction.*

Coupled GAPDH-PGK-luciferase assay

Using the enzymes glyceraldehyde 3-phosphate dehydrogenase, phosphoglycerate kinase and luciferase, the coupled GAPDH-PGK-luciferase assay was applied to analyze the transport of GAP through OEP21. This assay was performed to avoid the effect of GAP on the luciferin-luciferase reaction. With this approach GAP is used to produce ATP for further luminescence reaction with luciferin and luciferase. Consequently, the decrease in GAP concentration is caused and thereby it could be assumed that the luciferin-luciferase reaction is not affected by GAP.

The general procedure is described in chapter 3.2.9. By adding OEP21, GAP can be transported from the inside to the outside of the liposomes and starts there the reaction to finally produce ATP further with luciferin. Since GAP reacts further, the luciferin-luciferase reaction should not be affected. The detected luminescence of the GAP transport through OEP21 and its

mutants is shown in **Figure 36 A** and in **B** the maximum of the corresponding curves is presented. The maximal luminescence was determined by adding 1 % Triton X-100 to disrupt the liposomes and to release the total amount of GAP as a suitable reference for the anticipated maximum signal amplitude. Thus, the resulting luminescence was set to 100 %. As in the luciferin-luciferase assay the different mutations do not have a distinct impact on the GAP transport, nor is a delay visible for OEP21 and its mutants. This underlines the previously mentioned liposome leakage issue upon addition of OEP21 in detergent micelles. Additionally, the curve progression of all diverse reactions is similar.

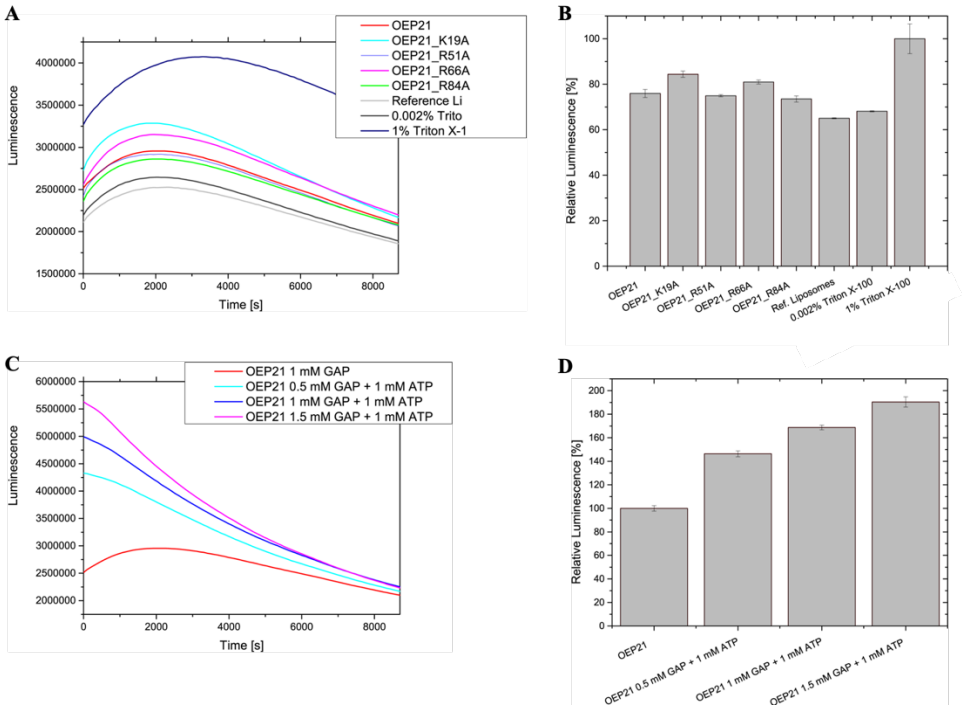

Figure 36: GAPDH-PGK-luciferase assay of OEP21. ***A*** *shows the detected luminescence of OEP21 and its mutant.* ***B*** *representation of the relative luminescence whereby 100 % refers to broken liposomes.* ***C*** *depicts the trial of the competitive ATP-GAP transport assay.* ***D*** *represents the relative luminescence, whereby 100 % refers to the permeability of OEP21 concerning GAP.*

By adding ATP and GAP, the maxima are highly increased. This obvious difference is cause by the reaction of the already present ATP with luciferin. Additionally, with increasing GAP concentrations, more ATP can be produced, which in turn results also in an increase of the luminescence maximum. Consequently, a detection of the competitive transport of ATP and GAP is not possible applying this approach.

Summarizing the results of the luciferin-luciferase and the coupled GAPDH-PGK-luciferase assay, it is obvious that in both approaches the competitive transport of GAP and ATP cannot be analyzed. On the one hand, GAP is interfering the luciferin-luciferase reaction

and on the other hand already present ATP is causing luminescence. Additionally, starting the reaction with addition of OEP21 results in a membrane leakage of liposomes, seen by the same curve progression and same delay of the luminescence maxima. Therefore, the GAPDH assay was performed to prove both, the GAP transport through OEP21 and the influence of the mutants, as well as the hindrance of GAP transport through ATP.

GAPDH assay

Since OEP21 is especially known to transport GAP outside of the chloroplasts, this assay was established to analyze this translocation. The initial approaches, using luciferin-luciferase reaction were not feasible since GAP inhibits this reaction in some parts. Therefore, an assay using GAPDH, which converts NAD to NADH/H^+, using GAP was devised, whereby the absorption of NADH/H^+ at 340 nm could be detected.

The experimental setup was evolved, to diminish the interference of Triton X-100 and LDAO during the assay, which was already observed in the previous assays. Therefore GAPDH, NAD and OEP21 were directly added during liposomes preparation resulting in enclosed GADPH and NAD, while OEP21 is integrated into the bilayer of the liposome. With this setup, the reaction is started by adding GAP instead of the in detergent solubilized membrane protein. Thereby the influence of high detergent concentrations yielding in disruption of the liposomes is diminished. A schematic setup including the two different assays is given in the following figure (**Figure 37**).

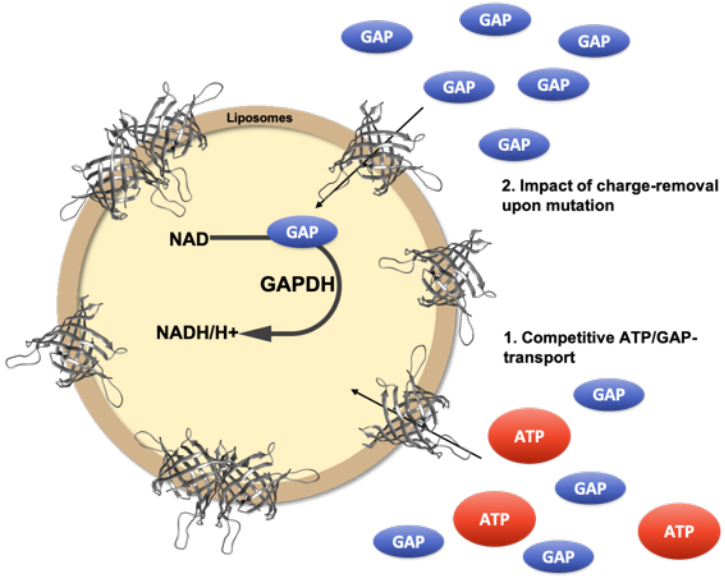

Figure 37: Schematic representation of the experimental setup of the GAPDH assay. *NAD and GAPDH are already enclosed in liposomes and OEP21 is added before the liposome preparation step. First setup is analyzing the efficiency of OEP21 in the GAP transport and the impact of charge-removal upon mutation. The second setup determines the impact of additional ATP.*

Another benefit of this method is the detection of both, the impact of charge-removal inside the barrel by analyzing the transport ability of the corresponding single point variants as well as by the presence of ATP on the transport of GAP. Starting with the influence of ATP on the GAP transport (**Figure 38**, **A** and **C**), a significant decrease in the amplitude is observed, with higher ATP, especially for ratios with ATP to GAP equal or higher 1. Additionally, the maximum is shifted to a later point in time by adding more ATP (**Figure 38 A**, right). In addition, for the reaction without ATP, two peaks can be observed, as well as for the reaction volume with equal amount of ATP. Another observation, which is made, is the overall decrease of absorption at 340 nm by adding higher concentrations of ATP (**Figure 38 A**, left).

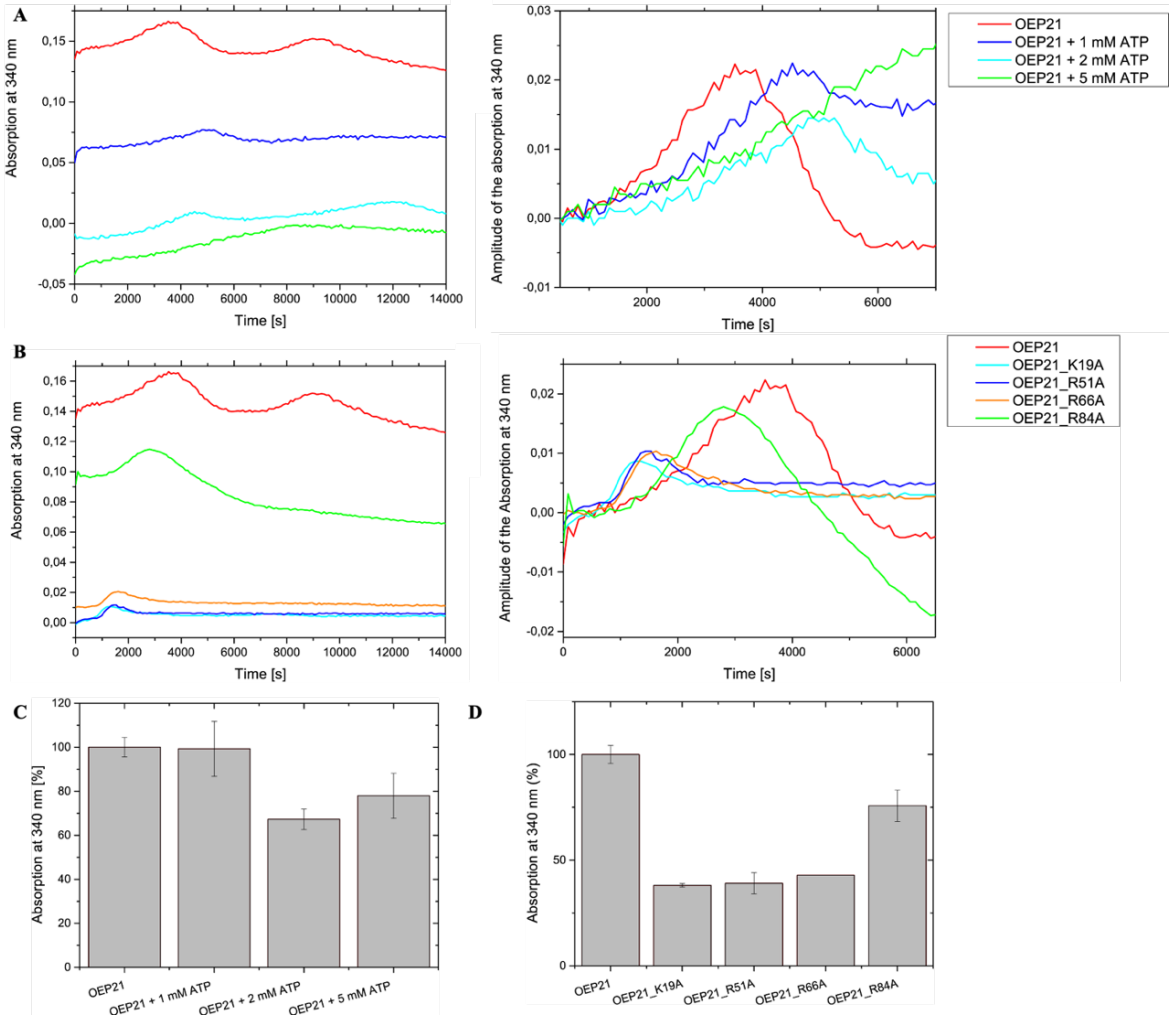

Figure 38: GAPDH assay of OEP21. ***A*** *Absolute absorption of NADH/H⁺ produced by 2 mM GAP transported through OEP21 with 0 mM (red), 1 mM (blue), 2 mM (cyan) and 5 mM (green) ATP added (left) and the resulted relative absorption of NADH/H⁺ produced by 2 mM GAP and additional ATP (right).* ***B*** *Absolute absorption of NADH/H+ produced by 2 mM GAP transported through OEP21 (red), OEP21_K19A (cyan), OEP21_R51A (blue), OEP21_R66A (orange) and OEP21_R84A (green) (left) and the corresponding relative absorption of NADH/H+ produced by 2 mM GAP (left).* ***C*** *Bar diagram showing the impact of ATP on the GAP transport through OEP21, whereby 100 % absorption refers to 2 mM GAP without additional ATP.* ***D*** *Bar diagram of the GAP transport through OEP21 and the different mutants, whereby 100 % absorption refers to OEP21.*

Regarding the mutations of OEP21 a significant decrease of about 60 %, relative to the GAP transport of wt OEP21 is observed for the mutants K19A, R51A and R66A. Whereas the mutation at position 84 affects the transport not as much as the other mutants. (**Figure 38 D**). As for the competitive GAP/ATP assay, the overall absorption is increased in the case where GAP transport was improved (**Figure 38 B**, left). The right data panel of **Figure 38 B** is depicting the amplitude of the absorption at 340 nm. Compared to the wildtype, the mutants show a shift of the maximum to earlier time points with a significant decrease in amplitude.

Conclusively the different assays, to detect the transport of ATP or GAP, first point out that the addition of OEP21 in detergent micelles to start the reaction is not applicable. This is due to the breakup of the liposomes following the addition of the protein. Second the GAP hinders the luciferin-luciferase reaction. Thereby this approach is not practicable. Third using GAPDH and NAD the absorption at 340 nm, is sufficient to detect the transport, given that OEP21 is already added during liposome preparation.

4.2. wtOEP21

4.2.1. Expression and purification

wtOEP21, meaning OEP21 without His-tag, is expressed, purified and refolded according protocol in chapter 3.2.2.2. The SDS-PAGE analysis of the expression at 37 °C for 5 h is shown in **Figure 39 A,** indicating a successful production of wtOEP21 by the emerging band after 5 h at 20 kDa. **Figure 39 B** shows the SDS-PAGE analysis of the purification steps via SP Sepharose. The obvious band of wtOEP21 in the FT fraction indicates an overload of the used resin. To increase the yield the FT fraction was purified again using a SP Sepharose gravity flow chromatography. The elution fraction in contrast shows primarily wtOEP21, but also some impurities. These impurities could be removed for the most part in the following purification steps. After the dialysis of the elution fraction and dissolving the precipitated protein in a 6 M GdmCl buffer a yield of 16 mg per 1 L main culture could be calculated, which is 46 % less compared to OEP21 with additional His-tag.

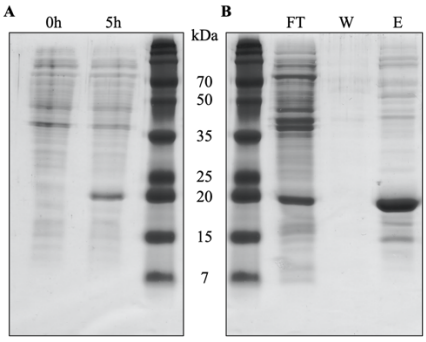

Figure 39: SDS-PAGE analysis of wtOEP21 production. ***A*** *Expression of wtOEP21 at 37 °C for 5 h with a positive wtOEP21 band at 20 kDa.* ***B*** *SDS-PAGE analysis of the purification of wtOEP21 using SP Sepharose gravity flow chromatography.*

After refolding a size exclusion chromatography using a Superdex 200 pg column was performed. The associated SEC profile is given in the next figure (**Figure 40**) with a predominate peak at 68.72 mL elution volume, which correlates with a size of ~190 kDa. The concentration of the main peak is yielding in 2.1 mg of refolded wtOEP21 in LDAO, which corresponds to 13 % of the initial concentration. Compared to OEP21-His_{10} the refolding efficiency is halved.

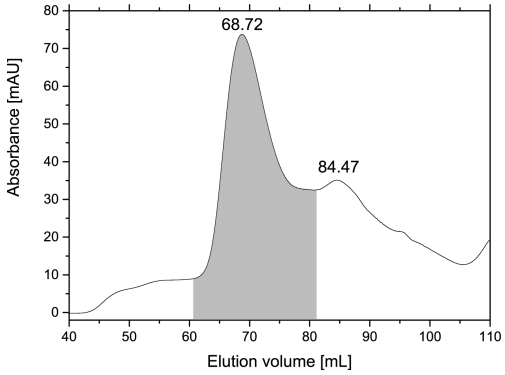

Figure 40: Size exclusion chromatogram of wtOEP21. *Main peak at 68.72 ml elution volume colored in gray were collected and concentrated.*

4.2.2. Functional and structural analysis

4.2.2.1. CD spectroscopy

Circular dichroism spectroscopy was performed to analyze the secondary structure of wtOEP21 and the influence of ATP on its structure and stability (**Figure 41**).

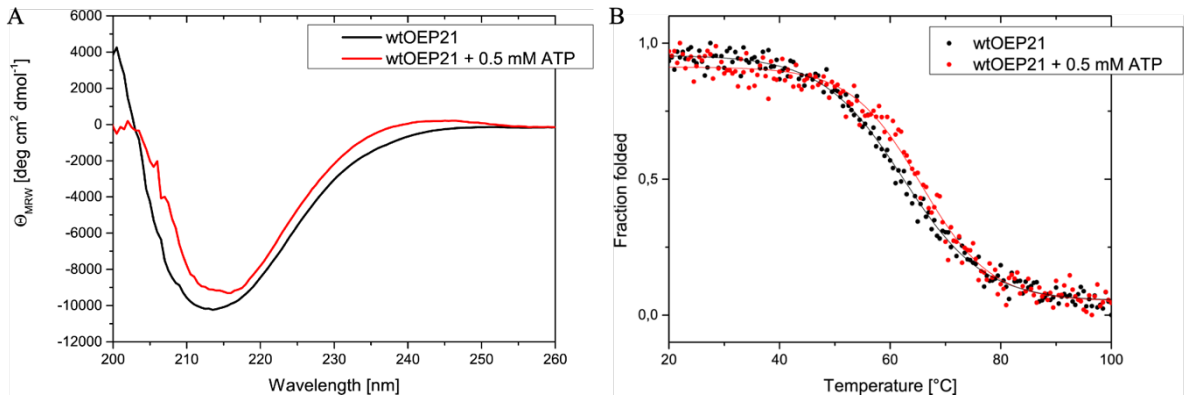

Figure 41: Circular dichroism analysis of wtOEP21. ***A*** *CD spectroscopy of wtOEP21 (black) and wtOEP21 with additional 0.5 mM ATP (red).* ***B*** *Thermal melting curve of wtOEP21(black) and wtOEP21 with additional 0.5 mM ATP (red).*

Comparing the two CD spectra of wtOEP21 +/- ATP (**Figure 41**, **A**) no marked difference can be detected, beside a minor shift of the minimum to higher wavelength. Additionally, a decrease of the minimum is observed. Signal-to-noise is also increasing at lower wavelength for wtOEP21 + ATP, since the ATP is increasing the photomultiplier voltage of the CD detector to above 500 V. Consequently, it appears that the overall secondary structure of wtOEP21 is not changing with the addition of ATP. Regarding the stability of wtOEP21, the temperature dependent diagram indicated a slight effect of ATP. Therefore, the melting temperatures were plotted in the next diagram (**Figure 42**). Compared to the construct containing a C-terminal His_{10}-tag, wtOEP21 is more stable without adding ATP. But as seen before the addition of ATP increases the stability by ~3 °C, which strongly suggests a stabilizing effect of ATP also on wtOEP21.

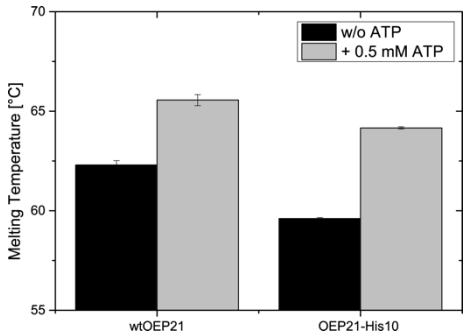

Figure 42: Comparison of the melting temperatures of wtOEP21 and OEP21. *In each case the apo state is contrasted with the ATP bound state using 0.5 mM ATP.*

4.2.2.2. NMR spectroscopy

To analyze the impact of the His-tag at the C-terminus of OEP21 on the overall structure, NMR measurements were performed. Therefore ^{2}H-^{15}N-labeled wtOEP21 was expressed and purified

according the protocol. Slight changes in the refolding conditions had to be made, since the first attempt using a HEPES buffer system without ATP was not successful. The following buffer were finally used for refolding: 20 mM HEPES pH 6.5, 50 mM NaCl, 1 mM EDTA, 3 mM DTT, 10 % (v/v) Glycerol, 2 mM ATP and 1 % (m/v) LDAO. wtOEP21 was measured in a buffer system containing 20 mM HEPES pH 6.5, 50 mM NaCl, 0.5 mM EDTA, 5 mM DTT, 2 mM ATP and 0.1 % (m/v) LDAO. The following overlay is illustrating the comparison of the NMR spectra of OEP21-His_{10} (grey) and wtOEP21 (red). A general low field shift is observable for wtOEP21. The appearance of NMR resonances in the area at around 8 ppm in the proton dimension and between 118–125 ppm in the nitrogen dimension can be traced back to impurities in the sample, since wtOEP21 cannot be produced in a high purity compared to OEP21-His_{10}.

To analyze the peak shift in more detail, a chemical shift perturbation plot (CSP) and the corresponding structural mapping of these effects were compiled (**Figure 43**, **B**). The CSP plot illustrates an overall change in the structure. Mapping those on the structure of OEP21-His_{10} chemical shift perturbation effects can be seen in the entire protein. This general shift of all signals might be temperature dependent, since both spectra were recorded at 303K or 308K respectively. Thus, it can be concluded that the structure of OEP21 is not influenced by the presence of a C-terminal His_6-tag.

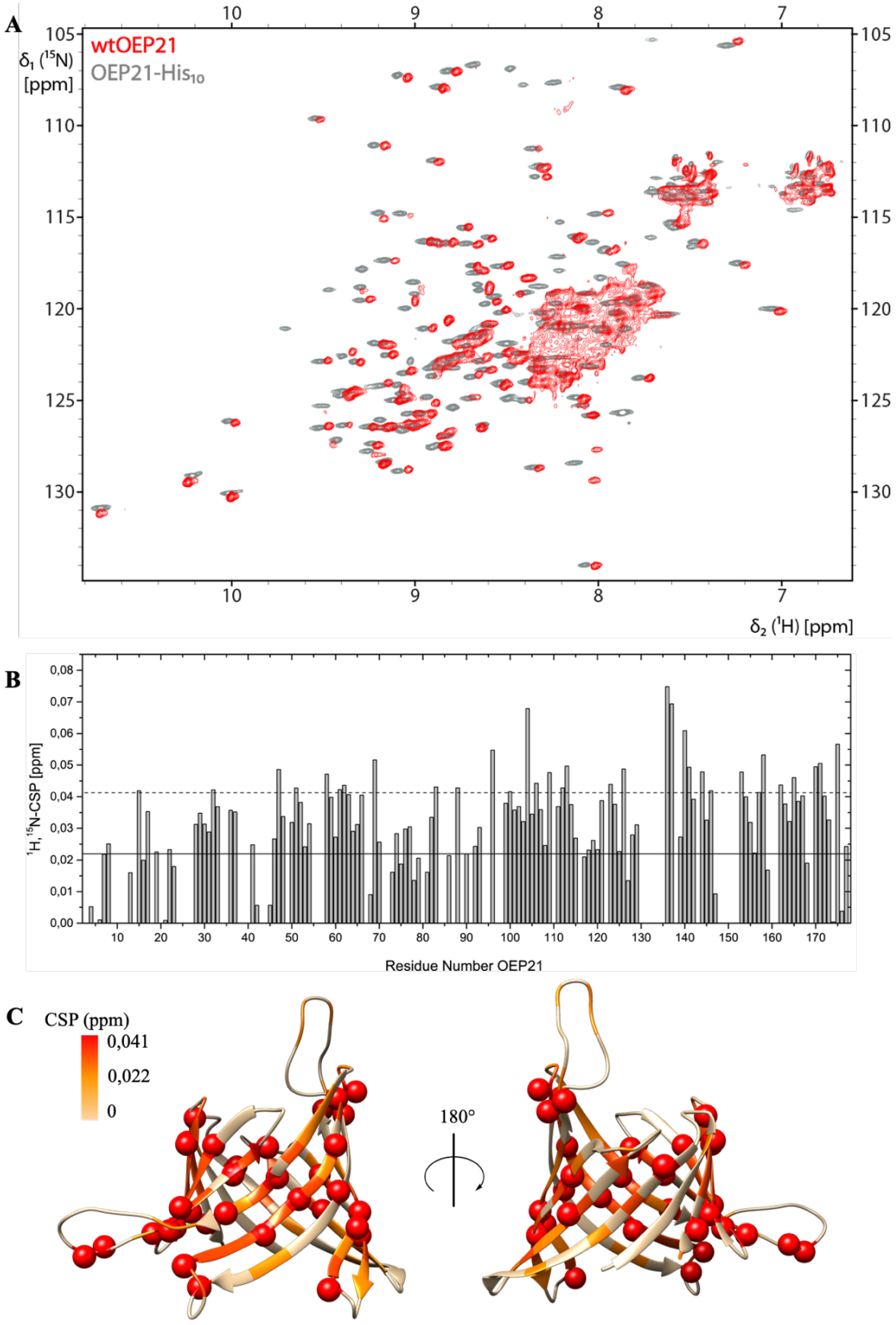

Figure 43: Comparison of wtOEP21 and OEP21-His$_{10}$ using NMR spectroscopy. ***A*** *2D-[^{1}H,^{15}N]-TROSY spectra of wtOEP21 (red) compared to OEP21-His$_{10}$ (grey).* ***B*** *^{1}H,^{15}N-CSP plot of wtOEP21 and OEP21-His$_{10}$. The mean value is given as a dotted line, whereas the sum of mean value and standard deviation is given in a solid line.* ***C*** *CSP values mapped on the OEP21 structure. No changes or not assigned amino acids are given in beige and the higher the changes the more intense the red.*

4.3. hVDAC1

The following results are partially published in **Häusler et al., Quantifying the insertion of membrane proteins into lipid bilayer nanodiscs using a fusion protein strategy, BBA – Biomembranes 1862 (2020) 183190. [95]**

4.3.1. hVDAC1 – Expression, purification and nanodisc assembly

Successful expression of hVDAC1 was performed as described in chapter 3.2.2.3. After purification of 1 L main culture, Ni affinity chromatography, precipitation and resolving in 6 M GdmCl a yield of around 50 mg hVDAC1 was achieved. **Figure 44 A** and **B** show the SDS-PAGE analysis of the hVDAC1 expression after 5 h at 37 °C and of the Ni affinity gravity flow chromatography. hVDAC1 expressed in a high level. Using 4 mL NiNTA resin the flow through fraction contained still a high amount of hVDAC1. A repetition of the Ni affinity chromatography was performed using the FT fraction to improve the yield. The wash fraction was as clean as the elution fraction. Hence it could be precipitate together and dissolved in 6 M GdmCl buffer to a final concentration of 5 mg/mL yielded in around 10 mL protein solution. In total a yield of ~50 mg hVDAC1 in GdmCl buffer was achieved by purification of 1 L main culture.

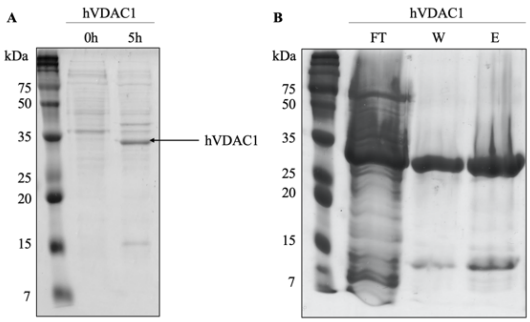

Figure 44: SDS-PAGE anaylsis of hVDAC1 production. ***A*** *Expression of hVDAC1 using E. coli BL21 (DE3) competent cells.* ***B*** *Ni affinity chromatography of hVDAC1 in 6 M GdmCl showing flowthrough (FT), wash (W) and elution (E).*

Refolding of 13 mL of hVADC1 in 130 mL refolding buffer (see chapter 3.2.2.3) was resulting in three cation exchange chromatography runs. Figure 45 shows the chromatogram of the separation of correctly and incorrectly folded hVDAC1. Correctly folded hVDAC1 was eluted at a salt concentration of ~300 mM. Following fractions were combined and concentrated. The concentration of hVDAC1 was determined to ~20 mg, respective to an amount of 65 mg starting quantity. A final yield of ~31 % of correctly folded hVDAC1 in LDAO micelles could be achieved.

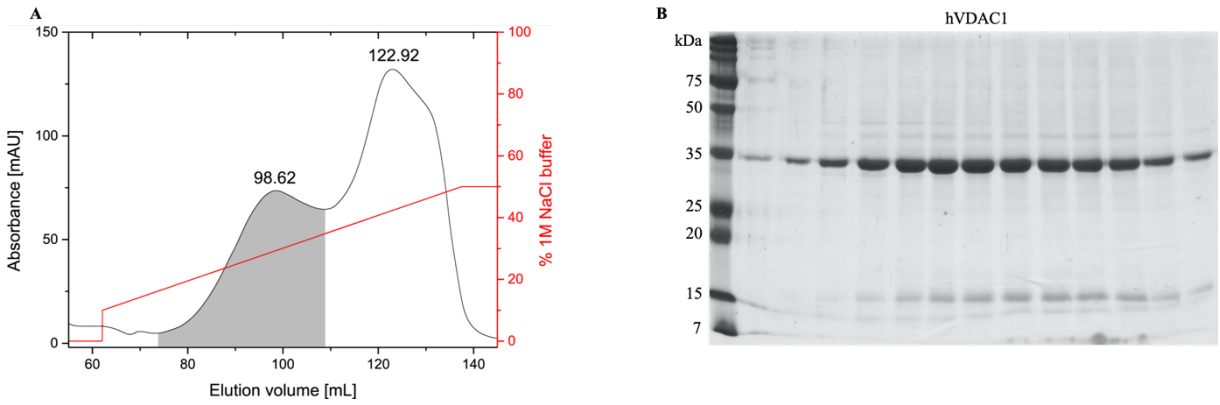

Figure 45: Separation strategy of correctly folded hVDAC1. ***A*** *Cation exchange chromatography (HiTrap SP Sepharose FF) of hVDAC1 refolded in 1 % LDAO buffer. Correctly folded hVDAC1 elutes at 200–400 mM NaCl.* ***B*** *SDS gel of the main fraction of the cation exchange chromatography column (marked in gray) showing nearly pure hVDAC1 at around 35 kDa.*

The refolded hVDAC1 in LDAO was then used to assemble nanodiscs. The purification of the used MSP variants (MSP1D1 and MSP1D1ΔH5) are not shown. The assembly was performed described as in chapter 3.2.3, using a hVDAC1 to MSP ratio of 1:6. The following figure (**Figure 46**) shows the SEC profiles of the assembled hVDAC1 nanodiscs, using MSP1D1 and MSP1D1ΔH5, as well as its associated SDS-PAGE analysis. The elution volume of the MSP1D1 nanodisc of hVDAC1 is slightly lower than for MSP1D1ΔH5, since it is bigger in size. The calculated molecular weight of the different nanodiscs, using these elution volumes, is 123.87 kDa and 134.83 kDa, respectively for 13.70 mL and 12.88 mL (applied equation given in appendix chapter III). Considering the mass of hVDAC1 and twice the mass of MSP without the lipids the molecular weight is ~69,8 kDa for MSP1D1ΔH5 and ~74,9 kDa for MSP1D1. Accordingly, the amount of lipids is 54 kDa and 60 kDa, respectively for MSP1D1ΔH5 and MSP1D1. Comparing the bands of hVDAC1 and MSP on the SDS gel the upper band is not as intense as the MSP band. This is valid for both nanodisc sizes and can be explained, since a nanodisc consist of two MSP proteins and mainly one hVDAC1 protein as also proven later on.

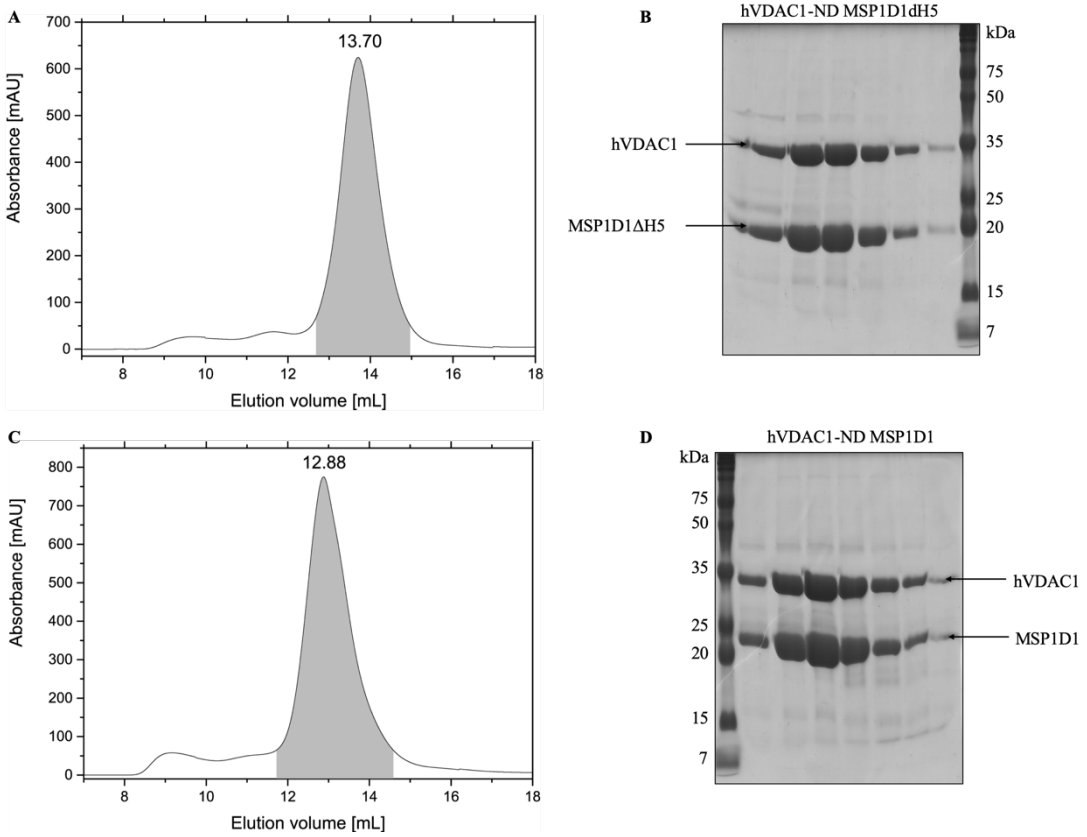

Figure 46: Size exclusion chromatography of hVDAC1 in nanodiscs. ***A*** *MSP1D1ΔH5 nanodiscs with* ***B*** *corresponding SDS-PAGE analysis* ***C*** *MSP1D1 nanodiscs with* ***D*** *corresponding SDS-PAGE analysis.*

Far-UV CD spectroscopic analysis of hVDAC1 in LDAO micelles reveals mainly β-sheet structure, whereas in MSP-nanodiscs the α-helical structure of MSP influences the overall data shape. When comparing the melting temperatures T_m of hVDAC1 in LDAO and MSP-nanodiscs the stability increases from detergent (57.9 °C) to small nanodiscs (67.5 °C) and further to large nanodiscs (71.6 °C). The melting curves of hVDAC1 in MSP-nanodiscs (**Figure 47 C**, blue and red curve) depicts a second transition at high temperature (~95 °C), indicating the melting temperature of the MSP.

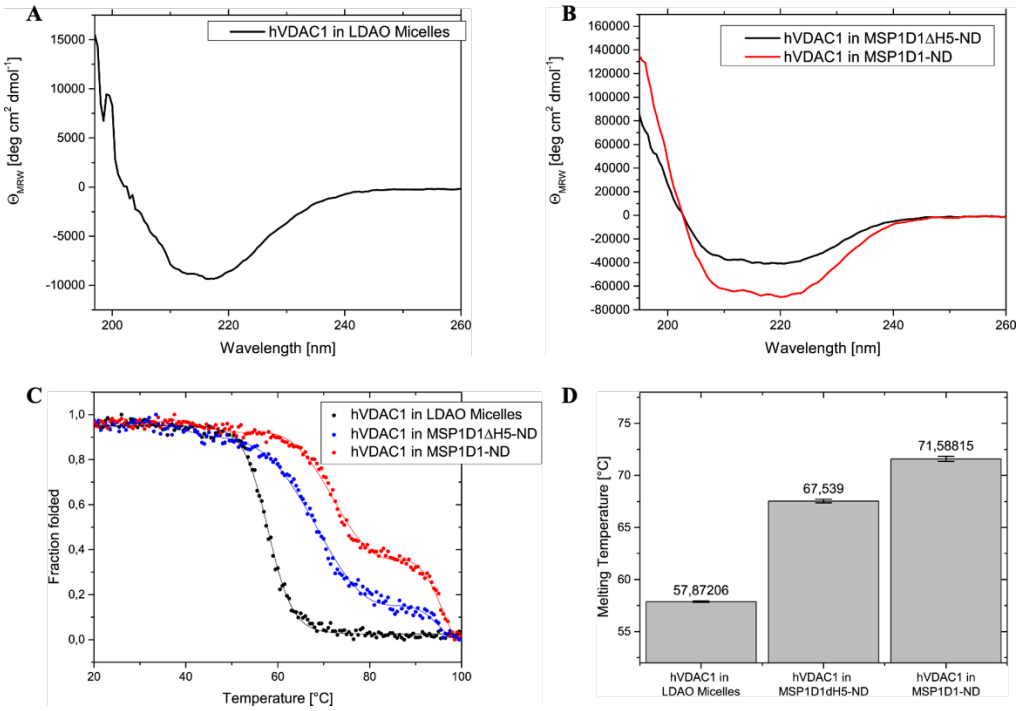

Figure 47: Circular dichroism spectroscopy of hVDAC1 in LDAO, MSP1D1ΔH5- and MSP1D1-nanodiscs. *A CD spectrum of hVDAC1 in LDAO micelles.* ***B*** *CD spectra of hVDAC1 in MSP1D1- (red) and MSP1D1ΔH5-nanodiscs (black).* ***C*** *Thermal melting curve of hVDAC1 in LDAO micelles (black), MSP1D1ΔH5- (blue) and MSP1D1-nanodiscs (red).* ***D*** *Determined melting temperatures of hVDAC1 in different mimetics.*

4.3.2. GB1-hVDAC1 – Protein production and purification

To evaluate the quantity of hVDAC1 in nanodiscs (MSP1D1 and MSP1D1ΔH5) different constructs were additionally produced and purified. These includes the following constructs, His_6-GB1-Thr-hVDAC1 (abbreviated GB1-hVDAC1) and His_6-TEV-GB1-Thr-MSP1D1ΔH5 (GB1-MSP1D1ΔH5). The expression of GB1-hVDAC1 yielded in around 150 mg per 1 L main culture inclusion bodies, solved in 6 M GdmCl buffer with a concentration of 5 mg/mL. After refolding, the cation exchange chromatography (**Figure 48**) separated the correctly folded from the incorrectly folded GB1-hVDAC1. Correctly folded GB1-hVDAC1 eluted at 20–40 % of 1 M sodium chloride buffer resulting in a distinct peak. Combining these fractions, a yield of ~50 mg refolded hVDAC1 was achieved, meaning a total yield of ~80 % for correctly refolded GB1-hVDAC in LDAO micelles. The SDS-PAGE analysis confirmed the purity of GB1-hVDAC1. Compared to hVDAC1, the overall expression, purification and refolding yields in three times more protein solubilized in 6 M GdmCl buffer. Additionally, refolding efficiency is more than 2.5 times higher.

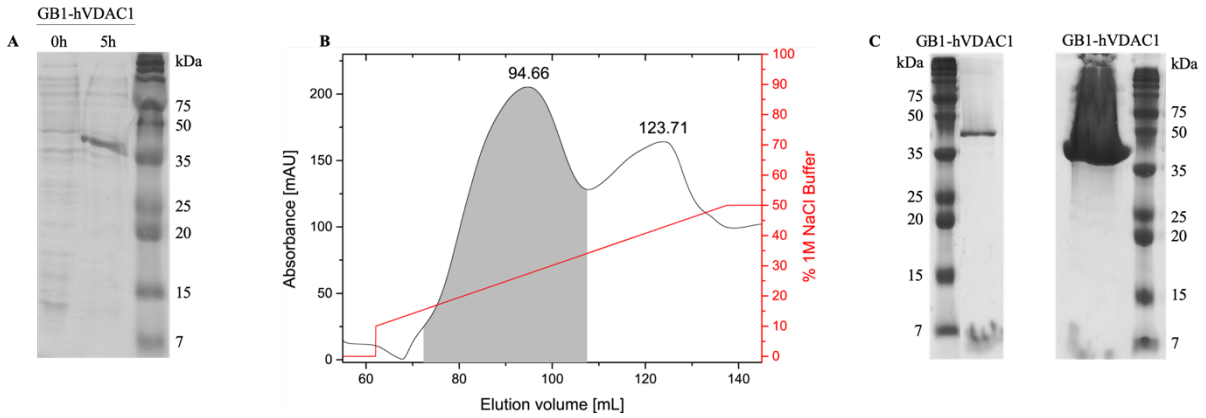

Figure 48: Separation strategy of correctly folded GB1-hVDAC1. ***A*** *Cation exchange chromatography of GB1-hVDAC1 refolded in 1 % LDAO.* ***B*** *SDS-PAGE analysis of the combined main peak (not concentrated (left) and concentrated (right)).*

4.3.3. Evaluation of the quantity of hVDAC1 in MSP nanodiscs

Two different approaches were performed to evaluate the quantity of hVDAC1 in nanodiscs. First, the GB1 was fused to hVDAC1, whereas in the second approach a GB1-MSP fusion construct was used. The expression, purification and refolding of GB1-hVDAC1 was already discussed previously, whereas the purification of the GB1-MSP1D1ΔH5 construct is described below.

To determine the impact of different GB1-hVDAC1 to MSP ratios during assembly, five different conditions for MSP1D1ΔH5 and MSP1D1 were tested. Therefore, the GB1-hVDAC1 to MSP ratios were varied, starting with a ratio of 1:1, then 1:2, 1:4, 1:6 up to 1:8. The nanodiscs of GB1-hVDAC1 were assembled according the protocol described in chapter 3.2.3. Figure 49 depict the procedure of nanodiscs purification and cleavage of GB1. The applied hVDAC1 to MSP1D1 ratio during assembly is 1:1 and is representative for all assembly ratios of hVDAC1 to both MSP variants.

A and **B** show the size exclusion chromatogram of GB1-hVDAC1 nanodiscs and the corresponding SDS-gels. The SEC profile reveals a single peak at 12.52 mL related to GB1-hVDAC1 nanodiscs and some aggregation at less elution volume. After collecting the main peak of the SEC run (colored in grey), thrombin was added to cleave of the GB1. The thrombin cleavage was analyzed, using SDS-PAGE (**C** and **D**). After complete cleavage (**D**) the protein solution was loaded on Superdex 200 10/300 size exclusion column which results in two peaks (**E**). The first peak at 12.87 mL contains the hVDAC1-nanodisc whereas the second peak at 17.64 mL contains the GB1.

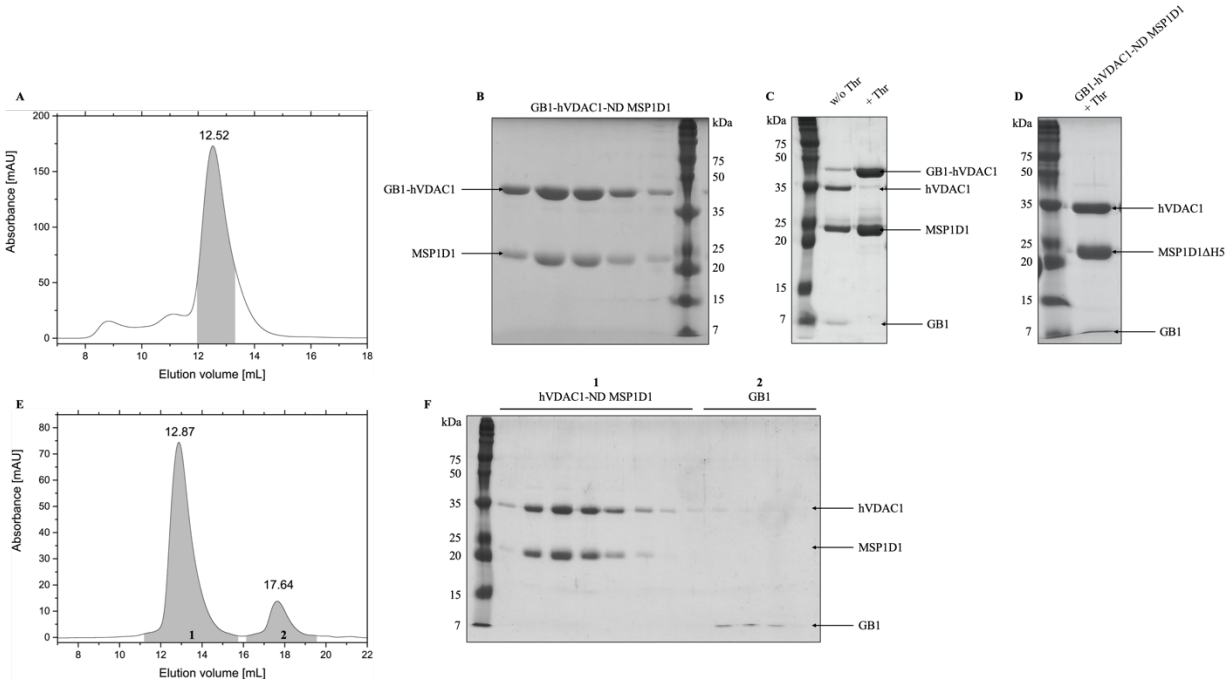

Figure 49: Quantification strategy of GB1-tagged hVDAC1 in nanodiscs using SEC. ***A*** *Size exclusion chromatography of GB1-hVDAC1 in MSP1D1-ND.* ***B*** *SDS-PAGE analysis of the main peak of GB1-hVDAC1 in MSP1D1-ND.* ***C*** *Thrombin cleavage of GB1-hVDAC1 showing an incomplete cleavage whereas* ***D*** *shows a complete cleavage of GB1 from hVDAC1.* ***E*** *Size exclusion chromatography of completely cleaved GB1-hVDAC1 in MSP1D1-ND at which the first peak represents the hVDAC1 nanodiscs and the second peak the GB1. Integrals for calculating the ratio of hVDAC1 to nanodiscs are given in grey.* ***F*** *SDS-PAGE analysis of the two peaks of the size exclusion chromatography (****E****).*

By determining the integrals of the two peaks, using OriginPro 9G the molar ratio of hVDAC1 to nanodiscs could be calculated. To do this, the equations (1–3) were used. In the first step equation 1 quantifies the amount of GB1, which can be set equal to the inserted hVDAC1. In the next step the pseudo particle number of the nanodiscs is back-calculated by using equation 2. As a final step the number of hVDAC1 per nanodisc can be calculated by the just using the numbers obtained with equations 1 and 2.

$$n_{GB1} = \frac{Int_{GB1}}{\varepsilon_{GB1}} \; ; \; n_{hVDAC1} = n_{GB1} \tag{1}$$

$$n_{ND} = \frac{Int_{ND+hVDAC1} - (n_{GB1} \cdot \varepsilon_{hVDAC1})}{2 \cdot \varepsilon_{MSP}} \tag{2}$$

$$R = \frac{n_{hVDAC1}}{n_{ND}} \tag{3}$$

The quantification of the different species in each sample, where the ratios and MSP variants were adjusted, were determined using the integrals of the UV absorption profiles

during size exclusion chromatography. In **Table 20** and **Table 21** (see appendix chapter V) the corresponding integrals, the calculated values for n_{GB1} and n_{ND} as well as the final hVDAC1 per nanodisc ratio R are listed. For their calculation the determined extinction coefficient of GB1 of 10006 $cm^{-1}M^{-1}$ (elucidation see below) was used. For each ratio of hVDAC1 per MSP during the assembly three SEC runs were performed. These resulted in three R-values for each ratio enabling the calculation of mean values and standard deviations.

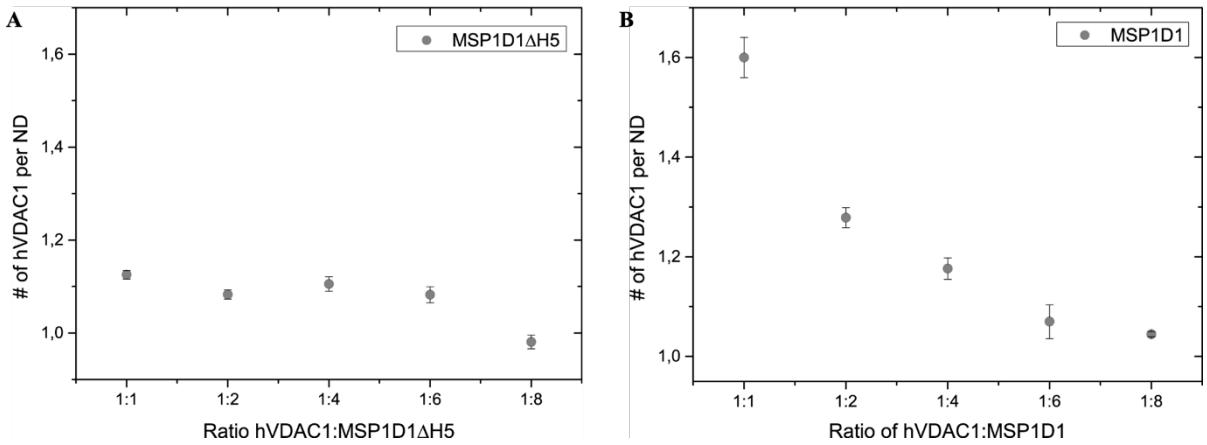

Figure 50: Quantity of hVDAC1 in MSP nanodiscs. *Calculated ratio of hVDAC1 to MSP1D1ΔH5 (**A**) and MSP1D1 (**B**), respectively, during ND assembly, revealing mainly 1 hVDAC1 in MSP1D1ΔH5-ND and up to 1.6 hVDAC1 in MSP1D1-ND depending on the hVDAC1.MSP ratio.*

For verifying this method and to apply a second alternative, the GB1-protein was fused to MSP1D1ΔH5. The GB1-fusion at MSP gives the opportunity to analyze the quantity of a membrane protein in nanodiscs, for which the GB1-fusion is not applicable. Additionally, the exact extinction coefficient of cleaved GB1 could be calibrated by using empty nanodiscs. Thereby, the quantity of GB1 has to be equal the amount of MSP.

His_6-TEV-GB1-Thr-MSP1D1ΔH5 (abbreviated GB1-MSP1D1ΔH5) was successfully produced and purified, resulting in a yield of 20 mg per 1 L main culture. Nanodisc assembly was performed according chapter 3.2.3. First, empty nanodiscs were assembled, in order to explore whether GB1-MSP fusion constructs are still able to form nanodiscs and also to determine the exact extinction coefficient of GB1 in this system for a more reliable calculation of the hVDAC1 quantity in nanodiscs. In **Figure 51 A** the SEC profiles of GB1-MSP1D1ΔH5 nanodiscs is shown. The corresponding homogenous peak fractions that have been used the following thrombin cleavage step are shaded in grey. Thrombin was then added to cleave off GB1, monitored by SDS-PAGE analysis (**B**). The second SEC run was not performed until the cleavage was completely successful. The right chromatogram (**C**) represents the empty

MSP1D1ΔH5 nanodiscs (peak 1) and GB1 (peak 2). A shift of the nanodisc elution volume from 13.12 mL to 13.32 mL correlates with the decrease in molecular weight. The integrals, colored in grey, were determined for further calculation of the extinction coefficient of GB1 resulting in 10006 $cm^{-1}M^{-1}$ (see appendix chapter V, **Table 22**).

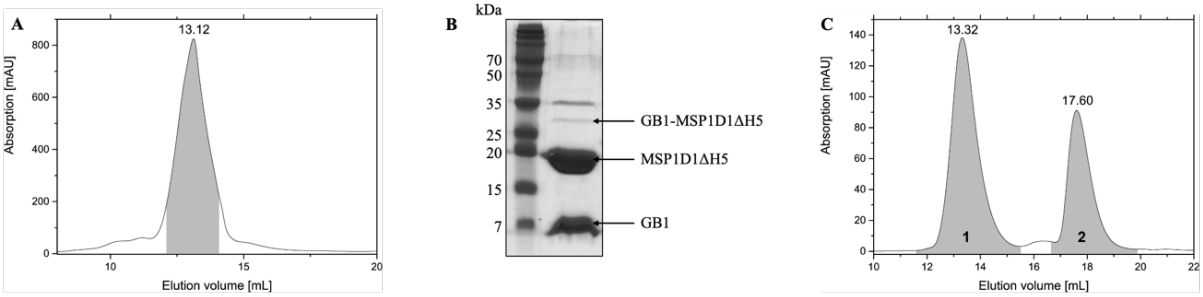

Figure 51: SEC of GB1-tagged MSP1D1ΔH5 nanodiscs and subsequent cleavage. ***A*** *Size exclusion chromatogram of empty GB1-MSP1D1ΔH5 nanodiscs using a lipid ratio of DMPC:DMPG = 3:1.* ***B*** *SDS-PAGE analysis of the thrombin cleavage of GB1-MSP1D1ΔH5, depicting an almost complete cleavage of GB1-MSP1D1ΔH5.* ***C*** *Size exclusion chromatogram of empty GB1-MSP1D1ΔH5 after Thrombin cleavage. Peak 1 represents empty MSP1D1ΔH5 nanodiscs and peak 2 represents GB1.*

Using GB1-MSP1D1ΔH5, hVDAC1 imbedded nanodisc were assembled. The assembly was performed according to protocol (chapter 3.2.3), resulting in a single peak with a small amount of additional aggregates at earlier elution volume (**A**) in the first sec run. For thrombin cleavage the peak fractions colored in grey were combined. After complete cleavage, proven by SDS-PAGE analysis (**B**) the second SEC was performed, resulting in peak 1 and peak 2, representing hVDAC1 in MSP1D1ΔH5 nanodiscs and GB1. The determined integrals (see appendix chapter V, **Table 22**) were used to calculate the amount of hVDAC1 in nanodiscs, resulting in 1.08 ± 0.035 hVDAC1 per nanodisc using a 1:8 ratio of hVDAC1 to MSP1D1ΔH5 during assembly.

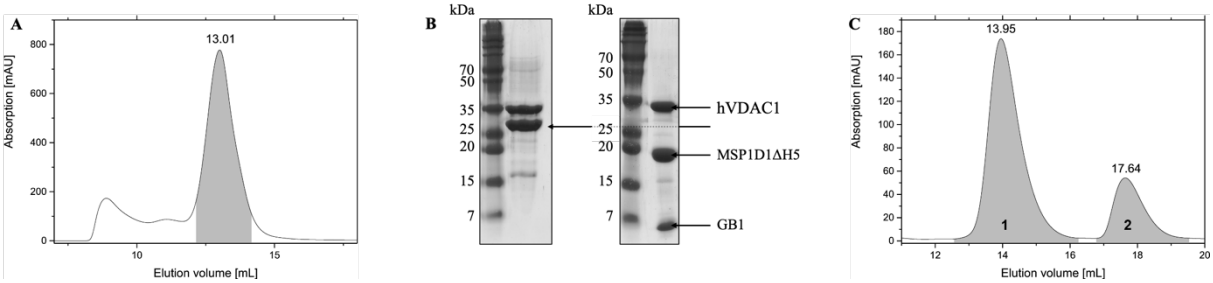

Figure 52: Quantification strategy of hVDAC1 in GB1-tagged MSP1D1ΔH5 using SEC. ***A*** *Size exclusion chromatography of hVDAC1 nanodiscs in GB1-MSP1D1ΔH5 (ratio 1:8) using a lipid ratio of DMPC:DMPG = 3:1.* ***B*** *SDS-PAGE analysis of hVDAC1 in GB1-MSP1D1ΔH5 before (left) and after (right) thrombin cleavage.* ***C*** *Size exclusion chromatogram of hVDAC1 in GB1-MSP1D1ΔH5 after Thrombin cleavage. Peak 1 represents hVDAC1 in MSP1D1ΔH5 and peak 2 represents GB1.*

Summarizing, a fast and easy method was established to detect the quantity of hVDAC1 in two sizes of nanodiscs using a GB1-tag. It has been seen, that one hVDAC1 is primarily present in both nanodisc sizes, but with adjusting the assembly conditions, nanodiscs harboring two hVDAC1 proteins could be assembled. Furthermore, it was possible to fuse GB1 to MSP, which gives rise to the opportunity for analyzing membrane proteins for which a fused tag is not possible.

5. Discussion

5.1. OEP21

The outer envelope protein with a molecular weight of 21 kDa (OEP21) functions as an anion channel, by transporting mainly phosphorylated carbohydrates. Until now, no detailed structure is published and therefore functional analysis based on its structure could not be conducted so far. In this project the high-resolution NMR structure of OEP21 was solved and further functional investigations were performed by applying biophysical and biochemical approaches.

OEP21-His_{10} was successfully expressed and purified. By improving the purification and refolding conditions, the yield could be increased up to 13 mg of refolded protein per 1 L culture. Thereby utilizing the stabilizing effect of NaP_i-buffer with additional ATP and yielding in around 25–35 % of refolded OEP21. In both refolding buffer systems, NaP_i and HEPES based, the yields are comparable, but differ in their SEC profiles. In NaP_i-buffer including ATP, couple of peaks can be observed, indicating an accumulation of LDAO and ATP, since both absorb at a wavelength of 280 nm to some extent. OEP21 in HEPES buffer in absence of any added metabolite, is resulting in a single peak followed by some LDAO accumulation. This uneven SEC profile following the main peak can be influenced by the LDAO concentration loaded on the column, meaning the concentration before SEC, affects the profile to some extent. Nonetheless for structural and functional analysis of OEP21, only the main peak was collected and concentrated for further studies. This refolding behavior is also detected for the different mutations of OEP21.

The first step of structural analysis of OEP21 was recording a CD spectrum with the corresponding thermal melting curves. Thereby the secondary structure and the stability of the protein was detected. As described in chapter 4.1.3.1 OEP21 has an overall β-sheet shape with a melting temperature of about 60 °C. In contrast to the secondary structure, the stability of OEP21 can be influenced especially by ATP, which increases the thermal melting temperature of about 5 °C, indicating a binding and thereby stabilizing effect of ATP to OEP21. But not only the increase in melting temperature, but also an increase in cooperative unfolding is detected compared to the apo state. This leads to the assumption that ATP binding results also in a compact and well-folded structure. The second most influential metabolite is GAP (with an increase of around 2 °C). These findings are consistent with the assumption, that OEP21 shuttles mainly GAP and has a higher affinity to ATP (K_D (ATP) = 200 µM, K_D (GAP) = 900

µM [13]). However, GAP has a less pronounced but opposite effect on the cooperativity compared to ATP, which substantiates the theory of GAP transport without strong binding to OEP21. In contrast to the positive impact of some metabolites an increasing pH reduces the stability (**Figure 24**). This result seems to be in conflict to the pH values detected in the chloroplasts, as the pH in the matrix of the chloroplasts is around 7, whereby in the cytosol the pH is approximately 8 [96]. Meaning that OEP21 is in case of an in vitro production and refolding in LDAO more stable at lower pH.

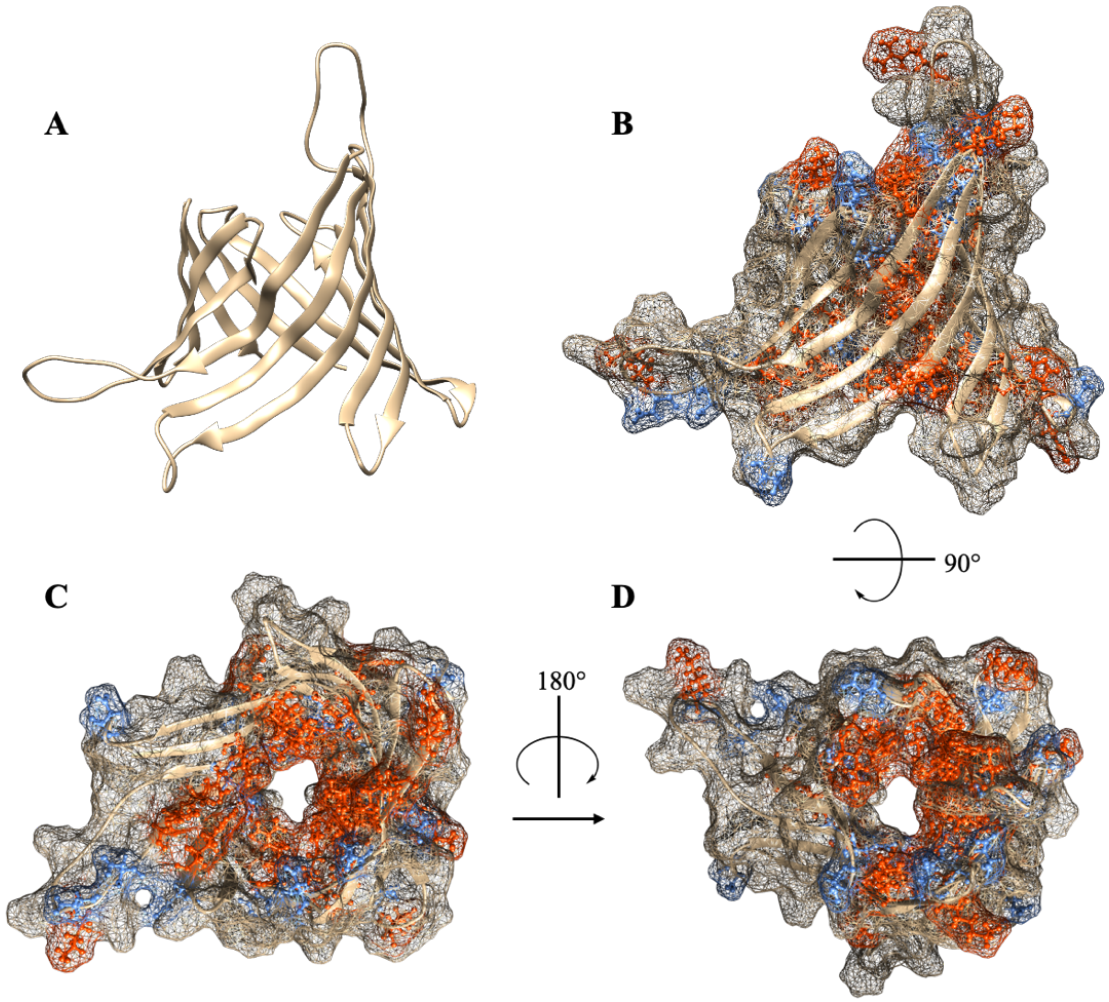

Figure 53: OEP21 and its positively charged inner surface. ***A*** *Ribbon representation of the OEP21 structure.* ***B, C, D*** *Representation of positive (red) and negative (blue) amino acids within the β-barrel using meshed surface and additional ball and stick representation for charged residues showing a predominantly positive charged passage through the channel.*

By means of NMR spectroscopy, the best refolding and NMR buffer conditions could be determined using NaP_i-based buffer system with additional ATP. In the following the backbone resonance assignment was performed using the a set of TROSY-based 3D-NMR experiments. With this, around 85 % of the amino acids could be assigned. The remaining 15

% amino acids are mainly located in the flexible loop regions, that most likely show adverse motions in the ms-to-µs time scale, leading to line broadening effects. Using about 700 NOE distance restrains, 110 hydrogen bond restrains and 255 backbone dihedral angle restrains (using TALOS+ [97]) a calculated structure with a backbone rmsd for all residues of 1.9 ± 0.3 Å and for heavy atoms the rmsd of 2.4 ± 0.3 Å is obtained. Regarding the ordered secondary structure, the resolution is highly improved with a rmsd value of 0.5 ± 0.1 Å for backbone and 1.1 ± 0.1 Å for heavy atoms. By analyzing the Ramachandran plot, meaning the angles between the C'-C_α and C_α-N angle, respectively, OEP21 consists predominantly out of β-strands. This is also seen by the differences between the C_α and C_β secondary chemical shift resonances (**Figure 28**) counting a 12 β-stranded barrel with different length. With these results, the previous hypothesis of an 8 β-barrel membrane protein is rebutted [13, 36]. The obtained structure proofs the assumption of the already mentioned flexible loop region, whose amino acids could not be assigned. A funnel-like shape of OEP21, which is formed by the β-strands, can be determined (**Figure 53 A**) with pore diameters ranging from 18 Å to 34 Å at the cytoplasmic or IMS side, respectively. This shape provides the theory, that the shuttled metabolites are transported mainly in one direction. With a closer look onto the amino acids, forming OEP21, it is quite apparent that 30 % of the residues are positively charged and almost all are directed into the β-barrel pore. (**Figure 53 B-D**) With these findings, it is obvious that OEP21 has a high interaction affinity to negatively charged phosphorylated carbohydrates and thereby are able to transport them from the intermembrane space of the chloroplast into the cytosol.

According to the NMR and BS^3 results, OEP21 exists as monomer, dimer and higher oligomers. Regarding the NMR spectra, the oligomerization of OEP21 can not only be detected by chemical shift perturbation, but also results in line broadening of the NMR signals. This effect is caused by an increase in molecular mass and therefore slower tumbling, which lead to faster T_2 relaxation. Evaluation of the CSPs reveals the dimerization site of OEP21 located at the side of the barrel with the longer β-strands. This dimerization or oligomerization, respectively, is induced by a lower LDAO concentration, which leads to the assumption, that OEP21 exists as an oligomer in its native state. This assumption is substantiated by the fact that OEP21 could not be inserted into MSP1D1ΔH5 or MSP1D1 nanodiscs. This oligomerization tendency can also be proven by BS^3 crosslinking, showing not only monomeric and dimeric OEP21, but even higher oligomers. As also shown by NMR spectroscopy with increasing LDAO concentrations, the equilibrium is shifted to the monomeric state. By analyzing the effect of metabolites on the oligomeric conformation, no significant change is recognized. Regarding

the oligomerization, it can be summarized that OEP21 occurs mainly as dimers and higher oligomers in a low detergent environment and metabolites do not affect this conformation. But with increasing LDAO concentrations, OEP21 can be forced into stable monomers.

The spin labeled 16-DOXYL stearic acid was used to probe the location of OEP21 in a micelle. It reveals a location of the loop regions outside of the micelle, while the anti-parallel β-sheets forming the barrel are inside the micelle. In addition, the PRE experiment also confirms the dimerization site of OEP21, since this site is partially shielded by a second OEP21 molecule in the micelle.

With the results of OEP21 dimerization the following model can be designed (**Figure 54**). It is manually aligned and not calculated, since specific experiments resulting in the exact orientation of the subunits, still have to be performed. The model shows a parallel dimer of OEP21, with the dimerization at the 'long' β-stand site.

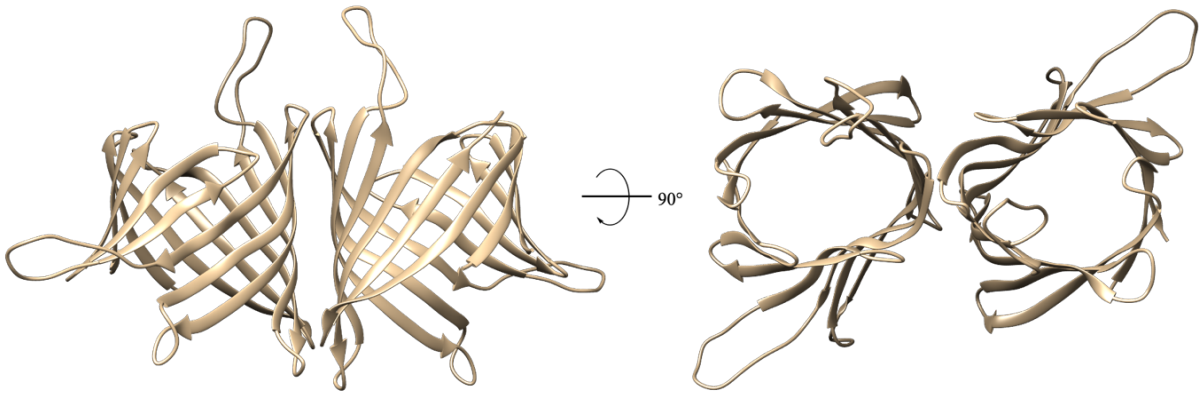

Figure 54: Hypothetic model of OEP21 dimer in a parallel orientation. *Manually aligned model of the OEP21 dimer interacting at the 'long' site of the barrel.*

Since OEP21 shuttles phosphorylated carbohydrates and is known to interact with ATP and GAP, these two metabolites were analyzed by NMR spectroscopy. In both cases, an effect is observable, whereby the impact of ATP is more significant, especially regarding the CSP of the signals. Compared to that, GAP has only a significant effect on the relative intensities. By mapping the CSP and relative intensities on the structure of OEP21, it is quite obvious that the changes occur mostly at the side with long β-strands. With these findings it can be conjectured, that ATP binds to OEP21 and thereby reduces the dynamical behavior. In contrast, GAP is shuttled through OEP21, binds loosely to OEP21 and induces a dynamic of OEP21 in a µs to ms range. This hypothesis is also substantiated by the previously analyzed stability measurements in addition of GAP and ATP using Far-UV CD spectroscopy.

For more detailed insights into the transport of GAP and ATP, four different mutants (K19A, R51A, R66A and R84) were cloned. These mutants were selected based on MD simulations (molecular dynamic simulation), done in corporation with Prof. Dr. Martin Zacharias and Dr. rer. nat. Manuel Hitzenberger, Chair of Theoretical Biophysics – Biomolecular Dynamics, Physics Department, Technical University Munich, Germany. These mutants show a statistically frequent binding to ATP and GAP and are located inside of the β-barrel (**Figure 55 B** and **C**). Expression, purification and refolding of these mutants worked in a same way and yielded in the same range as OEP21. Moreover, Far-UV CD spectroscopic measurements reveal a β-barrel structure, but in contrast to OEP21 the mutants have a slightly lower stability. But with addition of ATP the melting temperature increases again to a similar value as the wildtype. This behavior might be explained by the fact that ATP stabilizes OEP21 due to binding with several positively charged amino acids inside the barrel.

To analyze the transport efficiency of OEP21 and its mutants OEP21_K19A, OEP21_R51A, OEP21_R66A and OEP21_R84A, different assay approaches were designed. Thereby the focus lied on the identification of ATP or GAP transport. First, the luciferin-luciferase assay were applied to determine the transport of ATP, since ATP detection is quite sensitive. By analyzing the achieved data, a similar curve progression was detected for all mutants and no significant reduction in ATP transport was determined. The reference without any additional OEP21 and also adding 0.002 % Triton X-100, exhibits already a tendency to leak. The shape and fast luminescence reaction, compared to the reaction with 1 % Triton X-100, leads to the assumption, that liposomes undergo a breakup upon OEP21 addition. This can be explained by a higher detergent concentration, than expected, in the OEP21 sample.

Regarding the competitive assay of GAP and ATP a clear statement cannot be drawn, since GAP is interfering with the luciferin-luciferase reaction. These observations conclude, that this assay is not applicable to detect the transport of ATP through OEP21. Similar circumstances can be seen in the GAPDH-PGK-luciferase coupled assay, aimed the analysis of GAP transport. Here, ATP has an impact on the detection method, since it reacts already with luciferin. In summary, this assay as well as the luciferase-luciferin assay are not applicable to detect neither the transport of GAP nor of ATP. Since GAPDH is catalyzing the reaction of NAD to NADH/H^+ by using GAP, the absorption behavior at a wavelength of 340 nm is changed. The third approach is taking the advantage of this characteristic and measures the changes in absorption at 340 nm. Thereby, the transport of GAP, as well as the impact of ATP on GAP translocation can be observed. Due to the fact, that OEP21 is already added during the liposome preparation, no extra LDAO or Triton X-100 can interact with the liposomes and

break them. By analyzing the achieved data (**Figure 38**), the transport of GAP is recognized by an increase in absorbance at 340 nm. It has to be mentioned, that a data acquisition of the absorption at 280 nm is not possible, since ATP has its absorption maximum at 260 nm and contributes to the absorption at 280 nm. Therefore, the focus of the measurements is on the absorption at 340 nm. The amplitude is in the magnitude of the GAP and NAD reaction catalyzed by GAPDH to $NADH/H^+$ (appendix chapter IV, **Figure 59**). In case of the competitive assay of GAP and ATP a clear tendency of a reduction in amplitude up to 40 % in GAP transport, is recognized for an equimolar ATP and GAP concentration. By adding 1 mM ATP in a 2 mM GAP reaction mixture, the overall amplitude is not affected. This fits well to theory of Bölter *et al*., where the ratio of TP to ATP regulates the direction of transport [36]. But not only a reduction of the GAP transport, but also a delay is detected, described by the shift of the peak maximum. This indicates the kinetic of the GAP transport. Thereby the more ATP, the later starts the transport of GAP. This corresponds to the assumption, that the transport of GAP is hindered in presence of ATP, since ATP blocks the β-barrel. The data for 5 mM ATP do not fit directly to the other ATP measurements, since not a peak, but rather an increasing curve ending in a plateau is observed. This behavior cannot be sufficiently interpreted, but it can be reasonable suspect, that the liposomes seem to be unstable at higher ATP concentrations and thereby become leaky. This would explain the constant increase in absorption, without subsequent decline.

In contrast to that, the effects of the mutants are more significant. Compared to OEP21, the mutants K19A, R51A and R66A transport GAP in about 60 % less efficiency, whereas R84A does not have such a drastic effect and still transports 75 % GAP. In all cases the variants shuttle GAP slower than wt OEP21.

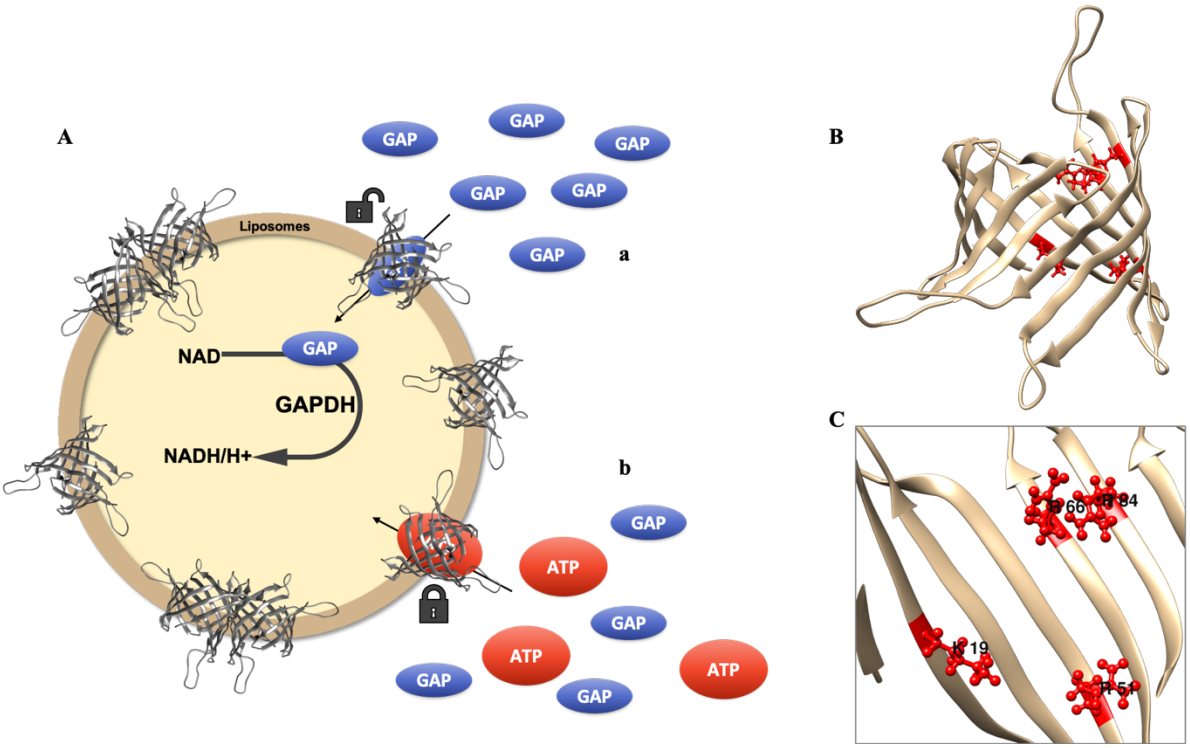

Figure 55: Regulation of GAP transport by ATP and mutagenesis. ***A*** *Schematic representation of the GAPDH assay.* ***a*** *Effective GAP transport through OEP21, but affected by removal of positively charged amino acids inside the barrel (K19A, R51A, R66A, R84A).* ***b*** *Competitive transport of ATP and GAP revealing a blockage of the channel through ATP.* ***B*** *Graphical representation of OEP21-mutants and their location in the β-barrel.* ***C*** *Closeup view of the mutated residues including labeling.*

Summarizing the outcome of the ATP/GAP-transport assays, only one out of three approaches was successful in context of an efficient method to detect the GAP translocation and the influence of ATP on the GAP transport. For achieving reliable results, it was also discovered, that the membrane protein has to be added during liposome preparation, to avoid leakage of the liposomes. Nonetheless, using OEP21 inserted into liposomes and NAD and GAPDH enclosed in those, a reliable method was designed to characterize the transport ability of OEP21 and its mutants. Applying this assay, the assumption, that the ratio of TP (in this case GAP) and ATP is influencing the transport of GAP, could be demonstrated. Thereby, a TP/ATP-ratio greater than one, does not influence the transport, whereas a ratio of one or lower decreases the translocation of GAP significantly, due to preferential binding of ATP. Three out of four mutations, OEP21_K19A, OEP21_R51A and OEP21_R66A, do have a significant impact on GAP transport, whereas OEP21_R84A reduced the translocation of GAP just slightly compared to wildtype OEP21.

The results of this assay are in agreement with the received MD simulations, resulting in a blocked OEP21 channel by ATP and a transport of GAP from the narrow side of the pore to the widely open side by interaction of especially the residues K19, R51 and R66 (**Figure 56**).

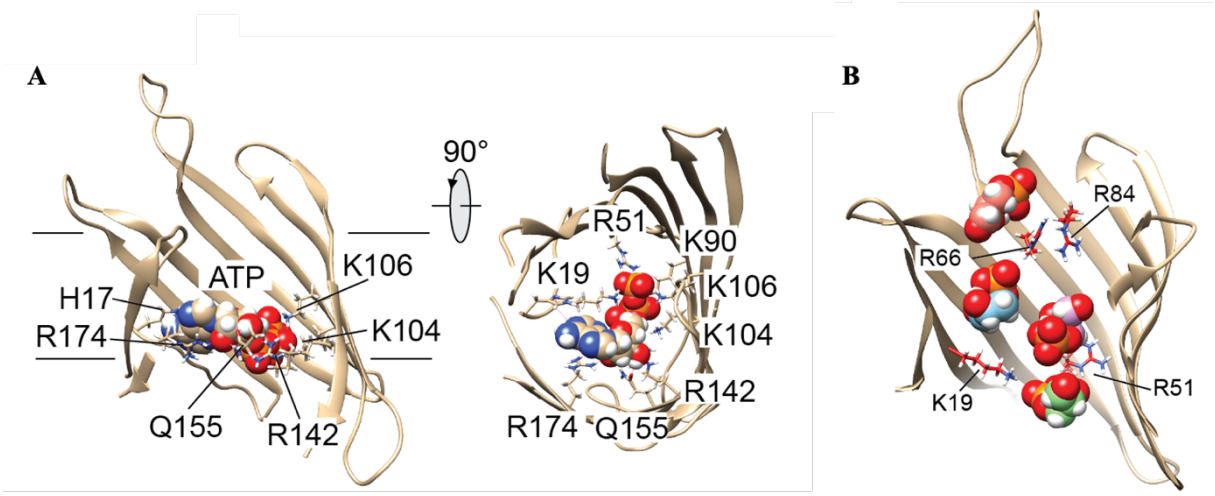

Figure 56: OEP21 and its interaction to GAP and ATP. ***A*** *Representation of ATP blocking OEP2 with involved amino acids labeled.* ***B*** *Detailed view on the GAP transport through OEP21 with involved amino acids. Figures were produced on basis of MD simulations performed by Dr. Manuel Hitzenberger, Chair of Theoretical Physics – Biomolecular Dynamics, Physics Department, Technical University Munich, Germany.*

As seen in MD simulation ATP binds to OEP21, whereas GAP is translocated. Due to the fact, that these MD simulations were performed using OEP21 without the His-tag, wtOEP21 (OEP21 without His-tag) were produced for additional structural investigation. These results should determine the effect of the C-terminal His-tag, which comes along with additional charges, on the already obtained structure of OEP21-His_{10}. The expression was not as successful as the construct with His-tag. It yielded in 16 mg wtOEP21 in 6 M GdmCl buffer per liter expression, which equals to 45 % of the yield produced with OEP21-His_{10}. Due to the missing His-tag, the purification was performed using a SP Sepharose gravity flow chromatography. This resulted in a protein sample with higher impurities. Even the final purification step of using a size exclusion chromatography did not remove those impurities completely. However, the SEC profile depicts a very similar chromatogram compared to OEP21-His_{10} with similar elution volumes. Also, Far-UV CD spectroscopic measurements indicate, that wtOEP21 has a β-strand secondary structure and compared to OEP21-His_{10}, with a slightly higher thermal stability. Regarding the flat cooperativity of the melting curve compared to OEP21-His_{10}, wtOEP21 indicates a more flexible structure. Additional ATP stabilizes wtOEP21, but in contrast to OEP21-His_{10}, the changes in steepness of the cooperativity are negligible. However, it cannot be precluded, that differences in these measurements of wtOEP21 and OEP21-His_{10} is caused by the impurities in the wtOEP21

sample. In any case, the very similar T_m and the characteristic CD spectrum for a β-sheet secondary structure suggests that this construct is correctly folded.

To verify these findings, $^{2}H,^{15}N$-wtOEP21 was expressed, purified, refolded and finally analyzed by NMR spectroscopy. First it has to be mentioned, that the overall peak distribution in the 2D-[$^{1}H,^{15}N$]-TROSY is comparable to OEP21-His_{10} and most of the peak assignment can be transferred. The overall shift of the signals can be reason with a different temperature during data acquisition. Analyzing wtOEP21 by Far-UV-CD and NMR spectroscopy, it can be claimed, that the His_{10}-tag at the C-terminal end is not affecting the structure of OEP21.

In conclusion the chloroplastic membrane protein OEP21 was successfully expressed and purified. By optimizing the refolding conditions correctly folded protein in LDAO micelles was achieved, evidenced by CD and NMR spectroscopy. Furthermore, using 2D- and 3D-NMR experiments, a high-resolution structure of OEP21 was determined. It reveals a 12 β-stranded barrel structure in a funnel-like shape with a highly positively charged inside and its loop regions located outside of the LDAO micelle. Additionally, it was detected, that OEP21 forms tight oligomers, but can be forced into a monomeric state at high LDAO concentrations of ~500 mM. Metabolites do not affect this oligomeric state, but do interact with OEP21. Among those, ATP has the highest impact on the protein, by stabilizing it up to 5 °C regarding the OEP21-His_{10} construct and reveal a higher influence on the structure as detected by CD and NMR spectroscopy. The transport of GAP through OEP21 or single point variants as well as the inhibiting effect of ATP, could be characterized by an established GAPDH-dependent assay. These data are consistent with the assumption, that OEP21 is able to transport TP, depending on their production levels in the chloroplasts. This means, that a high TP concentration in the intermembrane space preferably present during the prominent dark reaction, lead to an outward transport. In contrast, during light reaction the concentration of ATP is higher and TPs will not or rarely be transported. Thereby the conditions, the transport is based on, could be verified by this assay. Regarding the GAP transport itself, four single point mutations were inserted and a significant decrease with three out of four mutants could be detected. This confirms, that K19, R51 and R66 are essential amino acids in the transport of GAP through the barrel. Combining the obtained results, it can be hypothesized, that ATP binds tightly to OEP21 and thus blocks the channel to some extent, leading to a modulation of GAP transport by its ratio to ATP.

5.2. hVDAC1

The oligomeric state of the human voltage-dependent anion channel hVDAC1 might be crucial for the regulation of cell survival or death. Therefore, research on this topic requires hVDAC1 in a defined oligomeric state. This in turns needs a stable and reliable method to determine the quantity e. g. in phospholipid nanodiscs for further investigation.

Previous studies presented a reliable method to purify and refold hVDAC1 in LDAO micelles as well as incorporation of hVDAC1 into phospholipid nanodiscs using DMPC [11, 38, 57]. In this work, hVDAC1 nanodiscs were prepared, using a DMPC to DMPG ratio of 3:1 (see chapter 3.2.3). This lipid ratio is known to be optimized for the NMR analysis of hVDAC1. Since natural lipid membranes also have a negative net charge, the addition of DMPG represent a step into a more realistic environment [70]. Nonetheless, incorporation of hVDAC1 into MSP1D1 and MSP1D1ΔH5 nanodiscs, using a DMPC to DMPG ratio of 3:1 results in homogeneous SEC peaks (**Figure 46**). The SDS-PAGE analysis reveals - in both cases - a higher amount of MSP compared to hVDAC1, which fits to the overall structure of two MSP proteins and one hVDAC1 protein forming the nanodisc.

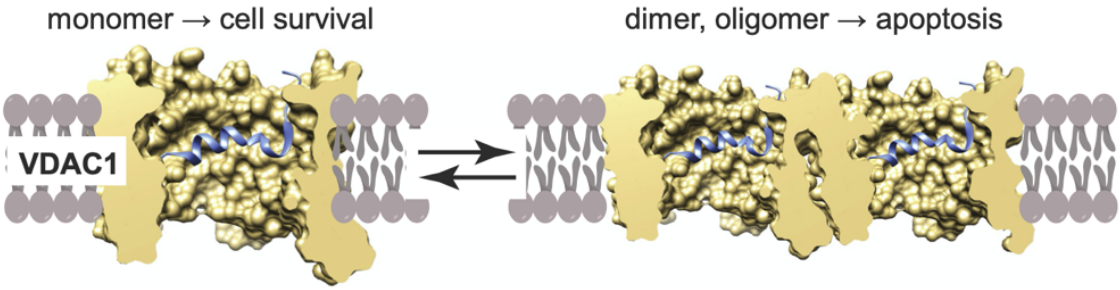

Figure 57: Representation of hVDAC1 as monomer and dimer. *Monomeric hVDAC1 sustains cell functions and its survival, while hVDAC1 dimers and higher oligomers lead to apoptosis. [95]*

Since previous studies have been determined, that one or more hVDAC1 exists in phospholipid nanodiscs depending on its size [38, 98], a fast and easily accessible method to determine the quantity of hVDAC1 could be established in this research project. To do this, the fusion construct GB1-hVDAC1 was successfully expressed and purified with the same conditions and protocol as used for hVDAC1. The fusion of the immunoglobulin-type B1 domain of protein G (GB1) to hVDAC1 yields in three times higher (150 mg to 50 mg per 1 L culture) production efficiency than without fusion protein. Also, the determined refolding efficiency of 80 % is about 2.7 times higher compared to hVDAC1. The increased expression

yield, as well as the more efficient refolding of GB1-hVDAC1 suggest, that GB1 functions as a solubility and expression level enhancing fusion protein, as seen in previous studies [99-101].

In the next step, nanodisc assembly were performed using two sizes of MSP, MSP1D1ΔH5 with a diameter of 8 nm and MSP1D1 with 10 nm. To assemble these nanodiscs, two different factors have to be considered: first, the number of lipids and second, the ratio of MSP to hVDAC1. The ratio is mainly responsible for the number of inserted membrane protein. The number of lipids was calculated using the inner diameter of 6 nm for MSP1D1ΔH5 or 8 nm for MSP1D1 and the surface area of 57 Å for DMPC and DMPG. Taking the diameter of hVDAC1 of 4 nm into account, it could be calculated that ~30 lipids per bilayer leaflet can fit into MSP1D1ΔH5 nanodiscs harboring hVDAC1. Using MSP1D1 nanodiscs, 60 or 40 lipids for one and two hVDAC1, respectively, was empirically determined. The ratio of hVDAC1 to MSP (MSP1D1ΔH5 and MSP1D1) were screened from 1:1, 1:2, 1:4, 1:6 up to 1:8. In addition the amount of lipids was screened and adjusted to each hVDAC1 to MSP ratio. Various nanodisc assemblies were prepared with defined ratios of hVDAC1 to MSP to lipids and afterwards cleaved by thrombin to remove GB1. To perform the SEC run, the GB1 had to be completely proteolytically cleaved of from hVDAC1. Otherwise, the integral of the GB1 peak is reduced, while the hVDAC1-ND peak has an increased integral and thereby leading to incorrect calculations. After SEC the peaks of GB1 and hVDAC1-ND were integrated and with the evolved equations the number of inserted hVDAC1 was calculated. It has to be highlighted, that the integral is calculated for the entire GB1 and hVDAC1-ND peak, respectively. Finally, the quantity of hVDAC1 inserted into the two different MSP variants and assembled in different hVDAC1 to MSP ratios, was determined (**Figure 50**). Using MSP1D1ΔH5 for nanodisc assembly, the number of hVDAC1 inserted into ND is varying from 0.98 to 1.13 with an increasing MSP ratio. Interpreting these first results, MSP1D1ΔH5 with diameter of 8 nm is too small to harbor more than one hVDAC1. Regarding MSP1D1-ND, the quantity of hVDAC1 in nanodiscs is increasing, if an excess of hVDAC1 is available during ND assembly. This means, that MSP1D1 are able to harbor more than one hVDAC1. Nevertheless, since a 1:1 ratio of hVDAC1 to MSP1D1 is resulting in a quantity of 1.6 molecules of hVDAC1 per nanodiscs, it can be assumed, that a positive cooperative effect between two monomers occur or the stability of the nanodiscs is increased. Furthermore, since the cooperativity is not highly pronounced and can only be seen at relatively high hVDAC1 concentrations, it can be speculated that hVDAC1 is not forming a tight dimer.

In some cases, GB1 fusion to a certain membrane protein is not possible, leading to the need of the fusion construct GB1-MSP1D1ΔH5. This was additionally expressed and purified.

Compared to standard MSP production, the GB1 fusion seems to affect the expression and purification negatively, resulting in a reduced yield. Nevertheless, production of the GB1-fusion construct is still sufficient, so that nanodisc assembly can be performed. Another advantage of the GB1-MSP1D1ΔH5 construct was the determination of the exact extinction coefficient of GB1 in this system. For this, empty nanodiscs were assembled, GB1 was cleaved off and the resulting integrals were used to back-calculate the extinction coefficient to 10006 $cm^{-1}M^{-1}$. Using this recalculated value, a reliable number of inserted hVDAC1 could be calculated. Additionally, GB1-MSP1D1ΔH5 was used to assemble hVDAC1 inserted nanodiscs with a defined ratio of 1:8, thereby obtaining a quantity of 1.08 hVDAC1 in nanodiscs. This number is close to the quantity achieved from the nanodisc assembly using GB1-hVDAC1 and MSP1D1ΔH5 in the same ratio. With this result it can be conclude, that a GB1-fusion to MSP is possible and does not have an impact on the insertion of a membrane protein during nanodisc assembly.

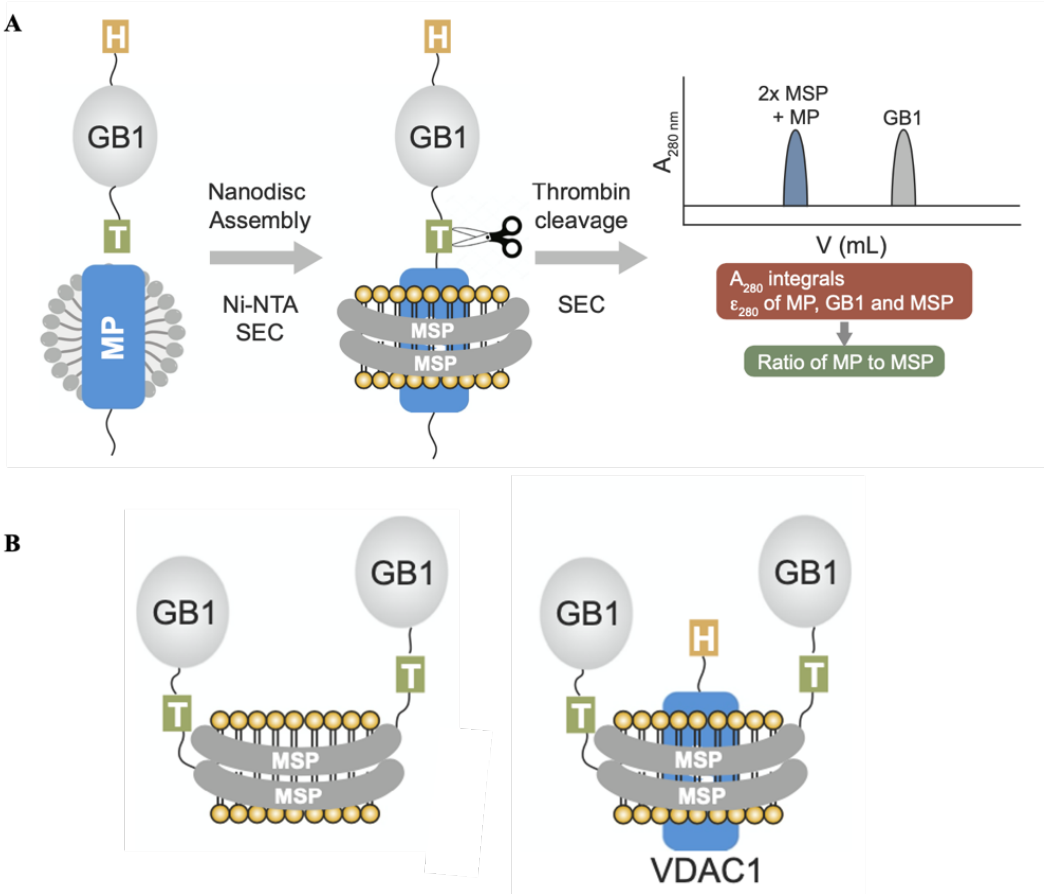

Figure 58: Quantification strategy of membrane proteins inserted into phospholipid nanodiscs. ***A*** *General procedure to determine the quantity of a membrane protein inserted into MSP nanodiscs by proteolytical cleavage of GB1 and subsequent SEC..* ***B*** *Schematic representation of empty and hVDAC1 inserted nanodisc with GB1 fused to MSP. [95]*

In conclusion this approach demonstrates a reliable and simple method to determine the quantity of a membrane protein in nanodiscs, which is available in almost every biochemistry laboratory. The GB1 can be fused to either the membrane protein or to MSP, if the fusion to the membrane protein is restricted in any kind. Furthermore, it could be demonstrated that the ratio of hVDAC1 and MSP is influencing the quantity of inserted membrane protein. Using this information, suitable nanodisc assembly conditions can be chosen in order to specifically obtain a monomeric or dimeric species for further structural and functional studies.

6. Outlook

6.1. Further investigation of OEP21

The chloroplastic membrane protein OEP21 was first characterized by Bölter *et al.* as an anion-selective channel for phosphorylated carbohydrates. Previous research suggests a structure of eight β-strands. In this project a high-resolution structure of OEP21 was determined, using NMR spectroscopy, revealing a 12 β-stranded barrel. With this knowledge, a closer look on the structural changes induced by GAP and ATP were obtained and by developing a reliable assay, the translocation of GAP and the competitive transport with ATP were analyzed.

Applying the obtained structure, further investigations could be performed. Analyzing the oligomeric state of OEP21 using PROXYL-tagged OEP21 would lead to a better knowledge on the exact location of the dimerization. The PROXYL-label next to the dimerization site causes signal extinction within 15 Å. Therefore, mutagenesis on OEP21 has to be performed to generate artificially cloned cysteines and an appropriate replacement for its native cysteine. Preferable these cysteines should be located near the dimerization site and in a loop region. Another interesting aspect concerning the overall structure of OEP21 would be the NMR structure in a lipid bilayer, compared to the obtained structure in LDAO micelles. Therefore, OEP21 has to be successfully transferred into a bilayer system. This requires a more detailed screening of different bilayer systems and optimization of the assembly conditions, since previous attempts failed so far.

Analyzing the transport of GAP and ATP, a reliable assay was established. Nevertheless, further extended experiments could be obtained by cloning additional mutations into OEP21. A stepwise mutation of all four residues, analyzed so far, could be performed. This results in a drastically reduction of charges inside the pore. The complete knockout of important residues for the GAP translocation could lead to the assumption, that the mutant is incapable to transport GAP.

Further analysis can be performed, detecting a possible ATP transport of OEP21. Adapting the optimized assay conditions, luciferase and luciferin could be enclosed in liposomes and OEP21 is imbedded in the lipid bilayer. Subsequently, the reaction could be started by adding ATP to the reaction volume. By using this assay design, the presumed ATP translocation might be detectable. Additionally, the exact K_D values of ATP and GAP would be of interest. Since an ITC measurement with membrane proteins solubilized in detergent

micelles is challenging, a NMR spectroscopic approach could be applied by stepwise titration of the metabolites.

Since OEP21 facilitates not only the transport of GAP and ATP, but also other phosphorylated carbohydrates, a more detailed analysis of their interaction with OEP21 could be performed. Therefore, a method has to be established to investigate different metabolites. Nonetheless, NMR spectroscopy can be used to detect, whether interaction occurs and how this interaction can be categorized. As a result, weak and strong binding or changes in dynamics, induced by the variety of metabolites, can be analyzed. Obtaining these insights, detailed information on the transport mechanism of various metabolites could be determined.

Now, the obtained structure of OEP21 opens up the various opportunities for a further research on its function.

6.2. Further investigation of hVDAC1

hVDAC1 is one of the most analyzed β-barrel membrane protein, which carries out a number of diverse functions. Previous research suggests a connection of t oligomeric state of hVDAC1 and its role in apoptosis. This is triggered by its interaction with Bcl-xL [54, 57, 102]. Therefore, the designed method, using a GB1-fusion construct for quantification of membrane proteins in MSP nanodiscs, is valuable for further research. Applying the new method, assembly conditions were screened, to determine the quantity of hVDAC1 in nanodiscs. The defined monomeric or dimeric samples of hVDAC1 in nanodiscs can now be analyzed in respect to its interaction of Bcl-xL or other partner proteins. This binding can be determined by using NMR spectroscopic experiments, such as 2D-[^{1}H,^{15}N]-TROSY. However, not only the interaction to partner proteins, but also a defined structure of monomer and dimer, respectively, in phospholipid nanodiscs, can be determined. The resulting structure of hVDAC1 in a lipid bilayer would be another important topic for further research, since all published NMR structures of hVDAC1 are solved in LDAO micelles (5JDP, 6TIQ, 2K4T and 6TIR) [2].

Nonetheless hVDAC1 is a highly analyzed membrane protein, but a lot of mechanistic aspects are still vague and further investigation is vital. The feasibility to assemble nanodiscs with a certain number of hVDAC1 facilitates a variety of new experiments were a defined the oligomeric state is required.

Literature

1. White, S. *Membrane proteins of known 3D structure* 1998-2020; Available from: https://blanco.biomol.uci.edu/mpstruc/.

2. Berman, H.M., et al., *The Protein Data Bank.* Nucleic Acids Research, 2000. **28**(1): p. 235-242.

3. Lodish H, B.A., Zipursky SL, et al. , *Molecular Cell Biology*. Vol. 4. 2000, New York: W. H. Freeman.

4. Goodman, S.R., *Medical Cell Biology*. 2007: Elsevier Science.

5. Stillwell, W., *Chapter 6 - Membrane Proteins*, in *An Introduction to Biological Membranes (Second Edition)*, W. Stillwell, Editor. 2016, Elsevier. p. 89-110.

6. Yeagle, P.L., *Chapter 10 - Membrane Proteins*, in *The Membranes of Cells (Third Edition)*, P.L. Yeagle, Editor. 2016, Academic Press: Boston. p. 219-268.

7. Yao, Y., et al., *Conformation of BCL-XL upon Membrane Integration.* Journal of molecular biology, 2015. **427**(13): p. 2262-2270.

8. Li, X., et al., *Structural modeling defines transmembrane residues in ADAM17 that are crucial for Rhbdf2–ADAM17-dependent proteolysis.* Journal of Cell Science, 2017. **130**(5): p. 868.

9. Hasegawa, N., et al., *X-ray structure analysis of bacteriorhodopsin at 1.3 Å resolution.* Scientific Reports, 2018. **8**(1): p. 13123.

10. Egloff, P., et al., *Structure of signaling-competent neurotensin receptor 1 obtained by directed evolution in Escherichia coli.* Proceedings of the National Academy of Sciences of the United States of America, 2014. **111**(6): p. E655-E662.

11. Hiller, S., et al., *Solution structure of the integral human membrane protein VDAC-1 in detergent micelles.* Science (New York, N.Y.), 2008. **321**(5893): p. 1206-1210.

12. Hagn, F., et al., *Optimized Phospholipid Bilayer Nanodiscs Facilitate High-Resolution Structure Determination of Membrane Proteins.* Journal of the American Chemical Society, 2013. **135**(5): p. 1919-1925.

13. Hemmler, R., et al., *Molecular Properties of Oep21, an ATP-regulated Anion-selective Solute Channel from the Outer Chloroplast Membrane.* Journal of Biological Chemistry, 2006. **281**(17): p. 12020-12029.

14. Zunke, F. and S. Rose-John, *The shedding protease ADAM17: Physiology and pathophysiology.* Biochimica et Biophysica Acta (BBA) - Molecular Cell Research, 2017. **1864**(11, Part B): p. 2059-2070.

15. Horiuchi, T., et al., *Transmembrane TNF-alpha: structure, function and interaction with anti-TNF agents.* Rheumatology (Oxford, England), 2010. **49**(7): p. 1215-1228.

16. Böhm, R., et al., *The Structural Basis for Low Conductance in the Membrane Protein VDAC upon β-NADH Binding and Voltage Gating.* Structure, 2020. **28**(2): p. 206-214.e4.

17. Subramaniam, S. and R. Henderson, *Molecular mechanism of vectorial proton translocation by bacteriorhodopsin.* Nature, 2000. **406**(6796): p. 653-657.

18. Bruncko, M., et al., *Studies Leading to Potent, Dual Inhibitors of Bcl-2 and Bcl-xL.* Journal of Medicinal Chemistry, 2007. **50**(4): p. 641-662.

19. Wang, J.L., et al., *The novel benzopyran class of selective cyclooxygenase-2 inhibitors. Part 2: The second clinical candidate having a shorter and favorable human half-life.* Bioorganic & Medicinal Chemistry Letters, 2010. **20**(23): p. 7159-7163.

20. Ubarretxena-Belandia, I. and D.M. Engelman, *Helical membrane proteins: diversity of functions in the context of simple architecture.* Current Opinion in Structural Biology, 2001. **11**(3): p. 370-376.

21. Trenker, R., M.E. Call, and M.J. Call, *Crystal Structure of the Glycophorin A Transmembrane Dimer in Lipidic Cubic Phase.* Journal of the American Chemical Society, 2015. **137**(50): p. 15676-15679.

22. Lee, E.F. and W.D. Fairlie, *The Structural Biology of Bcl-x(L).* International journal of molecular sciences, 2019. **20**(9): p. 2234.

23. Orzáez, M., E. Pérez-Payá, and I. Mingarro, *Influence of the C-terminus of the glycophorin A transmembrane fragment on the dimerization process.* Protein science : a publication of the Protein Society, 2000. **9**(6): p. 1246-1253.

24. Wimley, W.C., *The versatile β-barrel membrane protein.* Current Opinion in Structural Biology, 2003. **13**(4): p. 404-411.

25. Kleinschmidt, J.H., *Folding of β-barrel membrane proteins in lipid bilayers — Unassisted and assisted folding and insertion.* Biochimica et Biophysica Acta (BBA) - Biomembranes, 2015. **1848**(9): p. 1927-1943.

26. Jensen, P.E. and D. Leister, *Chloroplast evolution, structure and functions.* F1000prime reports, 2014. **6**: p. 40-40.

27. Neuhaus, H.E. and R. Wagner, *Solute pores, ion channels, and metabolite transporters in the outer and inner envelope membranes of higher plant plastids.* Biochimica et Biophysica Acta (BBA) - Biomembranes, 2000. **1465**(1): p. 307-323.

28. Awai, K., et al., *A phosphatidic acid-binding protein of the chloroplast inner envelope membrane involved in lipid trafficking.* Proceedings of the National Academy of Sciences, 2006. **103**(28): p. 10817.

29. Jarvis, P. and J. Soll, *Toc, Tic, and chloroplast protein import.* Biochimica et Biophysica Acta (BBA) - Molecular Cell Research, 2001. **1541**(1): p. 64-79.

30. Trentmann, O., et al., *Identification of chloroplast envelope proteins with critical importance for cold acclimation.* bioRxiv, 2019: p. 813725.

31. Flügge, U.-I., et al., *The role of transporters in supplying energy to plant plastids.* Journal of Experimental Botany, 2011. **62**(7): p. 2381-2392.

32. Flügge, U.I. and R. Benz, *Pore-forming activity in the outer membrane of the chloroplast envelope.* FEBS Letters, 1984. **169**(1): p. 85-89.

33. Gutierrez-Carbonell, E., et al., *The Distinct Functional Roles of the Inner and Outer Chloroplast Envelope of Pea (Pisum sativum) As Revealed by Proteomic Approaches.* Journal of Proteome Research, 2014. **13**(6): p. 2941-2953.

34. Röhl, T., M. Motzkus, and J. Soll, *The outer envelope protein OEP24 from pea chloroplasts can functionally replace the mitochondrial VDAC in yeast.* FEBS Letters, 1999. **460**(3): p. 491-494.

35. Bölter, B. and J. Soll, *Ion channels in the outer membranes of chloroplasts and mitochondria: open doors or regulated gates?* The EMBO journal, 2001. **20**(5): p. 935-940.

36. Bölter, B., et al., *A rectifying ATP-regulated solute channel in the chloroplastic outer envelope from pea.* The EMBO journal, 1999. **18**(20): p. 5505-5516.

37. Shoshan-Barmatz, V. and D. Gincel, *The voltage-dependent anion channel.* Cell Biochemistry and Biophysics, 2003. **39**(3): p. 279-292.

38. Raschle, T., et al., *Structural and Functional Characterization of the Integral Membrane Protein VDAC-1 in Lipid Bilayer Nanodiscs.* Journal of the American Chemical Society, 2009. **131**(49): p. 17777-17779.

39. Hiller, S., et al., *Backbone and ILV side chain methyl group assignments of the integral human membrane protein VDAC-1.* Biomolecular NMR assignments, 2010. **4**(1): p. 29-32.

40. Reif, M.M., et al., *The N-Terminal Segment of the Voltage-Dependent Anion Channel: A Possible Membrane-Bound Intermediate in Pore Unbinding.* Journal of Molecular Biology, 2019. **431**(2): p. 223-243.

41. Noskov, S.Y., et al., *Current state of theoretical and experimental studies of the voltage-dependent anion channel (VDAC).* Biochimica et Biophysica Acta (BBA) - Biomembranes, 2016. **1858**(7, Part B): p. 1778-1790.

42. Martínez-Reyes, I. and N.S. Chandel, *Mitochondrial TCA cycle metabolites control physiology and disease.* Nature Communications, 2020. **11**(1): p. 102.

43. Friedman, J.R. and J. Nunnari, *Mitochondrial form and function.* Nature, 2014. **505**(7483): p. 335-343.

44. Berg, J.M., et al., *Stryer Biochemie*. 2009: Spektrum Akademischer Verlag.

45. Kühlbrandt, W., *Structure and function of mitochondrial membrane protein complexes.* BMC Biology, 2015. **13**(1): p. 89.

46. Wiedemann, N. and N. Pfanner, *Mitochondrial Machineries for Protein Import and Assembly.* Annual Review of Biochemistry, 2017. **86**(1): p. 685-714.

47. Messina, A., et al., *VDAC isoforms in mammals.* Biochimica et Biophysica Acta (BBA) - Biomembranes, 2012. **1818**(6): p. 1466-1476.

48. Geula, S., D. Ben-Hail, and V. Shoshan-Barmatz, *Structure-based analysis of VDAC1: N-terminus location, translocation, channel gating and association with anti-apoptotic proteins.* Biochemical Journal, 2012. **444**(3): p. 475-485.

49. De Pinto, V., et al., *Determination of the Conformation of the Human VDAC1 N-Terminal Peptide, a Protein Moiety Essential for the Functional Properties of the Pore.* ChemBioChem, 2007. **8**(7): p. 744-756.

50. Reymann, S., et al., *Further Evidence for Multitopological Localization of Mammalian Porin (VDAC) in the Plasmalemma Forming Part of a Chloride Channel Complex Affected in Cystic Fibrosis and Encephalomyopathy.* Biochemical and Molecular Medicine, 1995. **54**(2): p. 75-87.

51. Bohm, R., et al., *The Structural Basis for Low Conductance in the Membrane Protein VDAC upon beta-NADH Binding and Voltage Gating. LID - S0969-2126(19)30433-2 [pii] LID - 10.1016/j.str.2019.11.015 [doi].* (1878-4186 (Electronic)).

52. Shoshan-Barmatz, V., E.N. Maldonado, and Y. Krelin, *VDAC1 at the crossroads of cell metabolism, apoptosis and cell stress.* Cell stress, 2017. **1**(1): p. 11-36.

53. Huang, H., et al., *An interaction between Bcl-xL and the voltage-dependent anion channel (VDAC) promotes mitochondrial Ca2+ uptake.* The Journal of biological chemistry, 2013. **288**(27): p. 19870-19881.

54. Arbel, N., D. Ben-Hail, and V. Shoshan-Barmatz, *Mediation of the Antiapoptotic Activity of Bcl-xL Protein upon Interaction with VDAC1 Protein.* Journal of Biological Chemistry, 2012. **287**(27): p. 23152-23161.

55. Shimizu, S., et al., *Bcl-2 family proteins regulate the release of apoptogenic cytochrome c by the mitochondrial channel VDAC.* Nature, 1999. **399**(6735): p. 483-487.

56. Shimizu, S., et al., *BH4 domain of antiapoptotic Bcl-2 family members closes voltage-dependent anion channel and inhibits apoptotic mitochondrial changes and cell death.* Proceedings of the National Academy of Sciences of the United States of America, 2000. **97**(7): p. 3100-3105.

57. Malia, T.J. and G. Wagner, *NMR Structural Investigation of the Mitochondrial Outer Membrane Protein VDAC and Its Interaction with Antiapoptotic Bcl-xL.* Biochemistry, 2007. **46**(2): p. 514-525.

58. Shi, Y., et al., *Identification of the protein–protein contact site and interaction mode of human VDAC1 with Bcl-2 family proteins.* Biochemical and Biophysical Research Communications, 2003. **305**(4): p. 989-996.

59. Klöpfer, K. and F. Hagn, *Beyond detergent micelles: The advantages and applications of non-micellar and lipid-based membrane mimetics for solution-state NMR.* Progress in Nuclear Magnetic Resonance Spectroscopy, 2019. **114-115**: p. 271-283.

60. Oliver, R.C., et al., *Dependence of Micelle Size and Shape on Detergent Alkyl Chain Length and Head Group.* PLOS ONE, 2013. **8**(5): p. e62488.

61. Konstantin, S.M. and D.N. Kirill, *Membrane mimetics for solution NMR studies of membrane proteins.* Nanotechnology Reviews, 2017. **6**(1): p. 15-32.

62. Tulumello, D.V. and C.M. Deber, *Efficiency of detergents at maintaining membrane protein structures in their biologically relevant forms.* Biochimica et Biophysica Acta (BBA) - Biomembranes, 2012. **1818**(5): p. 1351-1358.

63. Frey, L., et al., *Micelles, Bicelles, and Nanodiscs: Comparing the Impact of Membrane Mimetics on Membrane Protein Backbone Dynamics.* Angewandte Chemie International Edition, 2017. **56**(1): p. 380-383.

64. Ge, L., et al., *Molecular Plasticity of the Human Voltage-Dependent Anion Channel Embedded Into a Membrane.* Structure (London, England : 1993), 2016. **24**(4): p. 585-594.

65. Glover, K.J., et al., *Structural evaluation of phospholipid bicelles for solution-state studies of membrane-associated biomolecules.* Biophysical journal, 2001. **81**(4): p. 2163-2171.

66. Triba, M.N., D.E. Warschawski, and P.F. Devaux, *Reinvestigation by phosphorus NMR of lipid distribution in bicelles.* Biophysical journal, 2005. **88**(3): p. 1887-1901.

67. Mineev, K.S., et al., *Characterization of Small Isotropic Bicelles with Various Compositions.* Langmuir, 2016. **32**(26): p. 6624-6637.

68. Fang, Y., O. Gursky, and D. Atkinson, *Lipid-Binding Studies of Human Apolipoprotein A-I and Its Terminally Truncated Mutants.* Biochemistry, 2003. **42**(45): p. 13260-13268.

69. Puthenveetil, R., K. Nguyen, and O. Vinogradova, *Nanodiscs and Solution NMR: preparation, application and challenges.* Nanotechnology reviews, 2017. **6**(1): p. 111-126.

70. Hagn, F., M.L. Nasr, and G. Wagner, *Assembly of phospholipid nanodiscs of controlled size for structural studies of membrane proteins by NMR.* Nature protocols, 2018. **13**(1): p. 79-98.

71. Bayburt, T.H. and S.G. Sligar, *Membrane protein assembly into Nanodiscs.* FEBS letters, 2010. **584**(9): p. 1721-1727.

72. Corpet, F., *Multiple sequence alignment with hierarchical clustering.* Nucleic acids research, 1988. **16**(22): p. 10881-10890.

73. Goto, N.K., et al., *A robust and cost-effective method for the production of Val, Leu, Ile (delta 1) methyl-protonated 15N-, 13C-, 2H-labeled proteins.* Journal of Biomolecular Nmr, 1999. **13**(4): p. 369-374.

74. Partis, M.D., et al., *Cross-linking of protein by ω-maleimido alkanoylN-hydroxysuccinimido esters.* Journal of Protein Chemistry, 1983. **2**(3): p. 263-277.

75. Shi, J.-M., et al., *Bis(sulfosuccinimidyl) suberate (BS3) crosslinking analysis of the behavior of amyloid-β peptide in solution and in phospholipid membranes.* PloS one, 2017. **12**(3): p. e0173871-e0173871.

76. Knoller, S., S. Shpungin, and E. Pick, *The membrane-associated component of the amphiphile-activated, cytosol-dependent superoxide-forming NADPH oxidase of macrophages is identical to cytochrome b559.* Journal of Biological Chemistry, 1991. **266**(5): p. 2795-2804.

77. Branchini, B.R., et al., *Site-Directed Mutagenesis of Histidine 245 in Firefly Luciferase: A Proposed Model of the Active Site.* Biochemistry, 1998. **37**(44): p. 15311-15319.

78. Aillard, B., et al., *Synthesis and evaluation of a (3R,6S,9S)-2-oxo-1-azabicyclo[4.3.0]nonane scaffold as a mimic of Xaa-trans-Pro in poly-l-proline type II helix conformation.* Organic & Biomolecular Chemistry, 2015. **13**(15): p. 4562-4569.

79. Verardi, R., et al., *Isotope labeling for solution and solid-state NMR spectroscopy of membrane proteins.* Advances in experimental medicine and biology, 2012. **992**: p. 35-62.

80. Marley, J., M. Lu, and C. Bracken, *A method for efficient isotopic labeling of recombinant proteins.* Journal of Biomolecular NMR, 2001. **20**(1): p. 71-75.

81. Cavanagh, J., et al., *Protein NMR Spectroscopy: Principles and Practice*. 2010: Elsevier Science.

82. Kleckner, I.R. and M.P. Foster, *An introduction to NMR-based approaches for measuring protein dynamics.* Biochimica et biophysica acta, 2011. **1814**(8): p. 942-968.

83. Kempf, J.G. and J.P. Loria, *Protein dynamics from solution NMR.* Cell Biochemistry and Biophysics, 2002. **37**(3): p. 187-211.

84. Gemmecker, G., *Lecture Script: Advanced NMR Spectroscopy* D.C. Bayrisches NMR-Zentrum, TU München Editor. 2017.

85. Levitt, M.H., *Spin Dynamics: Basics of Nuclear Magnetic Resonance*. Spin Dynamics: Basics of Nuclear Magnetic Resonance. 2001: Wiley.

86. Keeler, J., *Understanding NMR Spectroscopy*. 2011: Wiley.

87. Teng, Q., *Structural Biology: Practical NMR Applications*. SpringerLink : Bücher. 2012: Springer US.

88. Sattler, M., J. Schleucher, and C. Griesinger, *Heteronuclear multidimensional NMR experiments for the structure determination of proteins in solution employing pulsed field gradients.* Progress in nuclear magnetic resonance spectroscopy, 1999. **34**(2): p. 93-158.

89. Higman, V. *Protein NMR* 2019; Available from: https://www.protein-nmr.org.uk/solution-nmr/spectrum-descriptions/.

90. Goricanec, D., et al., *Conformational dynamics of a G-protein α subunit is tightly regulated by nucleotide binding.* Proceedings of the National Academy of Sciences of the United States of America, 2016. **113**(26): p. E3629-E3638.

91. Schrank, E., G.E. Wagner, and K. Zangger, *Solution NMR studies on the orientation of membrane-bound peptides and proteins by paramagnetic probes.* Molecules (Basel, Switzerland), 2013. **18**(7): p. 7407-7435.

92. Clore, G.M. and J. Iwahara, *Theory, Practice, and Applications of Paramagnetic Relaxation Enhancement for the Characterization of Transient Low-Population States of Biological Macromolecules and Their Complexes.* Chemical Reviews, 2009. **109**(9): p. 4108-4139.

93. Keymeulen, F., et al., *Paramagnetic Relaxation Enhancement Experiments: A Valuable Tool for the Characterization of Micellar Nanodevices.* The Journal of Physical Chemistry B, 2013. **117**(39): p. 11654-11659.

94. Lee, W., M. Tonelli, and J.L. Markley, *NMRFAM-SPARKY: enhanced software for biomolecular NMR spectroscopy.* Bioinformatics (Oxford, England), 2015. **31**(8): p. 1325-1327.

95. Häusler, E., et al., *Quantifying the insertion of membrane proteins into lipid bilayer nanodiscs using a fusion protein strategy.* Biochimica et Biophysica Acta (BBA) - Biomembranes, 2020. **1862**(4): p. 183190.

96. Höhner, R., et al., *Proton Gradients and Proton-Dependent Transport Processes in the Chloroplast.* Frontiers in Plant Science, 2016. **7**.

97. Shen, Y., et al., *TALOS+: a hybrid method for predicting protein backbone torsion angles from NMR chemical shifts.* Journal of biomolecular NMR, 2009. **44**(4): p. 213-223.

98. Nasr, M.L., et al., *Covalently circularized nanodiscs for studying membrane proteins and viral entry.* Nature methods, 2017. **14**(1): p. 49-52.

99. Cheng, Y. and D.J. Patel, *An efficient system for small protein expression and refolding.* Biochemical and biophysical research communications, 2004. **317**(2): p. 401-405.

100. Harbron, S., et al., *Molecular Biology and Biotechnology*. 2015: Royal Society of Chemistry.

101. Zhou, P. and G. Wagner, *Overcoming the solubility limit with solubility-enhancement tags: successful applications in biomolecular NMR studies.* Journal of biomolecular NMR, 2010. **46**(1): p. 23-31.

102. Zalk, R., et al., *Oligomeric states of the voltage-dependent anion channel and cytochrome c release from mitochondria.* The Biochemical journal, 2005. **386**(Pt 1): p. 73-83.

103. Shen, Y., et al., *TALOS+: a hybrid method for predicting protein backbone torsion angles from NMR chemical shifts.* Journal of biomolecular NMR, 2009. **44**(4): p. 213-23.

104. Laskowski, R.A., et al., *AQUA and PROCHECK-NMR: programs for checking the quality of protein structures solved by NMR.* J Biomol NMR, 1996. **8**(4): p. 477-86.

Appendix

I. DNA sequence

Following DNA sequences are shown for the main constructs. Primers for single point mutations of OEP21-His_{10} are listed in chapter 3.1.4 and corresponding nucleotide triplets highlighted in bold letters.

i. OEP21-His_{10}

```
ATG GAG ACA TCG CTG CGA TAT GGA GGA GAT TCC AAA GCA CTA AAA ATC CAC GCC     54
AAG GAA AAA CTT CGA ATC GAC ACC AAC ACC TTC TTC CAG GTT CGT GGA GGG CTT    108
GAC ACA AAA ACT GGA CAA CCG AGT TCT GGA AGT GCG CTC ATT AGA CAT TTT TAT    162
CCC AAT TTT TCA GCA ACG CTT GGG GTT GGT GTG CGG TAT GAT AAA CAA GAT TCT    216
GTA GGA GTG AGA TAT GCT AAG AAT GAT AAG TTA CGG TAT ACT GTA CTT GCT AAG    270
AAG ACG TTT CCT GTG ACA AAT GAT GGT CTT GTT AAC TTC AAA ATT AAA GGA GGA    324
TGT GAT GTT GAC CAA GAT TTT AAA GAG TGG AAA TCT AGA GGA GGG GCT GAG TTT    378
TCG TGG AAC GTA TTC AAT TTT CAG AAG GAT CAA GAT GTT AGA CTC AGA ATT GGT    432
TAT GAA GCT TTT GAA CAG GTT CCT TAT CTG CAG ATT AGG GAG AAT AAT TGG ACA    486
TTT AAT GCA GAT TAC AAA GGT AGA TGG AAT GTG AGA TAT GAC TTG CTC GAG CAT    540
CAT CAT CAT CAC CAC CAC CAC CAC CAC                                       567
```

ii. wtOEP21

```
ATG GAG ACA TCG CTG CGA TAT GGA GGA GAT TCC AAA GCA CTA AAA ATC CAC GCC     54
AAG GAA AAA CTT CGA ATC GAC ACC AAC ACC TTC TTC CAG GTT CGT GGA GGG CTT    108
GAC ACA AAA ACT GGA CAA CCG AGT TCT GGA AGT GCG CTC ATT AGA CAT TTT TAT    162
CCC AAT TTT TCA GCA ACG CTT GGG GTT GGT GTG CGG TAT GAT AAA CAA GAT TCT    216
GTA GGA GTG AGA TAT GCT AAG AAT GAT AAG TTA CGG TAT ACT GTA CTT GCT AAG    270
AAG ACG TTT CCT GTG ACA AAT GAT GGT CTT GTT AAC TTC AAA ATT AAA GGA GGA    324
TGT GAT GTT GAC CAA GAT TTT AAA GAG TGG AAA TCT AGA GGA GGG GCT GAG TTT    378
TCG TGG AAC GTA TTC AAT TTT CAG AAG GAT CAA GAT GTT AGA CTC AGA ATT GGT    432
TAT GAA GCT TTT GAA CAG GTT CCT TAT CTG CAG ATT AGG GAG AAT AAT TGG ACA    486
TTT AAT GCA GAT TAC AAA GGT AGA TGG AAT GTG AGA TAT GAC TTG                531
```

iii. hVDAC1-His_6

```
ATG GCT GTG CCA CCC ACG TAT GCC GAT CTT GGC AAA TCT GCC AGG GAT GTC TTC     54
ACC AAG GGC TAT GGA TTT GGC TTA ATA AAG CTT GAT TTG AAA ACA AAA TCT GAG    108
AAT GGA TTG GAA TTT ACA AGC TCA GGC TCA GCC AAC ACT GAG ACC ACC AAA GTG    162
ACG GGC AGT CTG GAA ACC AAG TAC AGA TGG ACT GAG TAC GGC CTG ACG TTT ACA    216
GAG AAA TGG AAT ACC GAC AAT ACA CTA GGC ACC GAG ATT ACT GTG GAA GAT CAG    270
CTT GCA CGT GGA CTG AAG CTG ACC TTC GAT TCA TCC TTC TCA CCT AAC ACT GGG    324
AAA AAA AAT GCT AAA ATC AAG ACA GGG TAC AAG CGG GAG CAC ATT AAC CTG GGC    378
TGC GAC ATG GAT TTC GAC ATT GCT GGG CCT TCC ATC CGG GGT GCT CTG GTG CTA    432
GGT TAC GAG GGC TGG CTG GCC GGC TAC CAG ATG AAT TTT GAG ACT GCA AAA TCC    486
CGA GTG ACC CAG AGC AAC TTT GCA GTT GGC TAC AAG ACT GAT GAA TTC CAG CTT    540
CAC ACT AAT GTG AAT GAC GGG ACA GAG TTT GGC GGC TCC ATT TAC CAG AAA GTG    594
AAC AAG AAG TTG GAG ACC GCT GTC AAT CTT GCC TGG ACA GCA GGA AAC AGT AAC    648
ACG CGC TTC GGA ATA GCA GCC AAG TAT CAG ATT GAC CCT GAC GCC TGC TTC TCG    702
GCT AAA GTG AAC AAC TCC AGC CTG ATA GGT TTA GGA TAC ACT CAG ACT CTA AAG    756
CCA GGT ATT AAA CTG ACA CTG TCA GCT CTT CTG GAT GGC AAG AAC GTC AAT GCT    810
GGT GGC CAC AAG CTT GGT CTA GGA CTG GAA TTT CAA GCA TAA                    852
```

iv. His_6-GB1-Thr-hVDAC1

```
ATG GAG TAC AAG CTT ATC CTG AAC GGT AAA ACC CTG AAA GGT GAA ACC ACC ACC     54
GAA GCT GTT GAC GCT GCT ACC GCG GAA AAA GTT TTC AAA CAG TAC GCT AAC GAC    108
AAC GGT GTT GAC GGT GAA TGG ACC TAC GAC GAC GCT ACC AAA ACC TTC ACG GTA    162
ACC GAA ATC CCA ACG ACC CTG GTT CCG CGT GGT TCT GGT GGT TCT TCT GCT GTG    216
CCA CCC ACG TAT GCC GAT CTT GGC AAA TCT GCC AGG GAT GTC TTC ACC AAG GGC    270
TAT GGA TTT GGC TTA ATA AAG CTT GAT TTG AAA ACA AAA TCT GAG AAT GGA TTG    324
GAA TTT ACA AGC TCA GGC TCA GCC AAC ACT GAG ACC ACC AAA GTG ACG GGC AGT    378
CTG GAA ACC AAG TAC AGA TGG ACT GAG TAC GGC CTG ACG TTT ACA GAG AAA TGG    432
AAT ACC GAC AAT ACA CTA GGC ACC GAG ATT ACT GTG GAA GAT CAG CTT GCA CGT    486
GGA CTG AAG CTG ACC TTC GAT TCA TCC TTC TCA CCT AAC ACT GGG AAA AAA AAT    540
GCT AAA ATC AAG ACA GGG TAC AAG CGG GAG CAC ATT AAC CTG GGC TGC GAC ATG    594
GAT TTC GAC ATT GCT GGG CCT TCC ATC CGG GGT GCT CTG GTG CTA GGT TAC GAG    648
GGC TGG CTG GCC GGC TAC CAG ATG AAT TTT GAG ACT GCA AAA TCC CGA GTG ACC    702
CAG AGC AAC TTT GCA GTT GGC TAC AAG ACT GAT GAA TTC CAG CTT CAC ACT AAT    756
GTG AAT GAC GGG ACA GAG TTT GGC GGC TCC ATT TAC CAG AAA GTG AAC AAG AAG    810
TTG GAG ACC GCT GTC AAT CTT GCC TGG ACA GCA GGA AAC AGT AAC ACG CGC TTC    864
GGA ATA GCA GCC AAG TAT CAG ATT GAC CCT GAC GCC TGC TTC TCG GCT AAA GTG    918
AAC AAC TCC AGC CTG ATA GGT TTA GGA TAC ACT CAG ACT CTA AAG CCA GGT ATT    972
AAA CTG ACA CTG TCA GCT CTT CTG GAT GGC AAG AAC GTC AAT GCT GGT GGC CAC   1026
AAG CTT GGT CTA GGA CTG GAA TTT CAA GCA CTC GAG CAC CAC CAC CAC CAC CAC   1080
```

v. His_6-TEV-MSP1D1

```
CAT CAT CAT CAT CAT CAC GAA AAC CTG TAT TTT CAG GGC AGC ACC TTT AGC AAA    54
CTG CGT GAA CAG CTG GGC CCG GTG ACC CAG GAA TTT TGG GAT AAC CTG GAA AAA   108
GAA ACC GAA GGC CTG CGT CAG GAA ATG AGC AAA GAT CTG GAA GAG GTG AAA GCG   162
AAA GTG CAG CCG TAT CTG GAT GAC TTT CAG AAA AAA TGG CAG GAA GAG ATG GAA   216
CTG TAT CGT CAG AAA GTG GAA CCG CTG CGT GCG GAA CTG CAG GAA GGC GCG CGT   270
CAG AAA CTG CAT GAA CTG CAG GAA AAA CTG AGC CCG CTG GGC GAA GAG ATG CGT   324
GAT CGT GCG CGT GCG CAT GTG GAT GCG CTG CGT ACC CAT CTG GCG CCG TAT AGC   378
GAT GAA CTG CGT CAG CGT CTG GCG GCC CGT CTG GAA GCG CTG AAA GAA AAC GGC   432
GGT GCG CGT CTG GCG GAA TAT CAT GCG AAA GCG ACC GAA CAT CTG AGC ACC CTG   486
AGC GAA AAA GCG AAA CCG GCG CTG GAA GAT CTG CGT CAG GGC CTG CTG CCG GTG   540
CTG GAA AGC TTT AAA GTG AGC TTT CTG AGC GCG CTG GAA GAG TAT ACC AAA AAA   594
CTG AAC ACC CAG TAA                                                     609
```

vi. His_6-TEV-MSP1D1ΔH5

```
CAT CAT CAT CAT CAT CAC GAA AAC CTG TAT TTT CAG GGC AGC ACC TTT AGC AAA    54
CTG CGT GAA CAG CTG GGC CCG GTG ACC CAG GAA TTT TGG GAT AAC CTG GAA AAA   108
GAA ACC GAA GGC CTG CGT CAG GAA ATG AGC AAA GAT CTG GAA GAG GTG AAA GCG   162
AAA GTG CAG CCG TAT CTG GAT GAC TTT CAG AAA AAA TGG CAG GAA GAG ATG GAA   216
CTG TAT CGT CAG AAA GTG GAA CCG CTG GGC GAA GAG ATG CGT GAT CGT GCG CGT   270
GCG CAT GTG GAT GCG CTG CGT ACC CAT CTG GCG CCG TAT AGC GAT GAA CTG CGT   324
CAG CGT CTG GCG GCC CGT CTG GAA GCG CTG AAA GAA AAC GGC GGT GCG CGT CTG   378
GCG GAA TAT CAT GCG AAA GCG ACC GAA CAT CTG AGC ACC CTG AGC GAA AAA GCG   432
AAA CCG GCG CTG GAA GAT CTG CGT CAG GGC CTG CTG CCG GTG CTG GAA AGC TTT   486
AAA GTG AGC TTT CTG AGC GCG CTG GAA GAG TAT ACC AAA AAA CTG AAC ACC CAG   540
TAA                                                                     543
```

vii. His_6-TEV-GB1-Thr-MSP1D1ΔH5

```
CAT CAT CAT CAT CAT CAT GAA AAC CTG TAT TTT CAG GGC TCT GGT ATG GAG TAC     54
AAG CTT ATC CTG AAC GGT AAA ACC CTG AAA GGT GAA ACC ACC ACC GAA GCT GTT    108
GAC GCT GCT ACC GCG GAA AAA GTT TTC AAA CAG TAC GCT AAC GAC AAC GGT GTT    162
GAC GGT GAA TGG ACC TAC GAC GAC GCT ACC AAA ACC TTC ACG GTA ACC GAA ATC    216
CCA ACG ACC CTG GTT CCG CGT GGT TCT GGT GGT AGC ACC TTT AGC AAA CTG CGT    270
GAA CAG CTG GGC CCG GTG ACC CAG GAA TTT TGG GAT AAC CTG GAA AAA GAA ACC    324
GAA GGC CTG CGT CAG GAA ATG AGC AAA GAT CTG GAA GAG GTG AAA GCG AAA GTG    378
CAG CCG TAT CTG GAT GAC TTT CAG AAA AAA TGG CAG GAA GAG ATG GAA CTG TAT    432
CGT CAG AAA GTG GAA CCG CTG GGC GAA GAG ATG CGT GAT CGT GCG CGT GCG CAT    486
GTG GAT GCG CTG CGT ACC CAT CTG GCG CCG TAT AGC GAT GAA CTG CGT CAG CGT    540
CTG GCG GCC CGT CTG GAA GCG CTG AAA GAA AAC GGC GGT GCG CGT CTG GCG GAA    594
TAT CAT GCG AAA GCG ACC GAA CAT CTG AGC ACC CTG AGC GAA AAA GCG AAA CCG    648
GCG CTG GAA GAT CTG CGT CAG GGC CTG CTG CCG GTG CTG GAA AGC TTT AAA GTG    702
AGC TTT CTG AGC GCG CTG GAA GAG TAT ACC AAA AAA CTG AAC ACC CAG TAA        753
```

II. Amino acid sequence

In the following the amino acid sequence of the main constructs are listed. Full sequences of the single point mutations are not shown, but replaced amino acids are highlighted in bold letters.

i. OEP21-His_{10}

```
         10          20          30          40          50          60
METSL RYGGD SKALK IH**A**KE KLRID TNTFF QVRGG LDTKT GQPSS GSALI **R**HFYP NFSAT
         70          80          90         100         110         120
LGVGV **R**YDKQ DSVGV RYAKN DKL**R**Y TVLAK KTFPV TNDGL VNFKI KGGCD VDQDF KEWKS
        130         140         150         160         170         180
RGGAE FSWNV FNFQK DQDVR LRIGY EAFEQ VPYLQ IRENN WTFNA DYKGR WNVRY DLLEH
       189
HHHHH HHHH
```

ii. wtOEP21

```
         10          20          30          40          50          60
METSL RYGGD SKALK IHAKE KLRID TNTFF QVRGG LDTKT GQPSS GSALI RHFYP NFSAT
         70          80          90         100         110         120
LGVGV RYDKQ DSVGV RYAKN DKLRY TVLAK KTFPV TNDGL VNFKI KGGCD VDQDF KEWKS
        130         140         150         160         170      177
RGGAE FSWNV FNFQK DQDVR LRIGY EAFEQ VPYLQ IRENN WTFNA DYKGR WNVRY DL
```

iii. hVDAC1-His_6

```
         10          20          30          40          50          60
MAVPP TYADL GKSAR DVFTK GYGFG LIKLD LKTKS ENGLE FTSSG SANTE TTKVT GSLET
         70          80          90         100         110         120
KYRWT EYGLT FTEKW NTDNT LGTEI TVEDQ LARGL KLTFD SSFSP NTGKK NAKIK TGYKR
        130         140         150         160         170         180
EHINL GCDMD FDIAG PSIRG ALVLG YEGWL AGYQM NFETA KSRVT QSNFA VGYKT DEFQL
        190         200         210         220         230         240
HTNVN DGTEF GGSIY QKVNK KLETA VNLAW TAGNS NTRFG IAAKY QIDPD ACFSA KVNNS
        250         260         270         280 283
SLIGL GYTQT LKPGI KLTLS ALLDG KNVNA GGHKL GLGLE FQA
```

iv. GB1-hVDAC1-His_6

```
         10          20          30          40          50          60
MEYKL ILNGK TLKGE TTTEA VDAAT AEKVF KQYAN DNGVD GEWTY DDATK TFTVT EIPTT
         70          80          90         100         110         120
LVPRG SGGSS AVPPT YADLG KSARD VFTKG YGFGL IKLDL KTKSE NGLEF TSSGS ANTET
        130         140         150         160         170         180
TKVTG SLETK YRWTE YGLTF TEKWN TDNTL GTEIT VEDQL ARGLK LTFDS SFSPN TGKKN
        190         200         210         220         230         240
AKIKT GYKRE HINLG CDMDF DIAGP SIRGA LVLGY EGWLA GYQMN FETAK SRVTQ SNFAV
        250         260         270         280         290         300
GYKTD EFQLH TNVND GTEFG GSIYQ KVNKK LETAV NLAWT AGNSN TRFGI AAKYQ IDPDA
        310         320         330         340         350         360
CFSAK VNNSS LIGLG YTQTL KPGIK LTLSA LLDGK NVNAG GHKLG LGLEF QALEH HHHHH
```

v. His_6-TEV-MSP1D1

```
         10          20          30          40          50          60
HHHHH HENLY FQGST FSKLR EQLGP VTQEF WDNLE KETEG LRQEM SKDLE EVKAK VQPYL
         70          80          90         100         110         120
DDFQK KWQEE MELYR QKVEP LRAEL QEGAR QKLHE LQEKL SPLGE EMRDR ARAHV DALRT
        130         140         150         160         170         180
HLAPY SDELR QRLAA RLEAL KENGG ARLAE YHAKA TEHLS TLSEK AKPAL EDLRQ GLLPV
        190            222
LESFK VSFLS ALEEY TKKLN TQ
```

vi. His_6-TEV-MSP1D1ΔH5

```
         10          20          30          40          50          60
HHHHH HENLY FQGST FSKLR EQLGP VTQEF WDNLE KETEG LRQEM SKDLE EVKAK VQPYL
         70          80          90         100         110         120
DDFQK KWQEE MELYR QKVEP LGEEM RDRAR AHVDA LRTHL APYSD ELRQR LAARL EALKE
        130         140         150         160         170         180
NGGAR LAEYH AKATE HLSTL SEKAK PALED LRQGL LPVLE SFKVS FLSAL EEYTK KLNTQ
```

vii. His_6-TEV-GB1-Thr-MSP1D1ΔH5

```
         10          20          30          40          50          60
HHHHH HENLY FQGSG MEYKL ILNGK TLKGE TTTEA VDAAT AEKVF KQYAN DNGVD GEWTY
         70          80          90         100         110         120
DDATK TFTVT EIPTT LVPRG SGGST FSKLR EQLGP VTQEF WDNLE KETEG LRQEM SKDLE
        130         140         150         160         170         180
EVKAK VQPYL DDFQK KWQEE MELYR QKVEP LGEEM RDRAR AHVDA LRTHL APYSD ELRQR
        190         200         210         220         230         240
LAARL EALKE NGGAR LAEYH AKATE HLSTL SEKAK PALED LRQGL LPVLE SFKVS FLSAL
        250
EEYTK KLNTQ
```

III. Calibration of size exclusion chromatography columns

The following equation were applied to determine the molecular weight of the proteins purified by SEC:

$$K_{av} = \frac{V_e - V_0}{V_c - V_0}$$

Superdex 200 10/300, V_0 = 8.70 mL, V_c = 24 mL

$$\log(MW) = \frac{K_{av} - 2.1348}{-0.355}$$

Superdex 200 pg, V_0 = 46.12 mL, V_c = 120 mL

$$\log(MW) = \frac{K_{av} - 2.081}{-0.336}$$

V_0 = column void volume, V_c = column volume, V_e = elution volume, K_{av} = partition coefficient value

IV. OEP21

i. CD data

Table 14: Melting temperatures including error values of OEP21. *T_m values are listed for OEP21 in the apo state and with additional metabolites using dose-response curve as curve fitting function of OriginPro 9G.*

OEP21	Tm [°C]	Error [°C]
Apo	59.60289	0.05341
+ 0.5 mM ATP	64.15945	0.05701
+ 0.5 mM ADP	60.89700	0.11476
+ 0.5 mM GAP	61.61700	0.07380
+ 0.5 mM PEP	60.12165	0.06745
+ 0.5 mM NADPH	59.70175	0.10956
+ 0.5 mM NADH	58.75904	0.01634

Table 15: Melting temperatures including error values of OEP21 analyzing different pH. *Each buffer condition was analysed with +/- 0.5 mM ATP. Calculations were performed using dose-response curve as curve fitting function of OriginPro 9G.*

OEP21	Tm [°C]	Error [°C]
pH 6.0 / apo	61.51556	0.09825
pH 6.0 / + 0.5 mM ATP	63.20233	0.24044
pH 7.0 / apo	54.58784	0.17906
pH 7.0 / + 0.5 mM ATP	58.38327	0.25966
pH 8.0 / apo	54.10567	0.1327
pH 8.0 / + 0.5 mM ATP	55.98499	0.23444

Table 16: Melting temperatures including error values of OEP21 and mutants. *Each protein measured additionally with 0.5 mM ATP. Calculations were performed, using dose-response curve as curve fitting function of OriginPro 9G.*

OEP21 mutants	Tm [°C]	Error [°C]
OEP21	59.60289	0.05341
OEP21 + 0.5 mM ATP	64.15945	0.05701
OEP21_K19A	55.70524	0.19685
OEP21_K19A + 0.5 mM ATP	66.6744	0.26492
OEP21_R51A	54.31544	0.13347
OEP21_R51A + 0.5 mM ATP	67.43752	0.20673
OEP21_R66A	56.98663	0.16436
OEP21_R66A + 0.5 mM ATP	64.64205	0.27402
OEP21_R84A	52.75752	0.21148
OEP21_R84A + 0.5 mM ATP	64.04441	0.30539

Table 17: Melting temperatures including error values of wtOEP21 +/- 0.5 mM ATP. *Calculations were performed using dose-response curve as curve fitting function of OriginPro 9G.*

OEP21	Tm [°C]	Error [°C]
wtOEP21	62.30006	0.21338
wtOEP21 + 0.5 mM ATP	65.55831	0.27878

ii. GAPDH Assay

Efficiency of GAPDH was analyzed prior to establish the GAPDH-assay using OEP21 in liposomes. Focus on 340 nm, the absorption increases constantly with higher amount of GAP, revealing the reaction of NAD to NADH/H^+ dependent on the GAP concentration.

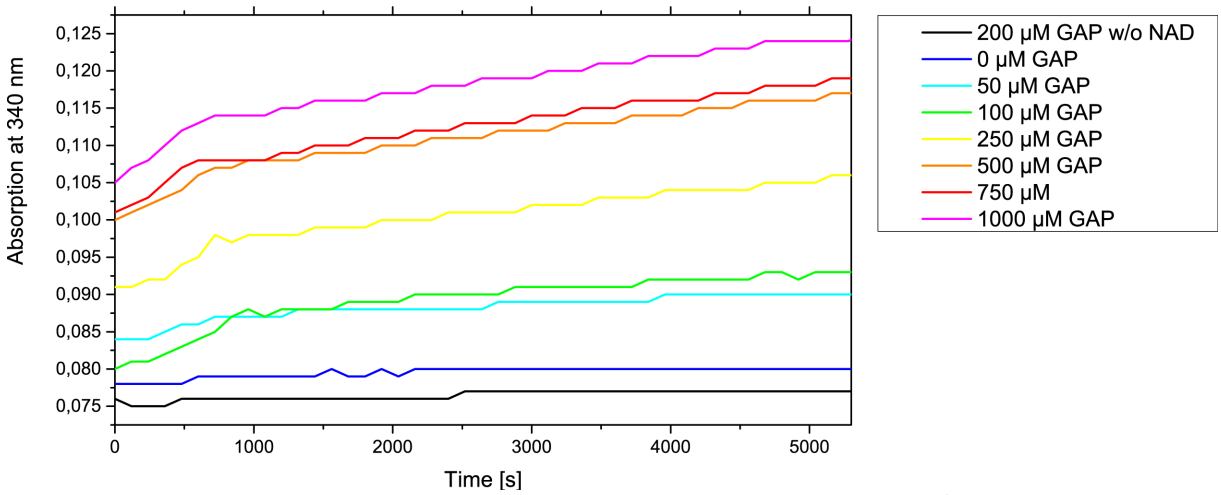

Figure 59: Analysis of GAPDH reaction using GAP and NAD. *Absorption captured at 340 nm for 90 min.*

iii. NMR data of OEP21 structure determination

Table 18: ^{15}N- and ^{1}H-chemical shift list of 2D-[^{1}H,^{15}N]-TROSY of OEP21-His$_{10}$.

Chemical shift assignment	^{15}N-Chemical shift [ppm]	^{1}H-Chemical shift [ppm]	Chemical shift assignment	^{15}N-Chemical shift [ppm]	^{1}H-Chemical shift [ppm]
?-?	122.711	8.326	**L36N-H**	123.512	9.064
?-?	118.302	7.989	**D37N-H**	124.828	8.122
?-?	116.128	7.718	**T38N-H**	116.358	8.030
?-?	120.736	8.304	**T40N-H**	119.322	8.569
?-?	126.487	9.188	**G41N-H**	111.233	8.361
?-?	122.886	8.856	**Q42N-H**	115.310	7.605
?-?	122.083	8.753	**S44N-H**	118.531	9.010
?-?	124.031	8.004	**S45N-H**	113.617	7.698
?-?	121.671	8.102	**G46N-H**	106.680	8.684
?N-H	115.569	7.582	**S47N-H**	114.772	9.201
AN-H	122.078	7.660	**A48N-H**	123.324	8.627
scN-H	116.054	8.132	**L49N-H**	121.542	8.735
scN-H	117.919	8.213	**I50N-H**	122.526	9.164
scN-H	121.075	9.708	**R51N-H**	125.725	9.046
scN-H	118.953	9.471	**H52N-H**	124.520	9.396
E2N-H	125.381	8.794	**F53N-H**	128.650	8.356
T3N-H	105.308	7.703	**Y54N-H**	123.982	8.396
S4N-H	117.839	9.291	**S58N-H**	117.541	7.869
R6N-H	119.963	9.054	**A59N-H**	119.998	7.058
Y7N-H	124.976	9.060	**T60N-H**	116.316	8.953
G8N-H	113.955	7.599	**L61N-H**	126.378	9.013
G9N-H	107.137	6.682	**G62N-H**	111.068	9.224
A13N-H	120.965	8.239	**V63N-H**	118.976	8.651
K15N-H	127.765	9.257	**G64N-H**	111.886	8.904
I16N-H	120.923	8.608	**V65N-H**	116.403	8.838
H17N-H	127.157	9.428	**R66N-H**	121.861	9.225
A18N-H	122.935	8.876	**Y67N-H**	123.199	8.909
K19N-H	119.112	8.399	**D68N-H**	125.810	8.040
E20N-H	123.666	8.910	**K69N-H**	123.123	8.052
K21N-H	125.283	9.511	**Q70N-H**	124.059	8.538
L22N-H	122.870	9.331	**V73N-H**	121.097	7.983
R23N-H	128.351	9.171	**G74N-H**	112.207	8.326
I24N-H	125.000	8.414	**V75N-H**	119.472	7.812
D25N-H	117.154	8.226	**R76N-H**	123.570	8.194
T28N-H	116.613	7.495	**Y77N-H**	120.220	7.902
F29N-H	124.544	9.377	**A78N-H**	125.270	8.099
F30N-H	122.869	9.521	**K79N-H**	119.916	8.095
Q31N-H	127.352	9.242	**D81N-H**	120.957	8.224
V32N-H	122.836	8.649	**K82N-H**	119.645	7.926
R33N-H	123.719	8.700	**L83N-H**	123.252	8.321
G34N-H	106.868	8.482	**R84N-H**	121.527	8.660
G35N-H	107.643	8.241	**Y85N-H**	121.782	8.814

Chemical shift assignment	^{15}N-Chemical shift [ppm]	^{1}H-Chemical shift [ppm]
T86N-H	115.569	8.739
V87N-H	123.093	8.485
L88N-H	125.702	8.972
A89N-H	124.143	9.099
K90N-H	117.626	8.688
K91N-H	122.503	8.752
T92N-H	122.425	8.431
F93N-H	126.118	10.020
V95N-H	121.330	8.644
T96N-H	105.622	7.303
G99N-H	107.903	7.892
L100N-H	119.702	8.231
V101N-H	117.510	7.246
N102N-H	124.624	9.079
F103N-H	121.876	9.182
K104N-H	127.427	8.882
I105N-H	120.202	8.541
K106N-H	122.544	8.542
G107N-H	107.014	8.824
G108N-H	107.880	8.880
C109N-H	116.419	8.720
D110N-H	122.701	8.818
V111N-H	121.073	8.953
D112N-H	123.761	7.779
Q113N-H	114.810	8.017
D114N-H	116.339	7.481
F115N-H	116.819	7.971
K116N-H	119.177	9.000
E117N-H	119.555	7.828
W118N-H	126.339	8.633
W118Ne-He	130.064	10.017
K119N-H	124.980	9.118
S120N-H	120.952	8.169
R121N-H	120.226	8.317
G122N-H	109.590	9.545
G123N-H	107.242	9.095
A124N-H	120.943	8.091
E125N-H	116.074	8.606
F126N-H	122.571	9.395
S127N-H	116.359	8.896
W128N-H	126.357	9.397
W128Ne-He	129.103	10.214

Chemical shift assignment	^{15}N-Chemical shift [ppm]	^{1}H-Chemical shift [ppm]
N129N-H	126.949	8.829
D136N-H	118.771	8.323
Q137N-H	118.739	7.730
D138N-H	124.888	8.493
V139N-H	123.256	8.343
R140N-H	126.658	9.070
L141N-H	127.554	8.908
R142N-H	124.191	9.194
I143N-H	122.016	8.721
G144N-H	112.786	8.346
Y145N-H	118.013	8.668
E146N-H	133.980	8.073
A147N-H	120.290	7.634
F148N-H	123.009	8.847
Y153N-H	118.674	8.659
L154N-H	119.528	9.301
Q155N-H	124.702	9.403
I156N-H	126.426	9.258
R157N-H	128.851	9.091
E158N-H	126.505	9.099
N159N-H	121.084	7.856
W161N-H	123.235	8.795
T162N-H	117.337	9.171
F163N-H	126.494	9.522
N164N-H	124.888	8.707
A165N-H	119.721	8.619
D166N-H	117.670	8.546
Y167N-H	116.703	7.962
K168N-H	115.263	8.211
G169N-H	107.759	8.412
R170N-H	121.958	7.959
W171N-H	119.143	8.067
W171Ne-He	130.893	10.714
N172N-H	114.801	9.080
V173N-H	118.804	9.300
R174N-H	126.059	9.190
Y175N-H	124.807	8.933
D176N-H	128.407	8.130
L177N-H	122.648	8.222
E179N-H	121.887	8.501

Table 19: Structural statistics of OEP21 in LDAO micelles.

Structural information	
Number of NOEs restraints	678 (3.8 / aa)
Number of hydrogen bond restraints	110
Number of dihedral angle restraints (TALOS+ [103])	255
Backbone / heavy atom rmsd for all residues (Å) [b]	1.9 ± 0.3 / 2.4 ± 0.3
Backbone / heavy atom rmsd for ordered secondary structure elements [c] (Å)	0.5 ± 0.1 / 1.1 ± 0.1
Ramachandran Map Analysis [d]	
Most favored regions	81.3 %
Additionally allowed regions	12.9 %
Generously allowed regions	4.5 %
Disallowed regions	1.3 %
Deviation from Restraints and Idealized Geometry	
Distance restraints (Å)	0.035 ± 0.002
Dihedral angle restraints (deg)	0.11 ± 0.04
Bonds (Å)	0.00384 ± 0.00008
Angles (deg)	0.87 ± 0.01
Impropers (deg)	2.4 ± 0.1

[a] Analysis of the 10 lowest-total energy structures

[b] rmsd values are calculated relative to a non-minimized average structure of each ensemble

[c] β-barrel region: residues 1-9, 14-25, 28-36, 44-54, 58-68, 81-94, 102-113, 117-128, 140-146, 151-158, 161-166, 169-176

[d] Ramachandran analysis with PROCHECK-NMR [104] was performed on the lowest-energy structure

V. hVDAC1

Table 20: Determined integrals of hVDAC1 in MSP1D1ΔH5-ND and cleaved GB1. *The integrals of hVDAC1 nanodiscs and GB1($Int_{ND+hVDAC1}$ and Int_{GB1}) are used to calculate the number of GB1 (n_{GB1}), the number of ND (n_{ND}) and finally in the ratio R by using the equations in chapter 4.3.3. GB1-hVDAC1 is the initial GB1-fusion construct for these assemblies.*

Ratio	No	Int $_{ND+hVDAC1}$	Int_{GB1}	n_{GB1}	n_{ND}	R	Mean value	Standard deviation
	#1	149,707	22,801	0,00227873	0,00184923	1,23226283		
1:1	#2	172,616	25,168	0,00251529	0,00224839	**1,1187084**	**1,12518883**	**0,0091647**
	#3	174,743	25,614	0,00255986	0,00226202	**1,13166925**		
	#1	251,717	35,962	0,00359404	0,00335524	**1,07117242**		
1:2	#2	257,236	37,044	0,00370218	0,00339842	**1,08938303**	**1,08247568**	**0,00986913**
	#3	244,766	35,21	0,00351889	0,00323763	**1,0868716**		
1:4	#1	238,602	34,844	0,00348231	0,00310218	**1,12253502**		
	#2	266,419	38,558	0,00385349	0,0034999	**1,10102746**	**1,10519875**	**0,01567262**
	#3	277,002	39,936	0,00399121	0,00365484	**1,09203378**		
	#1	225,034	32,02	0,00320008	0,00301302	**1,06208325**		
1:6	#2	252,017	36,31	0,00362882	0,00332765	**1,0905067**	**1,08215497**	**0,01746402**
	#3	251,916	36,348	0,00363262	0,00332087	**1,09387496**		
	#1	254,226	35,024	0,0035003	0,00352292	**0,99357978**		
1:8	#2	276,611	37,922	0,00378993	0,00385237	**0,98379187**	**0,98073869**	**0,01460895**
	#3	311,59	42,306	0,00422806	0,00438212	**0,96484443**		
						Total MV	**1,07515139**	

Table 21: Determined integrals of hVDAC1 in MSP1D1-ND and cleaved GB1. *The integrals of hVDAC1 nanodiscs and GB1 ($Int_{ND+hVDAC1}$ and Int_{GB1}) are used to calculate the number of GB1 (n_{GB1}), the number of ND (n_{ND}) and finally in the ration R by using the equations in chapter 4.3.3. GB1-hVDAC1 is the initial GB1-fusion construct for these assemblies.*

Ratio	No	Int $_{ND+hVDAC1}$	Int_{GB1}	n_{GB1}	n_{ND}	R	Mean value	Standard deviation
	#1	114,717	23,756	0,00237418	0,00076638	3,09792014		
1:1	#2	99,88	17,033	0,00170228	0,00104522	**1,6286305**	**1,60000387**	**0,04048416**
	#3	102,833	17,302	0,00172916	0,00110041	**1,57137725**		
	#1	152,197	23,3985	0,00233845	0,00185739	**1,25899949**		
1:2	#2	156,417	24,374	0,00243594	0,00187506	**1,29912765**	**1,27832962**	**0,02010431**
	#3	153,177	23,693	0,00236788	0,00185445	**1,27686171**		
	#1	163,999	24,254	0,00242395	0,0021007	**1,15387596**		
1:4	#2	171,777	25,825	0,00258095	0,00215677	**1,19667427**	**1,17600906**	**0,02143688**
	#3	200,551	29,933	0,00299151	0,00254061	**1,17747695**		
	#1	186,929	26,229	0,00262133	0,00254104	**1,03159707**		
1:6	#2	188,212	27,197	0,00271807	0,00247689	**1,09737023**	**1,06974373**	**0,03412524**
	#3	192,737	27,646	0,00276294	0,00255765	**1,08026389**		
	#1	159,441	22,561	0,00225475	0,00214781	**1,04978904**		
1:8	#2	192,188	27,073	0,00270568	0,00260154	**1,04002757**	**1,04458613**	**0,00491253**
	#3	190,842	26,932	0,00269159	0,00257829	**1,04394177**		
						Total MV	**1,23373448**	

Table 22: Determined integrals of hVDAC1 in MSP1D1ΔH5-ND and cleaved GB1. *The integrals of hVDAC1 nanodiscs and GB1 (Int_{ND} and Int_{GB1}) are used to calculate the number of GB1 (n_{GB1}), the number of ND (n_{ND}) and finally in the ratio R by using the equations in chapter 4.3.3. The integrals of empty MSP1D1ΔH5-ND (Int_{ND} and Int_{GB1}) are additionally used to calibrate the extinction coefficient of GB1 by using the equations below. GB1-MSP1D1ΔH5 is the initial GB1-fusion construct for these assemblies.*

Ratio	No	Int_{ND}	Int_{GB1}	n_{GB1}	n_{ND}	R	Mean value	Standard deviation
1:8	#1	186,68295	49,03167	0,00490023	0,00540483	1,10297489	**1,07512725**	**0,03477697**
	#2	199,355208	54,10835	0,00540759	0,00560306	1,03614711		
	#3	227,49015	60,23637	0,00602002	0,00653931	1,08625975		
Empty ND	#1	164,5676	92,60305	0,00925577	0,00925475	0,99988997	**1,00001474**	**0,00700767**
	#2	183,507046	104,00331	0,01032098	0,01039409	1,00708395		
	#3	204,06333	114,04433	0,01147713	0,01139759	0,99307028		

Calculation of ε_{GB1} :

$$\frac{\varepsilon_{MSP}}{Int_{ND}} = \frac{\varepsilon_{GB1}}{Int_{GB1}} \quad \rightarrow \quad \varepsilon_{GB1} = \frac{\varepsilon_{MSP} \cdot Int_{GB1}}{Int_{ND}}$$

By using the three different runs of empty nanodiscs, the extinction coefficient of GB1 can be derived: ε_{GB1} = 10006 $cm^{-1}M^{-1}$.

Acknowledgments

First of all, I want to thank Prof. Dr. Franz Hagn, who gave me the opportunity to be part of his research group and for supporting me at any time. During the last years I was able to educate myself and gain further knowledge in the field of membrane biochemistry. I am very grateful for that.

Further I also want to thank my colleagues for the excellent peer collaboration, support, professional discussions, and not to forget our familiar atmosphere.

Also special thanks to my collaboration partners at Ludwig Maximilian Univerisity , Prof. Dr. Jürgen Soll and Dr. Bettina Bölter, who initiated the OEP21 project and shared their knowledge with me, as well as to Prof. Dr. Martin Zacharias and Dr. Manuel Hitzenberger, both employed at the Technical University Munich, who supported my project by performing MD simulations on OEP21. Again thanks a lot for this great collaboration.

Last, but not least, many thanks to my family and friends, who accompanied me during this period of finishing my doctoral thesis.

THANK YOU!

Anhang I

Eidesstattliche Erklärung

Ich erkläre an Eides statt, dass ich die bei der promotionsführenden Einrichtung
Technische Universität München – Fakultät Chemie

der TUM zur Promotionsprüfung vorgelegte Arbeit mit dem Titel:
NMR structural and biochemical studies on the b-barrel membrane proteins OEP21 and hVDAC1

in Fakultät Chemie – Professur für Strukturelle Membranbiochemie
Fakultät, Institut, Lehrstuhl, Klinik, Krankenhaus, Abteilung

unter der Anleitung und Betreuung durch: Prof. Dr. Franz Hagn ohne sonstige Hilfe erstellt und bei der Abfassung nur die gemäß § 6 Ab. 6 und 7 Satz 2 angebotenen Hilfsmittel benutzt habe.

☒ Ich habe keine Organisation eingeschaltet, die gegen Entgelt Betreuerinnen und Betreuer für die Anfertigung von Dissertationen sucht, oder die mir obliegenden Pflichten hinsichtlich der Prüfungsleistungen für mich ganz oder teilweise erledigt.

☒ Ich habe die Dissertation in dieser oder ähnlicher Form in keinem anderen Prüfungsverfahren als Prüfungsleistung vorgelegt.

☒ Die vollständige Dissertation wurde in englischer Sprache veröffentlicht. Die promotionsführende Einrichtung
Technische Universität München – Fakultät Chemie
hat der Veröffentlichung zugestimmt.

☒ Ich habe den angestrebten Doktorgrad noch nicht erworben und bin nicht in einem früheren Promotionsverfahren für den angestrebten Doktorgrad endgültig gescheitert.

☐ Ich habe bereits am _____ bei der Fakultät für _____
_____
der Hochschule _____
unter Vorlage einer Dissertation mit dem Thema _____
_____
die Zulassung zur Promotion beantragt mit dem Ergebnis: _____
_____

Die öffentlich zugängliche Promotionsordnung der TUM ist mir bekannt, insbesondere habe ich die Bedeutung von § 28 (Nichtigkeit der Promotion) und § 29 (Entzug des Doktorgrades) zur Kenntnis genommen. Ich bin mir der Konsequenzen einer falschen Eidesstattlichen Erklärung bewusst.

Mit der Aufnahme meiner personenbezogenen Daten in die Alumni-Datei bei der TUM bin ich

☒ einverstanden, ☐ nicht einverstanden.

Garching, den 29.06.2020 _____
Ort, Datum, Unterschrift